
Geometry Aware Operator Transformer As An Efficient And Accurate Neural Surrogate For PDEs On Arbitrary Domains

Anonymous Author(s)

Affiliation

Address

email

Abstract

1 The very challenging task of learning solution operators of PDEs on arbitrary do-
2 domains accurately and efficiently is of vital importance to engineering and industrial
3 simulations. Despite the existence of many operator learning algorithms to approx-
4 imate such PDEs, we find that accurate models are not necessarily computationally
5 efficient and vice versa. We address this issue by proposing a geometry aware oper-
6 ator transformer (GAOT) for learning PDEs on arbitrary domains. GAOT combines
7 novel multiscale attentional graph neural operator encoders and decoders, together
8 with geometry embeddings and (vision) transformer processors to accurately map
9 information about the domain and the inputs into a robust approximation of the
10 PDE solution. Multiple innovations in the implementation of GAOT also ensure
11 computational efficiency and scalability. We demonstrate this significant gain in
12 both accuracy and efficiency of GAOT over several baselines on a large number
13 of learning tasks from a diverse set of PDEs, including achieving state of the art
14 performance on a large scale three-dimensional industrial CFD dataset.

15 1 Introduction

16 Partial Differential Equations (PDEs) are widely used to mathematically model very diverse natural
17 and engineering systems [14]. Currently, numerical algorithms, such as the finite element and finite
18 difference methods, are the preferred framework for *simulating* PDEs [44]. However, these methods
19 can be computationally very expensive, particularly for the so-called *many-query* problems such
20 as uncertainty quantification (UQ), control, and inverse problems. Here, the solver must be called
21 repeatedly, leading to prohibitive costs and providing the impetus for the design of fast and efficient
22 surrogates for PDE solvers [36].

23 To this end, ML/AI based algorithms are increasingly being explored as *neural PDE surrogates*. In
24 particular, *neural operators* [22, 5], including those proposed in [27, 28, 33, 45, 20], which learn
25 the *PDE solution operator* from data, are widely used [2]. As many of these neural operators are
26 restricted to PDEs on Cartesian (regular) grids, they cannot be directly applied to most engineering
27 and industrial systems, which are set on domains with complex geometries, imposing a pressing need
28 for neural operators for learning PDEs on arbitrary domains (point clouds).

29 In this context, a variety of options have recently been proposed, including domain masking for FNO
30 and CNO [45], replacing FFT in FNO with direct spectral evaluations [31], augmenting FNO with
31 learned diffeomorphisms [26] and mapping arbitrary point cloud data between the input domain and
32 latent regular grids with learned encoders/decoders, while processing on the latent grid with FNO [29]
33 or transformers [1]. Alternatives such as end-to-end message-passing based graph neural networks
34 [41, 15, 47, 46, 6, 13, 39] or end-to-end transformer based models [50, 18] have also been proposed.

35 A thorough comparison of the existing models, not
 36 just in terms of accuracy but also computational
 37 efficiency and scalability, is necessary to evaluate
 38 whether these models are yet capable enough to
 39 act as surrogates for highly successful finite ele-
 40 ment methods for engineering simulations [44].
 41 As one of the contributions in this paper, we per-
 42 formed such a comparison (see Sec.3 for details)
 43 to find evidence for an *accuracy-efficiency trade-*
 44 *off*, i.e., accurate and robust models, such as the
 45 message passing based RIGNO of [39] are not
 46 necessarily computationally efficient nor scalable
 47 in terms of training throughput and inference la-
 48 tency. On the other hand, more efficient models
 49 such as GINO [29] are not accurate enough (see
 50 the accompanying Radar Chart in Fig. 1). Given
 51 this observation, our main goal in this paper is
 52 to propose an algorithm to learn PDE solution
 53 operators on arbitrary domains that is accurate,
 54 computationally efficient, and can be seamlessly
 55 scaled to real-world industrial problems.

56 To this end, we propose *Geometry Aware Operator*
 57 *Transformer* (GAOT, pronounced goat) as a neural surrogate for PDEs on arbitrary domains. While
 58 being based on the well-established *encode-process-decode* paradigm [41], GAOT includes several
 59 novel features that are designed to ensure both computational efficiency and accuracy, such as

- 60 • Our proposed *multiscale attentional graph neural operator* (MAGNO) as the encoder
 61 between inputs on an arbitrary point cloud and a *coarser* latent grid, designed to enhance
 62 accuracy through its multiscale information processing and attention modules.
- 63 • Novel *Geometry embeddings* in the encoder (and decoder) that provide the model with
 64 access to information about the (local) domain geometry, greatly increasing accuracy.
- 65 • A *transformer processor* that utilizes patching (as in ViTs [10]) for computational efficiency.
- 66 • A MAGNO decoder, able to generate *neural fields*, with the ability to approximate the
 67 underlying solution at *any query point* in the domain.
- 68 • A set of implementation strategies to ensure that the computational realization of GAOT is
 69 efficient and highly scalable.

70 Combining these elements allows GAOT to treat PDEs on arbitrary domains in a robust, accurate
 71 and computationally efficient manner. We demonstrate these capabilities by,

- 72 • Extensively testing GAOT on 24 challenging benchmarks for both time-independent and
 73 time-dependent PDEs of various types, ranging from regular grids to random point clouds to
 74 highly unstructured adapted grids, and comparing it with widely-used baselines to show that
 75 GAOT is both highly accurate as well as computationally efficient and scalable, see Fig. 1.
- 76 • The efficiency and scalability of GAOT is further showcased by it achieving state of the
 77 art (SOTA) performance on the large scale three-dimensional industrial benchmark of
 78 *DrivAerNet++* dataset for automobile aerodynamics [12].
- 79 • Through extensive ablations, we also highlight how the novel elements in the design of
 80 GAOT such as multiscale attentional encoders and geometry embeddings crucially contribute
 81 to the overall performance of our model.

82 2 Methods.

83 **Problem Formulation.** We start with a generic *time-independent PDE*,

$$\mathcal{D}(c, u) = f, \quad \forall x \in D \subset \mathbb{R}^d, \quad \mathcal{B}(u) = u_b, \quad x \in \partial D, \quad (1)$$

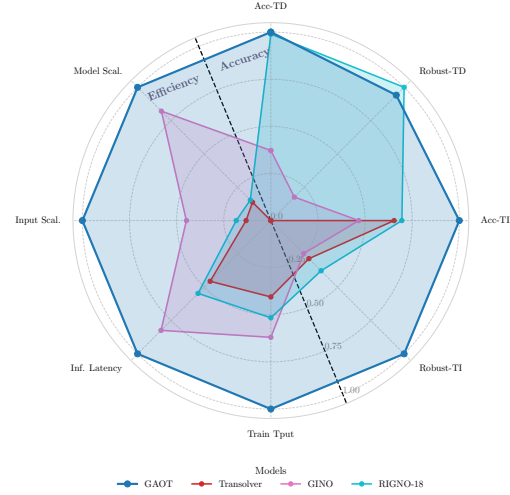


Figure 1: Normalized performance of GAOT and baselines across eight axes, covering accuracy (Acc.), robustness (Robust), throughput (Tput), scalability (Scal.) on time-dependent (TD) and time-independent (TI) tasks.

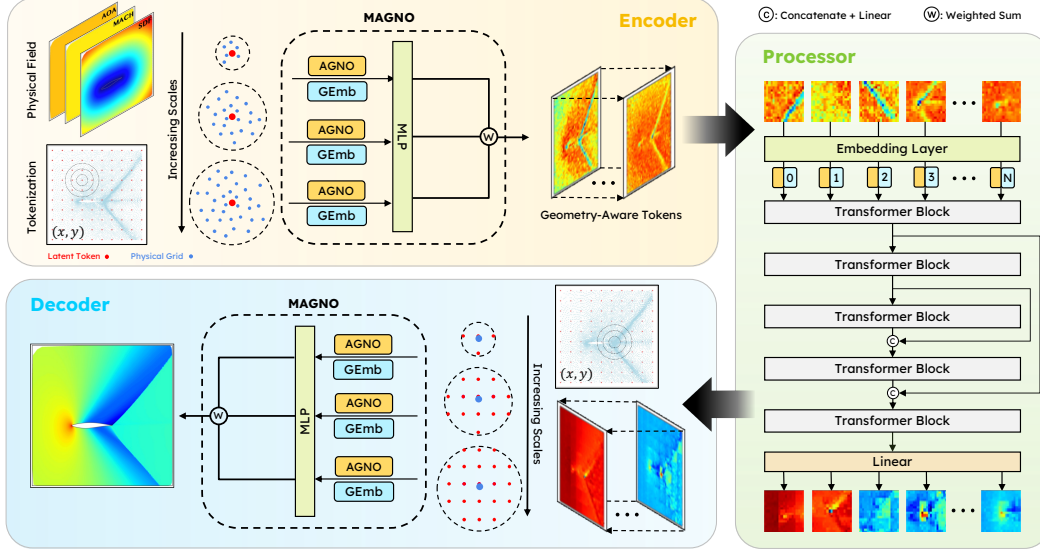


Figure 2: Schematic of the GAOT with an equispaced latent token grid. The encoder uses a multiscale attentional graph neural operator (MAGNO) to aggregate the input data into geometry-aware tokens. A vision transformer (ViT) block with residual connections processes tokens, enabling global exchange of information. A MAGNO decoder identifies the nearest tokens around a given query point to decode the final field.

84 with $u : D \mapsto \mathbb{R}^m$, the PDE solution, c is the coefficient (PDE parameters), f is the forcing term, u_b
85 are boundary values and \mathcal{D} and \mathcal{B} are the underlying differential and boundary operators, respectively.
86 Denoting as χ_D , a function (e.g. indicator or signed distance) parameterizing the domain D , we
87 combine all the *inputs* to the PDE (1) together into $a = (c, f, u_b, \chi_D)$, then the *solution operator* \mathcal{S}
88 maps inputs into PDE solution with $u = \mathcal{S}a$. The corresponding *operator learning* task is to learn
89 the solution operator \mathcal{S} from data. To this end, let μ be an underlying *data distribution*. We sample
90 i.i.d. inputs $a^{(i)} \sim \mu$, for $1 \leq i \leq M$ and assume that we have access to *data pairs* $(a^{(i)}, u^{(i)})$ with
91 $u^{(i)} = \mathcal{S}a^{(i)}$. Thus, the operator learning task is to approximate the distribution $\mathcal{S}_{\# \mu}$ from these data
92 pairs. In practice, we can only access *discretized* versions of the data pairs, sampled on collocation
93 points (which can vary over samples).

94 Similarly denoting a generic *time-dependent PDE* as,

$$u_t + \mathcal{D}(c, u) = 0, \quad \forall x \in D \subset \mathbb{R}^d, t \in [0, T] \quad u(0) = u_0, \quad x \in D, \quad (2)$$

95 with $u : D \times [0, T] \mapsto \mathbb{R}^m$, c the PDE coefficient and u_0 the initial datum and the underlying (spatial)
96 differential operator \mathcal{D} . Clubbing the *inputs* to the PDE (2) into $a = (c, u_0, \chi_D)$, the corresponding
97 *solution operator* \mathcal{S}_t , with $u(t) = \mathcal{S}_t(a)$ for all $t \in [0, T]$, maps the input into trajectory of the
98 solution. The *operator learning* task consists of approximating $(\mathcal{S}_t)_{\# \mu}$ from data pairs $(a^{(i)}, u^{(i)}(t))$
99 for all $t \in [0, T^{(i)}]$ and $1 \leq i \leq M$ with samples a_i drawn from the data distribution μ . However in
100 practice, we only have access to data, sampled on a discrete set of spatial points per sample as well as
101 only on discrete time snapshots $t_n^{(i)} \in [0, T^{(i)}]$ and have to learn the solution operator from them.

102 **GAOT Model Architecture.** The overall architecture of GAOT is depicted in Fig. 2. For simplicity
103 of exposition, we start with the time-independent case, where given inputs $a(x_j)$ on the point cloud
104 $D_\Delta = \{x_j\} \subset D$, for $1 \leq j \leq J$, GAOT provides an approximation to solution u of the PDE (1) at
105 any query point $x \in D$. At a high level, GAOT follows the *encode-process-decode* paradigm of [41].
106 In the first step, an *encoder* transforms the input on the underlying point cloud D_Δ to a *latent point*
107 *cloud* $\mathcal{D} \subset \mathbb{R}^d$. The resulting *spatial tokens* are then processed by a processor module to learn useful
108 representations and its output is remapped to the original domain D via the *decoder*, which allows
109 evaluation at any query point $x \in D$.

110 **Choice of Latent Domain.** As depicted in SM Fig. B.1, the latent domain \mathcal{D} (to which the encoder
111 maps) can be chosen in three different ways, namely i) a regular (structured) grid stencil, consisting of

112 equispaced points on a Cartesian domain (see also Fig. 2) ii) randomly downsampling the underlying
 113 point cloud D_Δ or iii) a projected low-dimensional representation, where a high-dimensional domain
 114 is projected to a lower dimension (for instance using tri-plane embeddings in 3-D [8]) and a regular
 115 grid is used in the lower-dimensional domain. GAOT is a general framework where any of these
 116 latent point cloud choices can be employed for \mathcal{D} .

117 **Encoder.** Given input values $a(x_j)$ on the underlying point cloud D_Δ , the encoder aims to transform
 118 it into latent features $w_e(y)$ at any point $y \in \mathcal{D}$ on the latent point cloud. Using a graph-neural
 119 operator (GNO) encoder as in GINO [29] would lead to,

$$\tilde{w}_e(y) = \sum_{k=1}^{n_y} \alpha_k K(y, x_k, a(x_k)) \varphi(a(x_k)), \quad (3)$$

120 with MLPs K and φ and the sum above taken over all the n_y points $x_k \in D_\Delta$ such that $|y - x_k| \leq r$
 121 for some hyperparameter $r > 0$, where α_k are some given quadrature weights. In other words, a
 122 GNO accumulates information from all the points in the original point cloud that lie inside a ball of
 123 radius r , centered at the given point y in the latent point cloud, and processes them through a kernel
 124 integral.

125 Our first innovation is based on the realization that this *single-scale* approach might be limiting the
 126 overall accuracy. Instead, we would like to introduce a mechanism to integrate *multiscale* information
 127 into the encoder. To this end and as shown in Fig. 2, we choose $r_m = s_m r_0$, for some base radius r_0
 128 and scale factors s_m , for $m = 1, \dots, \bar{m}$ to modify GNO (3) by,

$$\tilde{w}_e^m(y) = \sum_{k=1}^{n_y^m} \alpha_k^m K^m(y, x_k, a(x_k)) \varphi(a(x_k)), \quad (4)$$

129 for any fixed scale m and with MLPs K^m, φ . The above sum is taken over all the n_y^m points $x_k \in D_\Delta$
 130 such that $|y - x_k| \leq r_m$. To choose the quadrature weights α_k^m , we propose an *attention based*
 131 choice,

$$\alpha_k^m = \frac{\exp(e_k^m)}{\sum_{k'=1}^{n_y^m} \exp(e_{k'}^m)}, \quad e_k^m = \frac{\langle \mathbf{W}_q^m y, \mathbf{W}_\kappa^m x_k \rangle}{\sqrt{d}}, \quad (5)$$

132 with $\mathbf{W}_q^m, \mathbf{W}_\kappa^m \in \mathbb{R}^{\bar{d} \times m}$ are query and key matrices respectively, completing the description of the
 133 *attentional graph neural operator* (AGNO) (4) at each scale m .

134 **Geometry Embeddings.** The only geometric information in the afore-described encoder is provided
 135 by the coordinates of the underlying points. This alone does not convey the rich geometric information
 136 about the domain that can affect the solution of the underlying PDE (2). Hence, we need to
 137 embed further geometric information into the model. Deviating from the literature where geometric
 138 information is provided either by appending them as node and edge features on the underlying graphs
 139 [15] or by encoding a signed distance function [29], we propose to use novel *geometry embeddings* to
 140 encode this information. To this end and as described in SM Sec. B.3, we can rely on *local statistical*
 141 *embeddings* for each point $y \in \mathcal{D}$ as all the neighboring points x_k in D_Δ with $|y - x_k| \leq r_m$ have
 142 already been computed in the AGNO encoder. From these points, we can readily compute statistical
 143 descriptors such as i) number of neighbors $x_k \in D_\Delta$, in the ball $B_{r_m}(y)$, ii) the *average distance*
 144 $D_{\text{avg}} = \frac{1}{n_y^m} \sum_{k=1}^{n_y^m} |y - x_k|$, iii) the variance of this distance D_{var} , with respect to the average D_{avg} ,
 145 iv) the *centroid offset vector* $\Delta_y = \frac{1}{n_y^m} \sum_{k=1}^{n_y^m} (x_k - y)$ and v) a few principal component (PCA)
 146 features of the covariance matrix of $y - x_k$ to calculate the *local shape anisotropy*. These statistical
 147 descriptors, for each scale m and each point $y \in \mathcal{D}$ are then concatenated into a single vector z_y ,
 148 normalized across components to yield zero mean and unit variance and fed into an MLP to provide
 149 the embedding $g^m(y)$. Alternatively, geometry embedding using emphPointNet models [42] can also
 150 be considered.

151 **MAGNO.** As shown in Fig. 2, the scale-dependent AGNO \tilde{w}_e^m (4) and the geometry embedding
 152 g^m , at each scale m , can be concatenated together and passed through another MLP to yield a

scale-specific latent features function $\hat{w}^m(y)$. Next, we need to integrate these features across all m scales. Instead of naively summing these scale contributions, we observe that different scales might contribute differently for every latent token to the encoding. To ascertain this relative contribution, we introduce a (small) MLP ψ_m and weigh the relative contributions with a *softmax* and combine them into the *multiscale attentional graph neural operator* or MAGNO encoder by setting,

$$w_e(y) = \sum_{m=1}^{\bar{m}} \beta_m(y) \hat{w}^m(y), \quad \forall y \in \mathcal{D}, \quad \beta_m(y) = \frac{\exp(\psi_m(y))}{\sum_{m'=1}^M \exp(\psi_{m'}(y))} \quad (6)$$

Transformer Processor. The encoder provides a set of *geometry aware tokens* $w_e(y_\ell)$, for all points $y_\ell \in \mathcal{D}$, with $1 \leq \ell \leq L$, in the latent point cloud. These tokens are further transformed by a processor. As shown in Fig. 2, we choose a suitable transformer based processor. While postponing details on the processor architecture to SM Sec. B.4, we summarize our choices here. If the latent points $\{y_\ell\}$ lie on a regular grid (either through a structured stencil or a projected low-dimensional one), we use a patch-based *vision transformer* or ViT ([10] and [20, 38] for PDE operator learning) for computational efficiency. The equispaced latent points are combined into patches and the tokens in each patch are flattened into a single token embedding which serves as the input for a multi-head attention block, followed by a feed forward block. RMS normalization is applied to the tokens before processing. Either sinusoidal absolute position embeddings or rotary relative position embeddings are used to encode token positions. If the latent points y_ℓ are randomly downsampled from the original point cloud, there is no obvious way to patch them together. Hence, a standard transformer [49], but with RMS normalization, can be used. Additionally, we employ multiple skip connections across transformer blocks (see Fig. 2). The transformer processor transforms the tokens $w_e(y_\ell)$ into processed tokens, that we denote by $w_p(y_\ell)$, for all $1 \leq \ell \leq L$.

Decoder. Given any query point $x \in D$ in the original domain, the task of the decoder in GAOT is to provide $w(x)$, which approximates the solution u of the PDE (1) at that point. To this end, we simply employ the MAGNO architecture in reverse. By choosing a base radius \hat{r}_0 and scale factors \hat{s}_m , a set of increasing radii $\hat{r}_m = \hat{s}_m \hat{r}_0$ are selected to define a set of increasing balls $B_{\hat{r}_m}(x)$ around the query point x (Fig. 2). A corresponding AGNO model is defined by replacing $y \rightarrow x$, $x_k \rightarrow y_\ell$ and $a \rightarrow w_p$ in (4), with corresponding attentional weights computed via (5). In parallel, *geometry embeddings* over each ball $B_{\hat{r}_m}(x)$ are computed to provide statistical information about how the latent points y_ℓ are distributed in the neighborhood of the query point x . These AGNO features and geometry embeddings are concatenated and passed through a MLP to provide $w(x)$ which has the desired dimensions of the solution u of the PDE (1). We denote the GAOT model as S_θ with the output $w = S_\theta(a)$, for the inputs a to the PDE (1). It is trained to minimize the mismatch the underlying operator \mathcal{S} , i.e, the parameters θ are determined to minimize a loss $\mathcal{L}(\mathcal{S}(a), S_\theta(a))$, over all input samples a^i , with \mathcal{L} being either the absolute or mean-square errors.

Extension to time-dependent problems. To learn the solution operator S_t of the time-dependent PDE, we observe that the S_t can be used to update the solution forward in time, given the solution at any time point $u(t)$ by applying $u(t + \tau) = S_\tau(u(t))$. Thus, for any time t , given the augmented input $a(t) = (c, u(t))$, with c being the coefficient in the PDE (2), we need GAOT to output $u(t + \tau)$, for any $\tau \geq 0$. To this end, we retain the architecture of GAOT, as described for the time-independent case above, and simply add the current time t and the *lead-time* τ as further inputs to the model. More precisely, the time-dependent version of GAOT is of the form $\hat{S}_\theta(x, t, \tau, a(t))$, where $a(t)$ takes values at points sampled in D . Following [39], the map \hat{S}_θ can be used to update an approximate solution of PDE (2) in time by following a very general time-stepping strategy:

$$S_\theta(t, \tau, a(t)) = \gamma u(t) + \delta \hat{S}_\theta(x, t, \tau, a(t)). \quad (7)$$

Here, choosing the parameters (γ, δ) appropriately leads to different strategies for time stepping: $\gamma = 0, \delta = 1$ directly approximates the *output* of the solution operator at time $t + \tau$; $\gamma = 1, \delta = 1$ yields the *residual* of the solution at the later time, with respect to the solution at current time; $\gamma = 1, \delta = \tau$ is equivalent to approximating the *time-derivative* of the solution. GAOT provides the flexibility to use any of these time-stepping strategies. We also use the *all2all* training strategy [20] to leverage trajectory data for time-dependent PDEs.

Table 1: Benchmark results on time-dependent and time-independent datasets. Best and 2nd best models are shown in blue and orange fonts for each dataset.

Dataset	Median relative L^1 error [%]					
Time-Independent	GAOT	RIGNO-18	Transolver	GNOT	UPT	GINO
Poisson-C-Sines	3.10	6.83	77.3	100	100	20.0
Poisson-Gauss	0.83	2.26	2.02	88.9	48.4	7.57
Elasticity	1.34	4.31	4.92	10.4	12.6	4.38
NACA0012	6.81	5.30	8.69	6.89	16.1	9.01
NACA2412	6.66	6.72	8.51	8.82	17.9	9.39
RAE2822	6.61	5.06	4.82	7.15	16.1	8.61
Bluff-Body	2.25	5.76	1.78	44.2	5.81	3.49
Time-Dependent	GAOT	RIGNO-18	RIGNO-12	GeoFNO	FNO DSE	GINO
NS-Gauss	2.91	2.29	3.80	41.1	38.4	13.1
NS-PwC	1.50	1.58	2.03	26.0	56.7	5.85
NS-SL	1.21	1.28	1.91	13.7	22.6	4.48
NS-SVS	0.46	0.56	0.73	9.75	26.0	1.19
CE-Gauss	6.40	6.90	7.44	42.1	30.8	25.1
CE-RP	5.97	3.98	4.92	18.4	27.7	12.3
Wave-Layer	5.78	6.77	9.01	11.1	28.3	19.2
Wave-C-Sines	4.65	5.35	6.25	13.1	5.52	5.82

Efficient implementation. As our goal is to ensure accuracy and computational efficiency, we have designed GAOT with ability for large-scale computations in mind. We started with the realization that the heaviest burden of the computation should fall on the processor. The encoder and decoder are often responsible for memory overheads as these modules entail sparse computations on graphs with far more edges than nodes, making the computations largely edge-based and leading to high (and inefficient) memory usage. Moreover, in many PDE learning tasks on arbitrary geometries, the underlying domain (and the resulting graph) varies significantly between data samples, making load balancing very difficult.

To address these computational challenges, we resorted to i) moving the graph construction outside the model evaluation by either storing the graph, representing the input point cloud, in memory for small graphs or on disk for large graphs and loading them during training with efficient data loaders ii) sequentially processing each input in a given batch for the encoder and decoder, while still batch processing in the transformer processor, allowing us to reduce memory usage while retaining efficiency and iii) if needed for very large-scale datasets, we use an edge-dropping strategy to further increase the memory usage of the encoder and decoder. These innovations are essential to ensure batch training and underpin the efficiency of GAOT, even when input geometries vary significantly.

3 Results.

Datasets and Baselines. We start by testing GAOT of a challenging suite of 15 datasets for PDEs with input/output data on arbitrary point clouds in two space dimensions, see SM Secs D and G. for a detailed description of the datasets and for visualizations, respectively. For time-independent PDEs, in addition to the elasticity benchmark of [26], we consider two Poisson equation datasets: Poisson-Gauss, defined on random points in a square domain, and Poisson-C-Sines, a new dataset we propose, containing rich multiscale solutions on a circular domain. In addition, we propose 4 new datasets comprising compressible flows past objects, both airfoils as well as bluff bodies. These datasets have significant variation in domain geometry and flow conditions (Mach numbers ranging from subsonic to supersonic, varying angles of attack etc.) and are tailor-made for testing neural PDE surrogates on arbitrary domains. For time-dependent PDEs, we test on the challenging datasets considered recently in [39], composed of 8 operators corresponding to the compressible Euler (2), incompressible Navier-Stokes (4), and acoustic wave equations (2). These time-dependent operators include complex multiscale solutions with shocks and other sharp traveling waves which can interact, reflect and diffract making them hard to learn. We test GAOT on these datasets and compare them

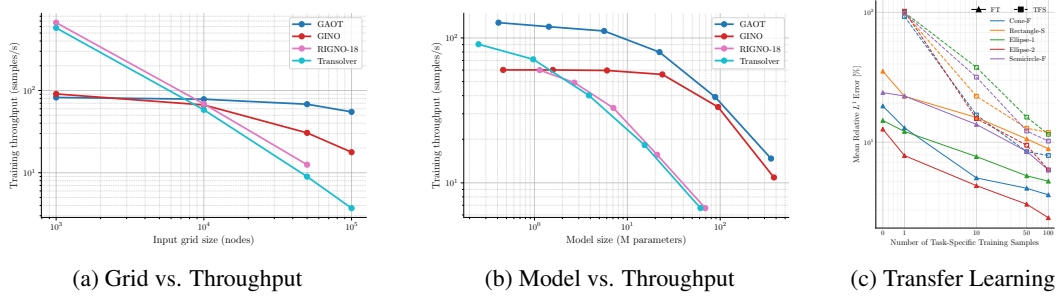


Figure 3: Training throughput (samples/s) with increasing input grid size (a) and model size (b) for proposed GAOT, GINO, RIGNO and Transolver. (c) Transfer learning performance of GAOT on unseen bluff body shapes (See SM Sec. E.6 for dataset details). FT (fine-tuning) adapts a pretrained GAOT model from Table 1, while TFS denotes training from scratch. FT consistently outperforms TFS across varying numbers of task-specific training samples.

with several widely used neural operators for PDEs on arbitrary domains including those based on message passing (RIGNO [39]), Fourier Layers (GINO [29], GeoFNO [26], FNO DSE[31]) and Transformers (Transolver [50], UPT [1] and GNOT [18]).

Accuracy and Robustness. In Table 1, we present the relative test errors for the above datasets to observe that GAOT is very accurate on all of them, being either the best (10) or second-best (4) model on 14 of them. On average, over the time-independent datasets, GAOT is almost 50% more accurate than the second-best performing model (RIGNO-18) while on time-dependent datasets, it is slightly more accurate than the second-best performing model (RIGNO-18). What is even more noteworthy is the *robustness* of the performance of GAOT over all the datasets. As seen from Table 1, the accuracy of GAOT is uniformly good over all the datasets and does not deteriorate on any of them. On the other hand, all the baselines show significantly poor performance on outlier datasets. This robustness can be quantified in terms of a *robustness score* (see SM Sec. E.1) to find that GAOT is almost three times more robust on the time-independent datasets as the second-best model (RIGNO-18), while GAOT and RIGNO-18 are as robust as each other on the time-dependent datasets.

Computational Efficiency and Scalability. It is worth reiterating that the computational efficiency of an ML model is a significant marker of overall performance. We test efficiency in terms of two critical quantities, the *training throughput* and the *inference latency*. For a given input and model size, training throughput measures the number of samples that a model can process during training (forward pass, backward pass and gradient update) per unit time (second) on a given compute system (GPU or CPU). The higher the training throughput, the faster the model can be trained. On the other hand, the inference latency is the amount of time it takes for a model to infer a single input. We present the throughput and latency for GAOT and three selected baselines (RIGNO-18 for Graph-based, GINO for FNO-based and Transolver for Transformer-based models) in Table 2 for learning tasks (such as the bluff-body dataset for compressible flow) where the domain geometry varies throughout the dataset. These experiments are conducted on one NVIDIA-4090 GPU with float32 precision. We see from this table that GAOT has the highest training throughput and the fastest inference latency, being almost 50% and 15%, respectively better than the second-most efficient model (GINO).

How the training throughput of a model scales with increasing input and model size, is absolutely crucial for evaluating whether it can be used to process large-scale datasets (input scalability) or whether it can serve as a backbone of foundation models (model scalability) which require large model sizes [20]. To evaluate the scalability of different models, we plot how the training throughput changes as input size and model size (Fig. 3 (a, b)) are increased to find that GAOT scales much more favorably than the baselines with respect to both input and model size. In fact, models like Transolver and GNOT scale very poorly, making it impossible for us to train them for the large-scale

Table 2: Comparison of model size (Params.), throughput (samples/s), and latency (ms) across GAOT and representative baselines.

Model	Params. (M)	Tput.	Latency
GAOT	5.62	97.5	6.966
GINO	6.04	60.4	8.455
RIGNO-18	2.69	50.3	12.74
Transolver	3.86	39.5	15.29

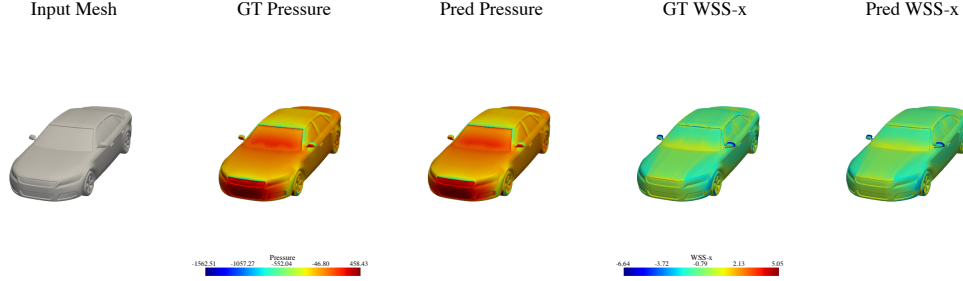


Figure 4: Comparison of predicted and ground-truth (GT) results for the pressure and wall shear stress in the x-direction (WSS-x) on the DrivAerNet++ test sample N_S_WWS_WM_172.

time-dependent datasets with all2all training, which requires handling large volumes of data for large input sizes. Hence, we omit them in the accuracy results for time-dependent datasets in Tab. 1. The results for both accuracy and efficiency across a range of metrics for GAOT, RIGNO, GINO and Transolver are summarized in SM Tab. E.1 and visualized in the Radar chart Fig. 1 demonstrating that GAOT ensures both accuracy (robustness) and computational efficiency (scalability) at the same time, while being the best model performing model on both sets of metrics.

The DrivAerNet++ Dataset. Given the high accuracy and excellent computational efficiency and scalability of GAOT, we showcase its abilities further on a challenging three-dimensional large-scale benchmark for industrial simulations, the DrivAerNet++ dataset of [12]. In this benchmark, the data consists of high-fidelity CFD simulations across 8K different car shapes which span the entire range of conventional car design. The underlying task is to learn steady-state surface fields (See Fig. 4) such as the pressure and wall shear stress, given the input car shape and flow conditions. The underlying data has approximately 500K points per shape, making the overall training extremely compute intensive. Thus, only scalable models can currently process this learning task. We test GAOT on this challenging 3D benchmark and report the RMSE and MAE test errors for the pressure and wall shear stress in Tab. 3. Compared to baselines results taken from the leaderboard of the DrivAerNet++ challenge [8], we see that GAOT significantly improves on the state-of-the-art (see also Fig. 4). This improvement is most visible in the MAE for wall shear stress where GAOT is ca. 30% more accurate than the second-best model (TripNet), which currently sits atop the leaderboard. We recall that GAOT’s decoder endows it with *neural field* properties. We showcase it for the DrivAerNet++ dataset by training GAOT on a randomly selected set of less than 10% of the total input points (per batch) and then testing on the original car surface point cloud by querying the desired points through GAOT’s decoder. Although not as accurate as training GAOT with full input, we observe from Tab. 3 that this neural field version of GAOT has comparable accuracy to some of the baselines which have been trained with 10x more input points, further demonstrating the flexibility and accuracy of GAOT.

Table 3: Error Metrics of MSE ($\times 10^{-2}$) and Mean AE ($\times 10^{-1}$) for Pressure and Wall Shear Stress on the DrivAerNet++ Dataset.

Model	Pressure		Wall Shear Stress	
	MSE	Mean AE	MSE	Mean AE
GAOT	4.9409	1.1017	8.7370	1.5674
FIGConvNet	4.9900	1.2200	9.8600	2.2200
TripNet	5.1400	1.2500	9.5200	2.1500
RegDGCNN	8.2900	1.6100	13.8200	3.6400
GAOT (NeurField)	12.0786	1.7826	22.9160	2.5099

Generality, Generalization and Scaling. We highlight GAOT’s flexibility with respect to the point distributions that it can handle by testing it on PDEs with regular grid inputs, as suggested in [39]. To this end, we considered 7 additional datasets and present the test errors in SM Sec. E.3. to find that GAOT is highly accurate even on regular grids and is either more accurate or comparable to the highly expressive GNN-based RIGNO, while being more accurate than widely used neural operators such as FNO and CNO. A key requirement in operator learning [22, 4] is the ability of the model to generalize (at test time) to input and output resolutions that are different from the training resolution. As GAOT can be readily evaluated at any query point, we showcase this aspect of GAOT in SM Sec. E.5. by plotting the test errors for a sequence of resolutions, different from the training resolution, for the Poisson-Gauss benchmark, to find that GAOT generalizes very well in both the sub- and super-resolution settings, even to grids with 10x more input points than the training resolution.

Another test of the generalizability of a model is its ability to perform well *out-of-distribution*, either zero-shot or when it is fine-tuned with a few in-distribution samples for the new learning task. To test this aspect, we consider the datasets for compressible flow past bluff bodies and train a GAOT model on a set of bluff body shapes and then test it on shapes that were not in the training set. Then, the model is fine-tuned with a few task-specific samples and the results are shown in Fig. 3 (c). We observe that our model performs very well in a *few-shot transfer learning* scenario, with the fine-tuned model providing an almost order of magnitude gain in accuracy over the model, trained from scratch. Finally, in SM Sec. E.4, we demonstrate that GAOT scales with both model and dataset size, with scaling with respect to dataset size, also illustrated in Fig. 3 (c)

Ablations. Summarizing the extensive ablation studies of SM Sec.F, we observed that i) the MAGNO encoder/decoder is clearly superior to message-passing based encoders/decoders, ii) choosing a regular equispaced latent point cloud performs significantly better than either downsampling on the original point cloud or using a projected low-dimensional regular grid, iii) a time-derivative marching strategy, i.e, setting $\gamma = 1, \delta = \tau$ in (7) is superior to other choices of γ, δ , iv) using a statistical geometric embedding performs significantly better than either not using additional geometric information or using a pointnet to process geometric information and v) incorporating *multiscale* features in the MAGNO encoder/decoder provides a significant gain in accuracy when compared to using just a single scale GNO encoder/decoder as in GINO. A posteriori, these observations justify the choices that we have made in designing GAOT and selecting the relevant model components, while also revealing how these innovative features underpin GAOT’s overall performance.

4 Discussion

Summary. We present GAOT, a new neural operator for learning PDE solutions on arbitrary domains. It is based on a novel multiscale GNO encoder/decoder, combined with geometric embeddings that convey statistical information about the local domain geometry, and a (vision) transformer based processor. The model is designed to handle any point cloud input and provide the output at any query point in the underlying domain. Several innovative strategies have been used to make the implementation of GAOT computationally efficient and scalable. We test GAOT on a large number of challenging datasets for a variety of time-dependent and time-independent PDEs over diverse two-dimensional domain geometries to find that GAOT is significantly more accurate, robust and computationally efficient in terms of training throughput and inference latency, over a large set of baselines. We further demonstrate the potential of GAOT by presenting its SOTA performance on a large-scale three-dimensional dataset of industrial simulations. These results demonstrate that GAOT can be a powerful and scalable neural operator with wide-spread applications.

Related Work. As discussed before, there are 3 broad classes of models for learning PDEs on arbitrary domains namely i) end-to-end message-passing based frameworks exemplified here with RIGNO, which significantly improves upon models such as (multiscale) MeshGraphNets [41, 15] ii) Transformer based frameworks such as Transolver [50], GNOT [18] and UPT [1] and iii) frameworks, based on GNO encoders/decoders and FNO processors as in GINO [29]. GAOT differs from all these approaches by a) not using graph-based message passing, b) only employing transformers in the processor c) using a transformer, rather than FNO as a processor and significantly augmenting the GNO encoder/decoder by multiscale features, attention based-quadrature and geometry embeddings. It is precisely these choices, along with a highly efficient implementation, that allows GAOT to significantly surpass GINO, RIGNO, and Transolver in both accuracy and efficiency.

Limitations and Extensions. GAOT’s excellent scalability and ability to generalize very well in a transfer learning setting (Fig. 3c) showcase its potential to serve as the backbone of foundation models for PDEs, extending models such as Poseidon [20] and DPOT [17] to arbitrary domains. Further evaluation of GAOT, beyond the DrivAerNet++ dataset, on three-dimensional datasets is also envisaged in future work. Physics-informed loss functions can be added to GAOT to enable it to act as a physics-informed neural operator as in [30]. We also plan to apply GAOT to downstream tasks such as UQ [34], inverse problems, [37] and PDE constrained optimization [35] to further test its abilities. Finally, our main aim in this paper has been to propose GAOT and test it empirically. We have not yet explored rigorous theoretical properties such as universal approximation results [25, 23]. This limitation will also be addressed in future work.

References

- [1] Benedikt Alkin, Andreas Fürst, Simon Lucas Schmid, Lukas Gruber, Markus Holzleitner, and Johannes Brandstetter. Universal physics transformers: A framework for efficiently scaling neural operators. In *The Thirty-eighth Annual Conference on Neural Information Processing Systems*, 2024.
- [2] Kamyar Azizzadenesheli, Nikola Kovachki, Zongyi Li, Miguel Liu-Schiaffini, Jean Kossaifi, and Anima Anandkumar. Neural operators for accelerating scientific simulations and design. *Nature Reviews Physics*, pages 1–9, 2024.
- [3] Fan Bao, Shen Nie, Kaiwen Xue, Yue Cao, Chongxuan Li, Hang Su, and Jun Zhu. All are worth words: A vit backbone for diffusion models. In *Proceedings of the IEEE/CVF conference on computer vision and pattern recognition*, pages 22669–22679, 2023.
- [4] Francesca Bartolucci, Emmanuel de Bezenac, Bogdan Raonic, Roberto Molinaro, Siddhartha Mishra, and Rima Alaifari. Representation equivalent neural operators: a framework for alias-free operator learning. In *Thirty-seventh Conference on Neural Information Processing Systems*, 2023.
- [5] Francesca Bartolucci, Emmanuel de Bezenac, Bogdan Raonic, Roberto Molinaro, Siddhartha Mishra, and Rima Alaifari. Representation equivalent neural operators: a framework for alias-free operator learning. *Advances in Neural Information Processing Systems*, 36, 2024.
- [6] Johannes Brandstetter, Daniel E. Worrall, and Max Welling. Message passing neural PDE solvers. In *International Conference on Learning Representations*, 2022.
- [7] Eric R Chan, Connor Z Lin, Matthew A Chan, Koki Nagano, Boxiao Pan, Shalini De Mello, Orazio Gallo, Leonidas J Guibas, Jonathan Tremblay, Sameh Khamis, et al. Efficient geometry-aware 3d generative adversarial networks. In *Proceedings of the IEEE/CVF conference on computer vision and pattern recognition*, pages 16123–16133, 2022.
- [8] Qian Chen, Mohamed Elrefaie, Angela Dai, and Faez Ahmed. Tripnet: Learning large-scale high-fidelity 3d car aerodynamics with triplane networks, 2025.
- [9] Ricky TQ Chen, Yulia Rubanova, Jesse Bettencourt, and David K Duvenaud. Neural ordinary differential equations. *Advances in neural information processing systems*, 31, 2018.
- [10] Alexey Dosovitskiy, Lucas Beyer, Alexander Kolesnikov, Dirk Weissenborn, Xiaohua Zhai, Thomas Unterthiner, Mostafa Dehghani, Matthias Minderer, Georg Heigold, Sylvain Gelly, Jakob Uszkoreit, and Neil Houlsby. An image is worth 16x16 words: Transformers for image recognition at scale. In *International Conference on Learning Representations*, 2021.
- [11] Thomas D Economon, Francisco Palacios, Sean R Copeland, Trent W Lukaczyk, and Juan J Alonso. Su2: An open-source suite for multiphysics simulation and design. *Aiaa Journal*, 54(3):828–846, 2016.
- [12] Mohamed Elrefaie, Florin Morar, Angela Dai, and Faez Ahmed. Drivaernet++: A large-scale multimodal car dataset with computational fluid dynamics simulations and deep learning benchmarks, 2025.
- [13] Léonard Equer, T Konstantin Rusch, and Siddhartha Mishra. Multi-scale message passing neural PDE solvers. *arXiv preprint arXiv:2302.03580*, 2023.
- [14] Lawrence C Evans. *Partial differential equations*, volume 19. American Mathematical Society, 2022.
- [15] Meire Fortunato, Tobias Pfaff, Peter Wirsberger, Alexander Pritzel, and Peter Battaglia. Multiscale meshgraphnets. *arXiv preprint arXiv:2210.00612*, 2022.
- [16] Justin Gilmer, Samuel S Schoenholz, Patrick F Riley, Oriol Vinyals, and George E Dahl. Neural message passing for quantum chemistry. In *International conference on machine learning*, pages 1263–1272. PMLR, 2017.

- [17] Zhongkai Hao, Chang Su, Songming Liu, Julius Berner, Chengyang Ying, Hang Su, Anima Anandkumar, Jian Song, and Jun Zhu. DPOT: Auto-regressive denoising operator transformer for large-scale PDE pre-training. In *Forty-first International Conference on Machine Learning*, 2024.
- [18] Zhongkai Hao, Zhengyi Wang, Hang Su, Chengyang Ying, Yinpeng Dong, Songming Liu, Ze Cheng, Jian Song, and Jun Zhu. Gnot: A general neural operator transformer for operator learning. In *International Conference on Machine Learning*, pages 12556–12569. PMLR, 2023.
- [19] Kaiming He, Xiangyu Zhang, Shaoqing Ren, and Jian Sun. Deep residual learning for image recognition. In *Proceedings of the IEEE conference on computer vision and pattern recognition*, pages 770–778, 2016.
- [20] Maximilian Herde, Bogdan Raonic, Tobias Rohner, Roger Käppeli, Roberto Molinaro, Emmanuel de Bezenac, and Siddhartha Mishra. Poseidon: Efficient foundation models for PDEs. In *The Thirty-eighth Annual Conference on Neural Information Processing Systems*, 2024.
- [21] Yicong Hong, Kai Zhang, Jiuxiang Gu, Sai Bi, Yang Zhou, Difan Liu, Feng Liu, Kalyan Sunkavalli, Trung Bui, and Hao Tan. Lrm: Large reconstruction model for single image to 3d. *arXiv preprint arXiv:2311.04400*, 2023.
- [22] Nikola Kovachki, Zongyi Li, Burigede Liu, Kamyar Azizzadenesheli, Kaushik Bhattacharya, Andrew Stuart, and Anima Anandkumar. Neural operator: Learning maps between function spaces with applications to pdes. *Journal of Machine Learning Research*, 24(89):1–97, 2023.
- [23] Nikola Kovachki, Samuel Lanthaler, and Siddhartha Mishra. On universal approximation and error bounds for fourier neural operators. *Journal of Machine Learning Research*, 22:Art–No, 2021.
- [24] Brenda Kulfan. *A Universal Parametric Geometry Representation Method - "CST"*.
- [25] Samuel Lanthaler, Siddhartha Mishra, and George E Karniadakis. Error estimates for Deep-ONets: A deep learning framework in infinite dimensions. *Transactions of Mathematics and Its Applications*, 6(1):tnac001, 2022.
- [26] Zongyi Li, Daniel Zhengyu Huang, Burigede Liu, and Anima Anandkumar. Fourier neural operator with learned deformations for pdes on general geometries. *Journal of Machine Learning Research*, 24(388):1–26, 2023.
- [27] Zongyi Li, Nikola Kovachki, Kamyar Azizzadenesheli, Burigede Liu, Kaushik Bhattacharya, Andrew Stuart, and Anima Anandkumar. Fourier neural operator for parametric partial differential equations. *arXiv preprint arXiv:2010.08895*, 2020.
- [28] Zongyi Li, Nikola Kovachki, Kamyar Azizzadenesheli, Burigede Liu, Kaushik Bhattacharya, Andrew Stuart, and Anima Anandkumar. Neural operator: Graph kernel network for partial differential equations. *arXiv preprint arXiv:2003.03485*, 2020.
- [29] Zongyi Li, Nikola Borislavov Kovachki, Chris Choy, Boyi Li, Jean Kossaifi, Shourya Prakash Otta, Mohammad Amin Nabian, Maximilian Stadler, Christian Hundt, Kamyar Azizzadenesheli, and Anima Anandkumar. Geometry-informed neural operator for large-scale 3d PDEs. In *Thirty-seventh Conference on Neural Information Processing Systems*, 2023.
- [30] Zongyi Li, Hongkai Zheng, Nikola Kovachki, David Jin, Haoxuan Chen, Burigede Liu, Kamyar Azizzadenesheli, and Anima Anandkumar. Physics-informed neural operator for learning partial differential equations. *ACM/JMS Journal of Data Science*, 1(3):1–27, 2024.
- [31] Levi E. Lingsch, Mike Yan Michelis, Emmanuel de Bezenac, Sirani M. Perera, Robert K. Katzschmann, and Siddhartha Mishra. Beyond regular grids: Fourier-based neural operators on arbitrary domains. In *Forty-first International Conference on Machine Learning*, 2024.
- [32] Adrien Loseille, Alain Dervieux, Pascal Frey, and Frédéric Alauzet. Achievement of global second order mesh convergence for discontinuous flows with adapted unstructured meshes. In *18th AIAA computational fluid dynamics conference*, page 4186, 2007.

- [33] Lu Lu, Pengzhan Jin, Guofei Pang, Zhongqiang Zhang, and George Em Karniadakis. Learning nonlinear operators via DeepONet based on the universal approximation theorem of operators. *Nature Machine Intelligence*, 3(3):218–229, 2021.
- [34] Kjetil O Lye, Siddhartha Mishra, and Deep Ray. Deep learning observables in computational fluid dynamics. *Journal of Computational Physics*, page 109339, 2020.
- [35] Kjetil O. Lye, Siddhartha Mishra, Deep Ray, and Praveen Chandrashekar. Iterative surrogate model optimization (ISMO): An active learning algorithm for PDE constrained optimization with deep neural networks. *Computer Methods in Applied Mechanics and Engineering*, 374:113575, 2021.
- [36] Siddhartha Mishra and Alex (Eds.) Townsend. *Numerical Analysis meets Machine Learning*. Handbook of Numerical Analysis. Springer, 2024.
- [37] R. Molinaro, y. Yang, E. Engquist, and S Mishra. Neural inverse operators for solving pde inverse problems. *arXiv:2301.11167*, 2023.
- [38] Roberto Molinaro, Samuel Lanthaler, Bogdan Raonić, Tobias Rohner, Victor Armegioiu, Stephan Simonis, Dana Grund, Yannick Ramic, Zhong Yi Wan, Fei Sha, Siddhartha Mishra, and Leonardo Zepeda-Núñez. Generative ai for fast and accurate statistical computation of fluids, 2025.
- [39] Sepehr Mousavi, Shizheng Wen, Levi Lingsch, Maximilian Herde, Bogdan Raonić, and Siddhartha Mishra. Rigno: A graph-based framework for robust and accurate operator learning for pdes on arbitrary domains, 2025.
- [40] Jens-Dominik Muller. *On triangles and flow*. University of Michigan, 1996.
- [41] Tobias Pfaff, Meire Fortunato, Alvaro Sanchez-Gonzalez, and Peter Battaglia. Learning mesh-based simulation with graph networks. In *International Conference on Learning Representations*, 2021.
- [42] Charles R. Qi, Hao Su, Kaichun Mo, and Leonidas J. Guibas. Pointnet: Deep learning on point sets for 3d classification and segmentation, 2017.
- [43] Charles R Qi, Hao Su, Kaichun Mo, and Leonidas J Guibas. Pointnet: Deep learning on point sets for 3d classification and segmentation. In *Proceedings of the IEEE conference on computer vision and pattern recognition*, pages 652–660, 2017.
- [44] A. Quarteroni and A. Valli. *Numerical approximation of Partial differential equations*, volume 23. Springer, 1994.
- [45] Bogdan Raonic, Roberto Molinaro, Tim De Ryck, Tobias Rohner, Francesca Bartolucci, Rima Alaifari, Siddhartha Mishra, and Emmanuel de Bezenac. Convolutional neural operators for robust and accurate learning of PDEs. In *Thirty-seventh Conference on Neural Information Processing Systems*, 2023.
- [46] Alvaro Sanchez-Gonzalez, Jonathan Godwin, Tobias Pfaff, Rex Ying, Jure Leskovec, and Peter Battaglia. Learning to simulate complex physics with graph networks. In *International conference on machine learning*, pages 8459–8468. PMLR, 2020.
- [47] Alvaro Sanchez-Gonzalez, Nicolas Heess, Jost Tobias Springenberg, Josh Merel, Martin Riedmiller, Raia Hadsell, and Peter Battaglia. Graph networks as learnable physics engines for inference and control. In *International Conference on Machine Learning*, pages 4470–4479. PMLR, 2018.
- [48] Jianlin Su, Murtadha Ahmed, Yu Lu, Shengfeng Pan, Wen Bo, and Yunfeng Liu. Roformer: Enhanced transformer with rotary position embedding. *Neurocomputing*, 568:127063, 2024.
- [49] A Vaswani. Attention is all you need. *Advances in Neural Information Processing Systems*, 2017.
- [50] Haixu Wu, Huakun Luo, Haowen Wang, Jianmin Wang, and Mingsheng Long. Transolver: A fast transformer solver for PDEs on general geometries. In *Forty-first International Conference on Machine Learning*, 2024.

Supplementary Material for: Geometry Aware Operator Transformer as an Efficient and Accurate Neural Surrogate for PDEs on Arbitrary Domains

A Details of Problem Formulation.

Here, we introduce the core concepts of *operator learning* for both time-dependent and time-independent partial differential equations (PDEs). We begin by defining the general forms of PDEs under consideration and then discuss the associated operator-learning tasks.

A.1 General Forms of PDEs

We focus on two broad classes of PDEs: time-dependent and time-independent.

Time-Dependent PDE. Let $D \subset \mathbb{R}^d$ be a d -dimensional spatial domain, and let $(0, T)$ denote the time interval. A general time-dependent PDE (see Main Text Eqn. (2)) can be written as

$$\begin{aligned} \frac{\partial}{\partial t} u(t, x) + \mathcal{D}(c, t, u, \nabla_x u, \nabla_x^2 u, \dots) &= 0, & \forall (t, x) \in (0, T) \times D, \\ \mathcal{B}(u, \nabla_x u, \nabla_x^2 u, \dots) &= u_b, & \forall (t, x) \in (0, T) \times \partial D, \\ u(0, x) &= u_0(x), & \forall x \in D, \end{aligned} \quad (\text{A.1})$$

where

- $u(t, x)$ is the PDE solution in $(0, T) \times D$;
- $c(t, x)$ is a known, possibly spatio-temporal parameter (e.g., a material coefficient or source term);
- \mathcal{D} is a (spatial) differential operator;
- \mathcal{B} is a boundary operator acting on ∂D ;
- $u_b(x)$ are boundary values;
- $u_0(x)$ is the initial condition at $t = 0$.

We assume $u(t, \cdot) \in \mathcal{X} \subset L^p(D; \mathbb{R}^m)$ for some $1 \leq p < \infty$ and integer $m \geq 1$. Likewise, $u_0(x) \in \mathcal{X}^0 \subset \mathcal{X}$ is an element of the initial-condition space, and $c \in \mathcal{Q} \subset L^p(\bar{D}; \mathbb{R}^m)$ is taken from a parameter space.

Time-Independent PDE. A time-independent (steady-state) PDE of the general form (Main Text Eqn. (1)) can be written as

$$\begin{aligned} \mathcal{D}(c, \bar{u}, \nabla_x \bar{u}, \nabla_x^2 \bar{u}, \dots) &= f, & \forall x \in D, \\ \mathcal{B}(\bar{u}, \nabla_x \bar{u}, \nabla_x^2 \bar{u}, \dots) &= u_b, & \forall x \in \partial D, \end{aligned} \quad (\text{A.2})$$

where $\bar{u}(x) \in \mathcal{X}$ and $c(x) \in \mathcal{Q}$ are now independent of t and f is a source term. In certain scenarios, one may view (A.2) as the long-time limit of (A.1), i.e.,

$$\bar{u}(x) = \lim_{t \rightarrow \infty} u(t, x). \quad (\text{A.3})$$

Hence, much of the theory for time-dependent PDEs can be adapted to time-independent problems by recognizing steady-state solutions as limiting cases.

A.2 Solution Operators for PDEs

Let us denote the solution to the time-dependent PDE (A.1) by

$$u(t, \cdot) = \mathcal{S}(a, c, t), \quad (\text{A.4})$$

where $\mathcal{S} : \mathcal{X}^0 \times \mathcal{Q} \times (0, T) \rightarrow \mathcal{X}$ is the *solution operator*, mapping any initial datum $u_0 \in \mathcal{X}^0$ (and parameter functions $c \in \mathcal{Q}$) to the solution $u(t)$ at time t .

542 **Time-Shifted Operator.** In many operator-learning strategies, it is useful to consider a *time-shifted*
 543 *operator* that predicts solutions at a future time from a current snapshot. Specifically, define

$$\mathcal{S}^\dagger : \mathcal{X} \times \mathcal{Q} \times (0, T) \times \mathbb{R}^+ \longrightarrow \mathcal{X},$$

544 such that

$$\mathcal{S}^\dagger(u^t, c^t, t, \tau) = \mathcal{S}^t(u^t, c^t, \tau) = u^{t+\tau}. \quad (\text{A.5})$$

545 Here, $u^t = u(t, \cdot)$ is the solution snapshot at time t , which now serves as an initial condition on the
 546 restricted time interval (t, T) . Likewise, c^t is the corresponding parameter snapshot at time t .

547 **Steady-State Operator.** For the time-independent PDE (A.2), we define

$$\bar{\mathcal{S}} : \mathcal{Q} \longrightarrow \mathcal{X} \quad (\text{A.6})$$

548 to be the analogous solution operator, such that $\bar{u} = \bar{\mathcal{S}}(c)$ solves the boundary-value problem for
 549 any parameter/boundary data c . Although many operator-learning methods primarily focus on the
 550 time-dependent form \mathcal{S} , the same ideas apply to steady-state problems by treating \bar{u} as a limiting
 551 case.

552 **Operator Learning Task (OLT).** A central goal is to approximate these solution operators without
 553 repeatedly resorting to expensive, high-fidelity numerical solvers. Formally, the OLT can be stated as:

554 *Given a data distribution $\mu \in \text{Prob}(\mathcal{X}^0) \times \mathcal{Q}$ for initial/boundary conditions*
 555 *and parameters $c \in \mathcal{Q}$, learn an approximation $\mathcal{S}^* \approx \mathcal{S}$ to the true solution*
 556 *operator \mathcal{S} . That is, for any $a \sim \mu$, we want $\mathcal{S}^*(t, a)$ to closely approximate $u(t)$*
 557 *for all $t \in [0, T]$. For time-independent problems, this goal changes accordingly to*
 558 *learning $\bar{\mathcal{S}}^* \approx \bar{\mathcal{S}}$.*

559 A.3 Discretizations.

560 In practice, we only have access to a *discretized form* of the data as the labelled data is generated
 561 either through experiments/observations or numerical simulations. In both cases, we can only evaluate
 562 the inputs and outputs to the underlying solution operator at discrete points.

563 We start by describing these discretizations for the time-independent PDE (A.2). To this end, fix
 564 the i -th sample and let $D_{\Delta^{(i)}} = \{x_j^{(i)} \in D^{(i)}\}$, for $1 \leq j \leq J^{(i)}$ denote a set of *sampling points*
 565 on the underlying domain $D^{(i)}$. Observe that the underlying domain itself can be an input to the
 566 solution operator $\bar{\mathcal{S}}$ of (A.2). We assume access to the functions $(c^{(i)}(x_j), f^{(i)}(x_j), u^{(i)}(x_j))$ and
 567 the corresponding discretized boundary values. Denoting these discretized inputs and outputs as
 568 $a_{\Delta^{(i)}}^{(i)}$ (where $a = (c, f, u_b)$) and $u_{\Delta^{(i)}}^{(i)}$, respectively, the underlying learning task boils down to
 569 approximating $\bar{\mathcal{S}}_{\# \mu}$ from the discretized data-pairs $(a_{\Delta^{(i)}}^{(i)}, u_{\Delta^{(i)}}^{(i)})$. Note that although the data is
 570 given in a discretized form, we still require that our operator learning algorithm can provide values of
 571 the output function u at any *query point* $x \in D$.

572 For the time-dependent PDE (A.1), in addition to the spatial discretization $D_{\Delta^{(i)}} = \{x_j^{(i)} \in D^{(i)}\}$,
 573 for $1 \leq j \leq J^{(i)}$, we only have access to data at time snapshots $t_n^{(i)} \in [0, T^{(i)}]$. Thus, the data to the
 574 time-dependent operator learning task consists of inputs $(c^{(i)}(x_j), u_0^{(i)}(x_j))$ and outputs $u(x_j^{(i)}, t_n^{(i)})$,
 575 from which the space- and time-continuous solution operator \mathcal{S}_t has to be learned at every query
 576 point $x \in D$ and time point $t \in [0, T]$.

577 Summarizing, for both time-independent and time-dependent PDEs, the operator learning task
 578 amounts to approximating the underlying (space-time) continuous solution operators, given dis-
 579 cretized data-pairs.

580 B Details of GAOT Architecture

581 This appendix provides a detailed explanation of the core components of the GAOT model architecture,
 582 including the choice of latent token grid, the Multiscale Attentional Graph Neural Operator (MAGNO)
 583 used in the encoder and decoder, the geometry embedding mechanisms, and the transformer-based
 584 processor.

B.1 Choice of Latent Grid

Given the input point cloud, denoted by D_Δ above, the first step in our design is to select a *latent* point cloud, consisting of points at which our spatial tokens are going to be specified. Here, we explore three distinct ways of choosing spatial tokens, each offering different trade-offs in terms of computational cost, geometric coverage, and ease of patching for efficient attention. Figure B.1 schematically illustrates these strategies.

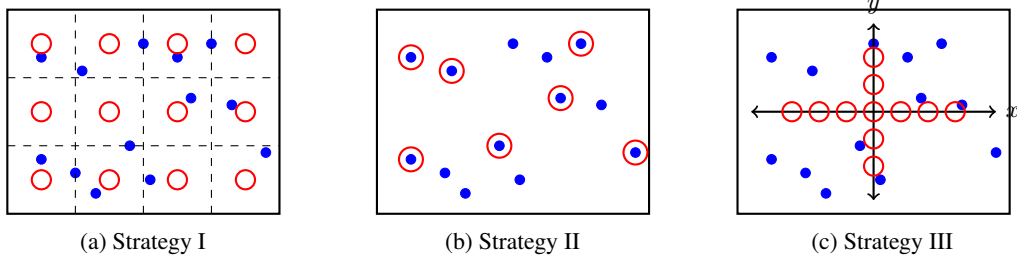


Figure B.1: Schematic illustration of the three tokenization strategies in a 2D domain. Blue points and red circles corresponding to physical grid and latent token grid, respectively. (a) A structured stencil grid overlaying the domain. (b) Downsampled unstructured points used directly as tokens. (c) Projecting the 2D domain onto low-dimensional planes.

Structured Stencil Grid (Strategy I). In this approach, we overlay a structured grid of tokens across D_Δ . For 2D domains, this may be a uniform mesh of cells; for 3D domains, an analogous dense grid can be used. GINO [29] is a good example for the use of such latent grids.

- *Advantages.* This grid can be quite fine if needed, ensuring adequate coverage. Moreover, we can group tokens into patches before feeding them into the transformer processor (see below), effectively reducing the token count (number of latent points). Our following experiments in SM Sec. F.2 suggest that patch size has a negligible effect on performance; hence, one can choose large patches to speed up training.
- *Limitations.* The main drawback is that token count grows exponentially with the dimension; for 3D, the number of grid cells can be prohibitively large. Also, if the input data lie on a low-dimensional manifold embedded in D_Δ , some tokens may remain underutilized. Nonetheless, we find in practice that even empty tokens (those with no neighboring input points) can still contribute to better global encoding and improved convergence.

Downsampled Unstructured Points (Strategy II). This method directly downsamples the input unstructured point cloud and treat each sampled point as a token, RIGNO [39] and UPT [1] are typical methods based on this strategy. If the data are denser in some regions, naturally more tokens appear there.

- *Advantages.* This method avoids the pitfalls of having many tokens in empty regions, as might happen if the data indeed lie on a lower-dimensional manifold. By adaptive sampling, it can allocate tokens more efficiently.
- *Limitations.* Unstructured tokens are harder to patch effectively for attention mechanisms in the processor. In a following experiment, we observed that this strategy can be less effective than Strategy I even when the domain is indeed partially low-dimensional.

Projected Low-Dimensional Grid (Strategy III). Inspired by certain 3D computer vision models [7, 21], one can project the 3D domain (or higher-dimensional space) into a lower-dimensional representation and then place a structured stencil grid in the reduced coordinates—for example, using triplane embeddings in 3D [8].

- *Advantages.* Such a projection drastically reduces the token count in 3D, and avoids the purely *low-dimensional manifold* disadvantage of Strategy I. Moreover, one can still apply patching on the structured plane.
- *Limitations.* Decomposing d -dimensional coordinates into disjoint projections (e.g., splitting x, y, z axes) can introduce additional approximation errors. Some local neighborhood

information is inevitably lost during the projection. This trade-off can degrade the final accuracy compared to direct methods (Strategy I or II).

In this paper, we mainly adopt Strategy I, i.e. a *structured stencil grid*, for all experiments due to its robustness and simplicity. While using a stencil grid indeed creates some empty tokens in low-density regions, we consistently observe fast convergence and strong generalization across various PDE datasets, see the ablation studies in SM Sec. F.2.

B.2 Multiscale Attentional Graph Neural Operator

Both the encoder and decoder in GAOT (see Figure 2 in the main text) employ the proposed Multiscale Attentional Graph Neural Operator (MAGNO). MAGNO is designed to augment classical Graph Neural Operators (GNOs) by incorporating multiscale information processing and attention-based weighting. A traditional GNO constructs a local graph for each query point (or token) by collecting all neighboring nodes within a specified radius, approximating a (kernel) integral operator over this local neighborhood. Below, we first recap the standard single-scale GNO scheme, then extend it to a multiscale version, and finally incorporate attention mechanisms for adaptive weighting.

Recap of Single-Scale Local Integration (GNO Basis) For any point y in the latent space \mathcal{D} (in the encoder) or a query point x in the original domain D_Δ (in the decoder), a GNO layer aims to aggregate information from its neighborhood via a kernel integral. For the encoder, given input data $a(x_j)$ on the original point cloud $D_\Delta = \{x_j\}$, the GNO transforms it into latent features $w_e(y)$. The fundamental GNO computation is given by Eq. (3) from the main text:

$$\tilde{w}_e(y) = \sum_{k=1}^{n_y} \alpha_k K(y, x_k, a(x_k)) \varphi(a(x_k)) \quad (\text{B.1})$$

where the sum is over n_y points x_k in the original point cloud D_Δ such that $|y - x_k| \leq r$. K and φ are MLPs, $a(x_k)$ is the input feature at point x_k , and α_k are given quadrature weights. This form can be seen as a discrete approximation of an integral operator:

$$\int_{B_r(y) \cap D_\Delta} K(y, x', a(x')) \varphi(a(x')) dx' \quad (\text{B.2})$$

where $B_r(y)$ is a ball of radius r centered at y .

Multiscale Neighborhood Construction The single-scale approach, while effective for capturing local interactions within a fixed radius r , may not efficiently perceive multiscale information crucial for many PDE problems. To address this, we introduce multiple radii. As described in the main text, we choose $r_m = s_m r_0$, where r_0 is a base radius and s_m are scale factors ($m = 1, \dots, \bar{m}$). For each scale m , we gather points x_k from the original point cloud D_Δ within the ball $B_{r_m}(y)$ centered at $y \in \mathcal{D}$ (for the encoder) with radius r_m . A GNO-like local integration is then performed for each scale m , as shown in Eq. (4) from the main text:

$$\tilde{w}_e^m(y) = \sum_{k=1}^{n_y^m} \alpha_k^m K^m(y, x_k, a(x_k)) \varphi(a(x_k)) \quad (\text{B.3})$$

Here, n_y^m is the number of neighbors x_k within radius r_m . The MLPs K^m and φ can be scale-specific or share parameters across scales. This paper chooses the shared parameters across all scales.

B.2.1 Attentional Weighting in Local Integration (AGNO)

In the main text, we further propose an attention-based choice for the quadrature weights α_k^m , as given by Eq. (5):

$$\alpha_k^m = \frac{\exp(e_k^m)}{\sum_{k'=1}^{n_y^m} \exp(e_{k'}^m)}, \quad e_k^m = \frac{\langle \mathbf{W}_q^m y, \mathbf{W}_\kappa^m x_k \rangle}{\sqrt{\bar{d}}} \quad (\text{B.4})$$

where $\mathbf{W}_q^m, \mathbf{W}_\kappa^m \in \mathbb{R}^{\bar{d} \times d}$ (assuming original and latent coordinate dimension d , and attention dimension \bar{d}) are learnable query and key matrices. This mechanism allows the model to dynamically assign contribution weights to each neighbor x_k based on the relationship between y and x_k . This forms the final form of our Attentional Graph Neural Operator or AGNO at each scale m .

662 B.2.2 Attentional Fusion of Multiscale Features

663 After computing the AGNO features $\hat{w}_e^m(y)$ for each scale (which are then fused with geometry
 664 embeddings, detailed in Sec. B.3, to form $\hat{w}^m(y)$), we need to integrate this information from
 665 different scales. As described in the main text (Fig. 2 and Eq. (6)), instead of simple summation or
 666 concatenation, we introduce a small MLP ψ_m to learn the relative contribution of each scale to the
 667 final encoded feature $w_e(y)$:

$$w_e(y) = \sum_{m=1}^{\bar{m}} \beta_m(y) \hat{w}^m(y), \quad \beta_m(y) = \frac{\exp(\psi_m(y))}{\sum_{m'=1}^{\bar{m}} \exp(\psi_{m'}(y))} \quad (\text{B.5})$$

668 Here, $\psi_m(y)$ is typically computed based on coordinates of y . $\beta_m(y)$ is the attention weight for the
 669 m -th scale at point y .

670 The final output of the MAGNO encoder, $w_e(y)$, is thus a feature representation that adaptively
 671 weights and fuses multiscale local information with attention mechanisms. The MAGNO in the
 672 decoder follows the exact same structure, with different inputs, outputs, and operating objects, as
 673 described in the Main Text.

674 B.3 Geometry Embeddings

675 While the Multiscale Attentional GNO already leverages geometric structure via local neighborhoods,
 676 one often needs to incorporate more explicit shape or domain information in practical PDE scenarios.
 677 For instance, when the geometry of the domain itself (e.g., the shape of an airfoil) plays a critical
 678 role in the solution operator, coordinates alone may be insufficient to encode all the necessary
 679 geometric priors. Therefore, we introduce geometry embeddings to enhance the model’s geometric
 680 awareness. These embeddings work in tandem with the MAGNO encoder (and decoder), providing a
 681 rich geometric description for each token (latent point y) and its neighborhood at various scales m .

682 Prior work on including geometric information in neural PDE solvers typically resorts to two major
 683 approaches: (i) appending geometry features directly into node/edge attributes [39], or (ii) using a
 684 signed distance function (SDF) [29]. However, we argue that:

- 685 • Simply merging geometry and physical features at the node level may entangle them
 686 prematurely, potentially hurting performance when the geometry is complex or when
 687 additional modalities (e.g. material properties) must be fused.
- 688 • Computing SDF to represent geometry is often cumbersome, especially for unstructured
 689 datasets or when the boundary is only partially known. Each new shape would require
 690 re-computation, and the SDF values may be inaccurate if the surface is not well-defined.

691 Instead, we advocate two more direct and flexible mechanisms for extracting geometric descriptors:
 692 local *Statistical embedding* and *PointNet-based embedding*, shown in Figure B.2.

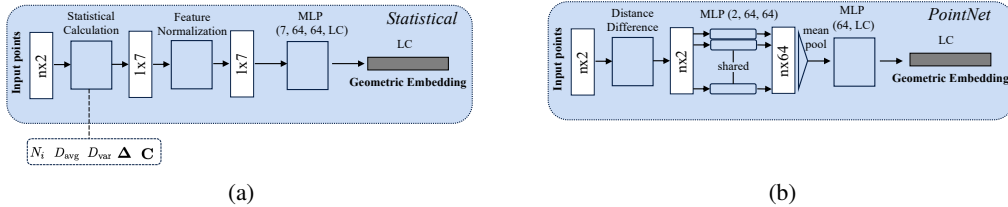


Figure B.2: Schematic of the Geometric Embedding for Statistical Embedding (a) and PointNet-based Embedding (b). LC denotes the lifting channels for MAGNO output.

693 **Local Statistical Embedding** The core idea is to extract statistical descriptors from the neighbor-
 694 hood $B_{r_m}(y)$ (or $B_{\hat{r}_m}(x)$ for the decoder) of original point cloud points x_k (or latent points y_ℓ for
 695 the decoder) for each latent point y (for the encoder) or query point x (for the decoder) at each scale
 696 m . Taking the encoder as an example, for a latent point $y \in \mathcal{D}$ and scale m , its neighborhood is
 697 $N_m(y) = \{x_k \in \mathcal{D}_\Delta : |y - x_k| \leq r_m\}$, containing n_y^m points. We compute the following statistics:

- 698 • Number of Neighbors n_y^m : Measures local density around point y .

699

- Average Distance $D_{\text{avg}}^m(y)$:

$$D_{\text{avg}}^m(y) = \frac{1}{n_y^m} \sum_{k=1}^{n_y^m} |y - x_k| \quad (\text{B.6})$$

700

Describes the average spatial extent of the neighborhood.

701

- Distance Variance $D_{\text{var}}^m(y)$:

$$D_{\text{var}}^m(y) = \frac{1}{n_y^m} \sum_{k=1}^{n_y^m} (|y - x_k| - D_{\text{avg}}^m(y))^2 \quad (\text{B.7})$$

702

Reflects the dispersion of points within the neighborhood.

703

- Neighbor Centroid Offset Vector Δ_y^m :

$$\Delta_y^m = \left(\frac{1}{n_y^m} \sum_{k=1}^{n_y^m} x_k \right) - y \quad (\text{B.8})$$

704

The vector from y to the centroid of its neighbors x_k .

705

- PCA Features: These features aim to capture the local shape anisotropy of the distribution of the n_y^m neighbor points $\{x_k\}$ within the m -th scale ball $B_{r_m}(y)$. This is achieved by performing PCA on the set of these neighbor coordinates $\{x_k\}$. Using the centroid of the neighbors $\bar{x}_{\text{nbrs},y}^m = \left(\frac{1}{n_y^m} \sum_{k=1}^{n_y^m} x_k \right)$, the $d \times d$ covariance matrix of the neighbor coordinates is calculated as:

709

$$\mathbf{C}_y^m = \frac{1}{n_y^m} \sum_{k=1}^{n_y^m} (x_k - \bar{x}_{\text{nbrs},y}^m)(x_k - \bar{x}_{\text{nbrs},y}^m)^\top \quad (\text{B.9})$$

710

If $n_y^m = 0$ (or too few points for a meaningful covariance, e.g. $n_y^m < d$), the covariance matrix \mathbf{C}_y^m is treated as a zero matrix, leading to zero eigenvalues. Otherwise, the d real eigenvalues of this symmetric, positive semi-definite covariance matrix, sorted in descending order ($\lambda_1^m \geq \lambda_2^m \geq \dots \geq \lambda_d^m \geq 0$), are used as the PCA features. These eigenvalues represent the variance of the neighbor data along the principal component directions, thus describing the extent and orientation of the local point cloud cluster.

711

712

713

714

715

716 These statistical descriptors, computed for each scale m and each point $y \in \mathcal{D}$, are concatenated into
717 a vector z_y^m , normalized (e.g., to have zero mean and unit variance for each component), and then fed
718 into an MLP to yield the geometry embedding $g^m(y)$ for that scale:

$$g^m(y) = \text{MLP}_{\text{geo}}(\text{Normalize}(z_y^m)) \quad (\text{B.10})$$

719

This MLP_{geo} is typically shared across all points and scales.

720

721

722

Point-Based Embedding As an alternative, we can train a PointNet-style network [43] to derive a compact geometric descriptor from each token's neighborhood. Classical PointNet architectures typically include:

723

- Input Transformer: aligns input points to a canonical space (optional),

724

- Shared MLP: processes each point individually,

725

- Symmetric Pooling: aggregates per-point features into a global descriptor, ensuring permutation invariance.

726

727

In our PDE setting, we do not necessarily need an input transformer; the local coordinates can directly serve as input features. We replace the typical max-pooling with mean-pooling to produce smoother local embeddings (though other pooling strategies are also possible). For a point y and scale m , we collect the relative coordinates of its neighbors $\{\delta_k^m = x_k - y\}_{k=1}^{n_y^m}$. These relative coordinates are fed into a shared MLP (point-wise MLP):

730

$$h_k^m = \text{MLP}_{\text{pt}}(\delta_k^m) \quad (\text{B.11})$$

Then, a symmetric pooling operation (e.g., mean pooling or max pooling) aggregates these per-point features into a global geometric feature:

$$\bar{h}^m(y) = \text{MeanPool}(\{h_k^m\}_{k=1}^{n_y^m}) = \frac{1}{n_y^m} \sum_{k=1}^{n_y^m} h_k^m \quad (\text{B.12})$$

This aggregated feature $\bar{h}^m(y)$ can optionally be passed through another small MLP to produce the final geometry embedding $g^m(y)$.

B.3.1 Integration of Geometry Embeddings in MAGNO

As depicted in Fig. 2 of the main text and described in the MAGNO paragraph, in the MAGNO component of the encoder (or decoder), the geometry embedding is fused with the AGNO output at each scale. The specific workflow (for the encoder) is as follows:

1. **Scale-Specific AGNO Features:** For latent point y and scale m , compute the AGNO output $\tilde{w}_e^m(y)$ (as described in Sec. B.2.1).
2. **Scale-Specific Geometry Embedding:** In parallel, using methods from Sec. B.3, compute the geometry embedding $g^m(y)$ from the same neighborhood $N_m(y)$.
3. **Feature Fusion:** Concatenate the AGNO features $\tilde{w}_e^m(y)$ and the geometry embedding $g^m(y)$, and pass them through an MLP for fusion, yielding the scale-specific latent feature function $\hat{w}^m(y)$:

$$\hat{w}^m(y) = \text{MLP}_{\text{fuse}}^m([\tilde{w}_e^m(y) \parallel g^m(y)]) \quad (\text{B.13})$$

where \parallel denotes concatenation. And $\text{MLP}_{\text{fuse}}^m$ is shared across scales.

4. **Multiscale Aggregation:** Finally, as described in Sec. B.2.2, an attention mechanism is used to perform a weighted sum of the fused features $\{\hat{w}^m(y)\}_{m=1}^{\bar{m}}$ from all scales, yielding the final encoder output $w_e(y)$ (Eq. (B.5)).

Compared to merging geometry and PDE features at the node level before any operator updates, this *per-scale* integration offers several benefits:

- **Scale-Adapted Geometry.** Each scale has a correspondingly sized neighborhood, allowing the geometric embedding to reflect local shape details at the appropriate radius. Small radii capture fine-grained features (e.g. sharp corners), while large radii convey coarse global context.
- **Modular Flexibility.** Both MAGNO and Geometric Embeddings act as distinct modules. One can upgrade either component (e.g. adopting a more customized local aggregator or geometry encoder) without changing the overall pipeline.
- **Unified Per-Token Fusion.** The final aggregated feature $w_e(y)$ collects information from all relevant scales and from geometric descriptors, leading to a richer token representation. This is particularly advantageous in settings with complex boundaries (e.g. airfoils, porous media) where multiple length scales and shape cues matter.

This design preserves the encode-process-decode philosophy: each token gains geometry-aware, multiscale PDE features during the encoder stage, facilitating global attention and final decoding later in the pipeline.

B.4 Processor

After constructing geometry-aware tokens, we employ a Transformer-based processor to enable global message passing among all tokens. Depending on the chosen tokenization strategy (SM B.1), we can choose the following strategies, respectively:

- **Regular Grid (Strategy I or III):** If the latent points $\{y_\ell \in \mathcal{D}\}$ lie on a regular grid (e.g., via a structured stencil or a projected low-dimensional regular grid), we adopt a strategy similar to vision transformers (ViTs) [10]. The latent points are grouped into non-overlapping "patches." All token features $w_e(y)$ within each patch are flattened and linearly projected into a single patch token embedding. These patch tokens then serve as the input sequence to the Transformer.

- Randomly Downsampled Points (Strategy II): If the latent points $\{y_\ell\}$ are randomly downsampled from the original point cloud D_Δ , they lack a regular grid structure. In this case, there is no obvious "patching" method, and each latent token $w_e(y_\ell)$ directly serves as an element in the Transformer's input sequence.

Positional Encoding Transformers themselves are permutation-invariant and do not inherently process sequential order or spatial position. Thus, positional information must be injected. In GAOT, we use the Relative Positional Embeddings (RoPE) [48], which is a method that integrates relative positional information directly into the self-attention mechanism. It achieves this by applying rotations, dependent on their relative positions, to the Query and Key vectors. This has shown strong performance in many Transformer models.

Transformer Block Structure For the transformer Blocks, we adopt an RMS norm $\text{RMSNorm}(\cdot)$ at the beginning of attention and feedforward layers:

$$\mathbf{z} = \text{RMSNorm}(\mathbf{x}), \quad \text{RMSNorm}(\mathbf{x}) = \frac{\mathbf{x}}{\sqrt{\text{mean}(\mathbf{x}^2)}} \odot \boldsymbol{\alpha} \quad (\text{B.14})$$

where $\boldsymbol{\alpha}$ is a learned scaling parameter. This approach is akin to LayerNorm but uses the root mean square of feature magnitudes rather than computing mean-and-variance separately. This prenorm design helps stabilize the gradient flow compared to the conventions in [49]. Each block has the structure,

$$\mathbf{Z}_{\text{attn}} = \mathbf{X} + \text{MultiHeadAttn}(\text{RMSNorm}(\mathbf{X})), \quad \mathbf{Z}_{\text{ffn}} = \mathbf{Z}_{\text{attn}} + \text{FFN}(\text{RMSNorm}(\mathbf{Z}_{\text{attn}})). \quad (\text{B.15})$$

Furthermore, we use *Group Query* and *Flash Attention* in the code for efficient multi-head self-attention.

Long-Range Skip Connections In addition to the intra-block residual connections, we also introduce long-range skip connections across multiple Transformer blocks, as suggested in works like [3]. For instance, the Transformer blocks can be divided into an earlier part and a later part, and layers can be symmetrically connected (e.g., the first with the last, the second with the second-to-last, etc.), allowing later blocks to directly receive information from earlier blocks, further improving information flow.

By stacking these blocks, the Transformer processor learns complex global dependencies among tokens, transforming the locally geometry-aware tokens $w_e(y_\ell)$ from the encoder into processed tokens $w_p(y_\ell)$ that incorporate richer contextual information. These processed tokens are then converted by the MAGNO decoder to the desired approximation of the output of the underlying solution operator (see Main Text and Fig. ??)

B.5 Training Details.

This section discusses the details of how the GAOT models were trained, including the loss functions, data normalization procedures, general training hyperparameters, and default model configurations. In our experiments, we address both time-independent and time-dependent PDEs. The application of GAOT to time-independent PDEs is straightforward. For time-dependent PDEs, we employ three different time-stepping methods and all2all training [20], as discussed in the main text. More details on these methods can be found in [39].

B.5.1 Loss Function

The loss function used for training GAOT is the Mean Squared Error (MSE), computed between the model's final predictions and the true physical quantities. For a set of N_s samples and N_p spatial points, the loss is:

$$\mathcal{L}_{\text{MSE}} = \frac{1}{N_s N_p} \sum_{i=1}^{N_s} \sum_{j=1}^{N_p} \|\mathcal{S}_\theta(\cdot)_i(x_j) - \mathbf{u}_{\text{true},i}(x_j)\|_2^2 \quad (\text{B.16})$$

where $\mathcal{S}_\theta(\cdot)_i(x_j)$ is the model's prediction for sample i at point x_j , and $\mathbf{u}_{\text{true},i}(x_j)$ is the corresponding ground truth. The exact form of $\mathcal{S}_\theta(\cdot)$ depends on whether the problem is time-independent or time-dependent.

819 **Time-Independent PDEs.** For time-independent PDEs, given an input $a(x_j)$ (e.g., boundary
820 conditions, coefficients c), GAOT directly predicts the solution $u(x_j)$. Thus, $\mathcal{S}_\theta(a)(x_j)$ is the direct
821 output of the GAOT architecture, and the MSE loss is computed between $\mathcal{S}_\theta(a)(x_j)$ and the true
822 steady-state solution $u_{\text{true}}(x_j)$ of PDE (A.2).

823 **Time-Dependent PDEs.** To learn the solution operator for time-dependent PDEs, GAOT is used to
824 update the solution forward in time. Given the solution $u(t)$ at time t and coefficients c (forming the
825 augmented input $a(t) = (c, u(t))$), the model predicts the solution at $t + \tau$. The GAOT architecture
826 produces an output $\hat{\mathcal{S}}_\theta(x, t, \tau, a(t))$. The final prediction for $u(t + \tau)$, denoted $\mathcal{S}_\theta(t, \tau, a(t))$, is
827 constructed using a general time-stepping strategy as per Eq. (7) from the main text, see also [39]:

$$\mathcal{S}_\theta(t, \tau, a(t)) = \gamma u(t) + \delta \hat{\mathcal{S}}_\theta(x, t, \tau, a(t)) \quad (\text{B.17})$$

828 The MSE loss is then computed between this $\mathcal{S}_\theta(t, \tau, a(t))$ and the true solution $u_{\text{true}}(t + \tau)$. The
829 choice of parameters (γ, δ) determines the time-stepping strategy and what the network output $\hat{\mathcal{S}}_\theta$
830 effectively learns:

- 831 • **Output Stepping** ($\gamma = 0, \delta = 1$): The final prediction is $\mathcal{S}_\theta(t, \tau, a(t)) = \hat{\mathcal{S}}_\theta(x, t, \tau, a(t))$.
832 The network output $\hat{\mathcal{S}}_\theta$ directly learns to approximate $u(t + \tau)$.
- 833 • **Residual Stepping** ($\gamma = 1, \delta = 1$): The final prediction is $\mathcal{S}_\theta(t, \tau, a(t)) = u(t) +$
834 $\hat{\mathcal{S}}_\theta(x, t, \tau, a(t))$. The network output $\hat{\mathcal{S}}_\theta$ learns to approximate the residual, $u(t + \tau) - u(t)$.
- 835 • **Time-Derivative Stepping** ($\gamma = 1, \delta = \tau$): The final prediction is $\mathcal{S}_\theta(t, \tau, a(t)) = u(t) +$
836 $\tau \cdot \hat{\mathcal{S}}_\theta(x, t, \tau, a(t))$. The network output $\hat{\mathcal{S}}_\theta$ learns to approximate the time-derivative,
837 $(u(t + \tau) - u(t))/\tau$.

838 GAOT offers the flexibility to use any of these strategies. A detailed ablation of their comparative
839 performance is described in SM Sec. F.

840 B.5.2 Data Normalization

841 Data normalization is applied to stabilize training. We typically use Z-score normalization, where for
842 a quantity X , its normalized version \hat{X} is $(X - \mu_X)/\sigma_X$. The mean μ_X and standard deviation σ_X
843 are computed over the training dataset.

844 **Time-Independent PDEs.** For input features $a(x_j)$ and output solution fields $u(x_j)$, normalization
845 parameters are computed across all samples and spatial points in the training set for each channel
846 independently. The model is trained on normalized inputs to predict normalized outputs.

847 **Time-Dependent PDEs.** The input $u(t)$ is normalized using its global mean and standard deviation
848 computed over all time steps and samples in the training set. The normalization of the target for the
849 network output $\hat{\mathcal{S}}_\theta(x, t, \tau, a(t))$ depends on the chosen time-stepping strategy, as $\hat{\mathcal{S}}_\theta$ learns a different
850 physical quantity in each case:

- 851 • **Output Stepping:** The network $\hat{\mathcal{S}}_\theta$ aims to predict $u(t + \tau)$. Thus, the ground truth values
852 $u(t + \tau)$ are normalized, and $\hat{\mathcal{S}}_\theta$ is trained to predict these normalized values. Statistics μ_u
853 and σ_u are computed from all values $u(t')$ in the training set. The normalized target for $\hat{\mathcal{S}}_\theta$ is
854 $\hat{u}(t + \tau) = (u(t + \tau) - \mu_u)/\sigma_u$.
- 855 • **Residual Stepping:** The network $\hat{\mathcal{S}}_\theta$ aims to predict the residual $R(t, \tau) = u(t + \tau) - u(t)$. Thus,
856 these true residual values are computed from the training data, and their statistics (μ_R, σ_R) are
857 used for normalization. The normalized target for $\hat{\mathcal{S}}_\theta$ is $\hat{R}(t, \tau) = (R(t, \tau) - \mu_R)/\sigma_R$.
- 858 • **Time-Derivative Stepping:** The network $\hat{\mathcal{S}}_\theta$ aims to predict the time-derivative $D(t, \tau) = (u(t +$
859 $\tau) - u(t))/\tau$. These true derivative values are computed, and their statistics (μ_D, σ_D) are used for
860 normalization. The normalized target for $\hat{\mathcal{S}}_\theta$ is $\hat{D}(t, \tau) = (D(t, \tau) - \mu_D)/\sigma_D$.

861 Time t and lead-time τ inputs are also typically scaled or normalized. Further details on these
862 normalizations can be found in [39].

B.5.3 General Training Setup

This section provides an overview of our training hyperparameters. Unless otherwise noted, all experiments follow these settings. Table B.1 summarizes the primary hyperparameters and training schedules. In particular, we distinguish between time-dependent and time-independent PDE tasks in terms of epoch count, and highlight the differences in hardware usage for the DrivAerNet++ dataset. All models except DrivAerNet++ run on a single GeForce RTX 4090 GPU. For the DrivAerNet++ dataset, we use 4 GeForce A100 (40GB) GPUs in data parallel mode, and each GPU holds a batch size of 1. For the scheduler, we warm up to mitigate instability at early epochs, then adopt a cosine schedule for gradual decay, and finalize with a step-based drop for fine-tuning the last epoch range.

Table B.1: Key training hyperparameters and schedulers used for all models, unless otherwise specified.

Hardware	<ul style="list-style-type: none"> • Single-GPU: All models (except DrivAerNet++) are trained on a single GeForce RTX 4090 with batch size = 64. • Four-GPU: For the DrivAerNet++ dataset, we use four GeForce A100 (40GB) GPUs, each with batch size = 1.
Optimizer	<ul style="list-style-type: none"> • Algorithm: AdamW • Weight Decay: 1×10^{-5}
Epochs	<ul style="list-style-type: none"> • Time-Dependent PDEs: 500 epochs • Time-Independent PDEs: 1000 epochs except the DrivAerNet++ dataset, which is trained on 200 epochs.
Learning Rate Scheduler	<ul style="list-style-type: none"> • Warmup (first 10% epochs): LR increases linearly from 8×10^{-4} to 1×10^{-3}. • Cosine Decay (next 85% epochs): LR decays from 1×10^{-3} to 1×10^{-4}. • StepLR (final 5% epochs): LR drops from 1×10^{-4} to 5×10^{-5}.

B.5.4 GAOT Model Configuration

Table B.2 outlines the default configuration of our GAOT framework. This includes the MAGNO used in both the encoder and decoder stages, as well as the Transformer-based global processor. MAGNO converts node features into geometry-aware tokens (encoder) and reconstructs continuous fields (decoder). By default, the coordinates will be rescaled in the domain $[-1, 1]^d$, and we use a single aggregation radius 0.033 for adequate coverage. If multiscale is enabled, we adopt radii $\{0.022, 0.033, 0.044\}$. The default geometric embedding method is local *Statistical Embedding* (e.g. as SM Sec. B.3), and will typically be implemented for unstructured datasets. The Transformer processes geometry-aware tokens globally via multi-head self-attention. We set the hidden dimension to 256 with a 1024-dim feed-forward layer, residual connections, RMSNorm, and RoPE for positional embeddings. By adjusting the patch size and the number of tokens, we can trade off computational cost and model resolution.

B.6 Inference

When predicting solutions for *time-independent* PDEs, we simply feed the input parameters a (e.g. boundary conditions, coefficients, or geometric shape) into our learned operator $\mathcal{S}_\theta(a)$ and obtain the steady-state output $u(x)$ directly. However, for *time-dependent* PDEs, there are two different strategies for forecasting the solution at a future time, using the learned one-step advancement operator $\mathcal{S}_\theta(t, \tau, a(t))$ which, as defined in Eq. (B.17), takes the current time t , a lead-time τ , and the augmented input $a(t) = (c, u(t))$ to predict the solution at $t + \tau$. The two main inference strategies are *direct inference* and *autoregressive inference*.

Direct Inference (DR) Recall from the main text that our learned operator \mathcal{S}_θ takes the lead-time τ as an explicit input, allowing for predictions over variable time steps. Given a snapshot of the solution $u(t_n)$ (which is part of $a(t_n)$), the network can directly predict the solution at any later time $t_n + \tau_{target}$, up to a maximum trained horizon t_{max} , by evaluating $\mathcal{S}_\theta(t_n, \tau_{target}, a(t_n))$. Hence, for each possible time increment $\tau_{target} = k \cdot \Delta t$ (where Δt is a base time step in the dataset, and

Table B.2: Default architectural hyperparameters for GAOT.

Abbreviation	Default Value	Description
MAGNO (Encoder / Decoder)		
PJC	256	Dimensionality for MAGNO’s internal hidden layers.
ENC-MLP	[64, 64, 64]	Hidden layers of the encoder MLP in MAGNO.
DEC-MLP	[64, 64]	Hidden layers of the decoder MLP in MAGNO.
LC	32	Output/Lifting channels after MAGNO (both encoder and decoder).
TS	I	Tokenization Strategy I.
NT	[64, 64]	Number of tokens for Strategy I (e.g., a 64×64 stencil grid).
GR	0.033	Aggregation radius (single-scale) for every token. If multiscale: $\{0.022, 0.033, 0.044\}$.
GeoEmb	statistical	Geometric Embedding for the encoder and decoder.
EM	0.3	Edge masking ratio for the MAGNO, used for 3D drivearnet++ dataset.
Transformer		
PS	2	Default patch size for token grouping if Strategy I or III is used.
Norm	RMSNorm	Normalization used in attention and MLP layers. Pre-norm configuration.
PE	RoPE	Positional embedding used in the Transformer. Rotary positional embeddings.
RES-CON	True	Residual connections between transformer blocks.
TL	5	Number of Transformer blocks.
THS	256	Hidden dimension per self-attention block.
HEAD	8	Number of attention heads.
Dropout	0.2	Dropout ratio in the attention module.
FFN	1024	$4 \times$ hidden size (THS) for the feedforward layer.

897 $1 \leq k \leq k_{\max}$), we can produce the model’s estimate $u(t_n + \tau_{\text{target}})$ from $u(t_n)$ in a single step,
898 without iterating through intermediate time steps. Concretely, if our dataset is discretized at times
899 $\Omega_t^\Delta = \{t_0, t_1, \dots, t_N\}$, we can directly evaluate $\mathcal{S}_\theta(t_n, \tau_{\text{target}}, a(t_n))$ for various τ_{target} values
900 originating from any $t_n \in \Omega_t^\Delta$. This provides a sequence of direct predictions at each possible time
901 offset τ_{target} from any initial time t_n .

902 **Autoregressive Inference (AR)** While direct inference estimates the solution at a single future
903 time, an alternative is to iterate the operator in multiple, typically smaller, sub-steps to reach the
904 final time. This approach is called *autoregressive* (AR) inference. Formally, given an initial snapshot
905 $u(t_0)$, we repeatedly apply the learned operator \mathcal{S}_θ with a chosen fixed time increment for each step,
906 Δt_{AR} , to advance the solution:

$$u(t_{k+1}) = \mathcal{S}_\theta(t_k, \Delta t_{AR}, a(t_k)) \quad (\text{B.18})$$

907 where $t_{k+1} = t_k + \Delta t_{AR}$, and $a(t_k) = (c, u(t_k))$ uses the solution $u(t_k)$ from the previous step (or
908 the initial condition if $k = 0$). This process is repeated until the desired final time t_{final} is reached.

909 We examine two types of autoregressive step sizes in our experiments:

- 910 • **AR-2:** Use an autoregressive time increment of $\Delta t_{AR} = 2$ (assuming time units are
911 consistent with the dataset). Starting from $u(t_0)$, we compute $u(t_0 + 2) = \mathcal{S}_\theta(t_0, 2, a(t_0))$.
912 Then, using $u(t_0 + 2)$, we compute $u(t_0 + 4) = \mathcal{S}_\theta(t_0 + 2, 2, a(t_0 + 2))$, and so on, up to
913 t_{14} . In total, we perform 7 consecutive evaluations of \mathcal{S}_θ .
- 914 • **AR-4:** Use an autoregressive time increment of $\Delta t_{AR} = 4$. In this scenario, we predict
915 $u(t_0 + 4) = \mathcal{S}_\theta(t_0, 4, a(t_0))$, then from $u(t_0 + 4)$, $u(t_0 + 8) = \mathcal{S}_\theta(t_0 + 4, 4, a(t_0 + 4))$,
916 and so on, eventually reaching t_{14} in just 4 iterations (assuming $t_0 = 0$ and $t_{\text{final}} = 16$ for
917 this example, or if t_{14} is the target after some steps).

918 Generally, the choice of the AR step size Δt_{AR} is flexible. One could select any valid $\Delta t_{AR} \leq \tau_{\max}$
 919 (where τ_{\max} is the maximum lead-time the model was reliably trained for in a single step) at each
 920 sub-step. Note that using fewer, larger time steps (e.g., $\Delta t_{AR} = 4$) can reduce computational cost
 921 but potentially compounds prediction errors more quickly if the operator \mathcal{S}_θ is less accurate for
 922 larger single-step lead-times. Conversely, smaller increments (e.g. $\Delta t_{AR} = 2$) tend to accumulate
 923 errors more gradually but require more iterations (and thus more computation) to reach the final time.
 924 Details can be found in [20, 39].

925 C Baselines

926 For the time-dependent benchmarks (including those on unstructured grids detailed in Table 1 and
 927 regular grids in Table E.2, the corresponding baseline results are primarily obtained from the work
 928 by [39]. These baseline models include RIGNO-12, RIGNO-18, CNO, scOT, FNO, GeoFNO,
 929 FNO DSE, and GINO. For further details on these methods, please refer to the paper [39]. In this
 930 work, we have additionally included three more recent models for a comprehensive comparison:
 931 Transolver [50], GNOT [18], and UPT [1]. Brief descriptions of these newly added models and the
 932 specific hyperparameters adopted in our experiments are provided below.

933 C.1 UPT

934 *Universal Physics Transformers* (UPT) [1] form a neural-operator framework that fits into the
 935 canonical encode–process–decode pipeline:

$$\mathcal{U} = \mathcal{D} \circ \mathcal{A} \circ \mathcal{E}, \quad (\text{C.1})$$

936 where \mathcal{E} (Encoder) compresses k input points—coming from an arbitrary Eulerian mesh or Lagrangian
 937 particle cloud—into a fixed set of n_{latent} tokens. It first embeds the features and coordinates through
 938 a radius-graph message-passing layer that aggregates information into n_s supernodes, and finally
 939 employs transformer and perceiver pooling blocks to obtain the latent representation $z_t \in \mathbb{R}^{n_{\text{latent}} \times h}$.

940 \mathcal{A} (Approximator) is a stack of transformer blocks that advances the latent state in time, $\mathcal{A} : z_t \mapsto$
 941 $z_{t+\Delta t}$, enabling fast *latent roll-outs* without repeatedly decoding to the spatial domain.

942 \mathcal{D} (Decoder) is a Perceiver-style cross-attention module that evaluates the latent field at any set of
 943 query positions $\{y_i\}_{i=1}^{k'}$, yielding $u_{t+\Delta t}(y_i) = \mathcal{D}(z_{t+\Delta t}, y_i)$ with $\mathcal{O}(n_{\text{latent}})$ complexity independent
 944 of k' .

945 In the setting of time-independent problems, we bypass the latent roll-out stage, and adopt a
 946 lightweight configuration in our experiments. Specifically, we use latent tokens = 64 and em-
 947 bedding dimensions = 64, which results in a model size of $0.74M$. A large variant with 256 latent
 948 tokens and 192 embedding dimension as setup in [1] was found to suffer from optimization difficulties
 949 and was not adopted in our baseline results. The same optimizer setup as GAOT is used here.

950 Considered Hyperparameters

<i>Architecture</i>	
Trainable parameters	0.74M
Number of supernodes n_s	2048
Radius for message passing	0.033
Embedding (feature) channels	64
Encoder transformer blocks	4
Encoder attention heads	4
Latent tokens n_{latent}	64
Latent dimension h	64
Approximator transformer blocks	4
Approximator attention heads	4
Decoder attention heads	4
<i>Training</i>	
Optimizer	AdamW
Scheduler	same as in B.2
Initial learning rate	$1 \cdot 10^{-3}$
Weight decay	10^{-5}
Number of epochs	500
Batch size	64

C.2 Transolver

Transolver [50] is a transformer-based operator learning model designed for PDEs on unstructured grids. It follows an encode-process-decode paradigm by stacking multiple Transolver blocks. The core of each block is the Physics-Attention mechanism.

Given input features $X_{\text{phys}} \in \mathbb{R}^{N \times C}$ for N mesh points:

1. Encoding to Tokens: First, for each mesh point feature $x_i \in X_{\text{phys}}$, M slice weights $w_i \in \mathbb{R}^{1 \times M}$ are learned, typically via a projection followed by a Softmax function: $w_i = \text{Softmax}(\text{Project}(x_i))$. These weights determine the assignment of mesh points to M learnable "slices". The j -th physics-aware token $z_j \in \mathbb{R}^{1 \times C}$ is then encoded by a weighted aggregation of all mesh point features, using the slice weights:

$$z_j = \frac{\sum_{i=1}^N w_{i,j} x_i}{\sum_{i=1}^N w_{i,j}} \quad (\text{C.2})$$

This results in M tokens $Z = \{z_j\}_{j=1}^M \in \mathbb{R}^{M \times C}$.

2. Token Processing: These M tokens Z are processed by a standard attention mechanism (e.g., multi-head self-attention) to capture correlations between different physical states represented by the tokens:

$$Z'_{\text{proc}} = \text{Attention}(Z) \quad (\text{C.3})$$

The processed tokens are $Z'_{\text{proc}} = \{z'_j\}_{j=1}^M \in \mathbb{R}^{M \times C}$.

3. Decoding to Physical Grid (Deslicing): The updated token features Z'_{proc} are then broadcast back and recomposed onto the N physical mesh points using the original slice weights w :

$$x'_i = \sum_{j=1}^M w_{i,j} z'_j \quad (\text{C.4})$$

This yields the output features for the Physics-Attention block, $X'_{\text{phys}} = \{x'_i\}_{i=1}^N \in \mathbb{R}^{N \times C}$.

A full Transolver layer typically incorporates this Physics-Attention mechanism within a standard Transformer layer structure, including Layer Normalization and Feed-Forward Networks.

While the Physics-Attention mechanism itself is designed to have a computational complexity linear with respect to the number of mesh points, it is important to note that the slicing (Eq. C.2) and deslicing (Eq. C.4) operations, which involve all N points, are performed within each of the L Transolver layers. This repeated mapping can lead to significant computational costs and memory overhead, especially for large N . This contrasts with architectures like GAOT and UPT, which perform the encoding to a latent space and decoding from it only once, with intermediate processing happening entirely in the latent token domain. In our experiments with time-independent partial differential equations, we followed the settings from the original Transolver paper [50];

Considered Hyperparameters

<i>Architecture</i>	
Trainable parameters	3.85 M
Hidden channels	256
Attention heads	8
Number of Layers	8
MLP ratio	2
number of slice	32
<i>Training</i>	
Optimizer	AdamW
Scheduler	same as in B.2
Initial learning rate	$1 \cdot 10^{-3}$
Weight decay	10^{-5}
Number of epochs	500
Batch size	20

C.3 GNOT

General Neural Operator Transformer (GNOT) [18] is a Transformer-based framework designed for operator learning, particularly addressing challenges such as irregular meshes, multiple heterogeneous input functions, and multiscale problems. Its overall architecture can be represented as:

$$\mathcal{G} = \underbrace{\mathcal{F} \circ (\mathcal{B})^L}_{\text{processor}} \circ \mathcal{E}, \quad (\text{C.5})$$

where \mathcal{E} is the encoder, \mathcal{B} represents a GNOT Transformer block (repeated L times), and \mathcal{F} is the output decoder.

1. Encoder (\mathcal{E}): The encoder maps diverse input sources (geometry, fields, parameters, edges) to embeddings using dedicated MLPs. This yields query embeddings $Q \in \mathbb{R}^{N_q \times d}$ for target points and a set of m conditional embeddings $\{Y^{(\ell)} \in \mathbb{R}^{N_\ell \times d}\}_{\ell=1}^m$ from other input functions.
2. GNOT Transformer Block (\mathcal{B}): Each block refines query embeddings Q using conditional embeddings $Y^{(\ell)}$ via:
 - Heterogeneous Normalized linear Cross-Attention (HNA): Fuses Q with each $Y^{(\ell)}$ using separate MLPs for keys/values from different $Y^{(\ell)}$, followed by normalization and averaging.

$$Q'_{\text{cross}} = Q + \frac{1}{L_c} \sum_{\ell=1}^{L_c} \text{NormLinearCrossAttn}(Q, Y^{(\ell)}) \quad (\text{C.6})$$

- Normalized Self-Attention: Applies normalized linear self-attention to Q'_{cross} for further refinement.

$$Q'_{\text{self}} = \text{NormLinearSelfAttn}(Q'_{\text{cross}}) \quad (\text{C.7})$$

- Geometric Gating FFN: A Mixture-of-Experts (MoE) FFN where expert FFNs (E_k) are weighted by $p_k(x_{\text{coord}})$. These weights are predicted by a gating network $G(\cdot)$ using query point coordinates x_{coord} , enabling soft domain decomposition for multiscale problems.

$$\text{FFN}_{\text{Gated}}(X) = \sum_{k=1}^K p_k(x_{\text{coord}}) \cdot E_k(X), \quad p_k(x_{\text{coord}}) = \text{Softmax}(G_k(x_{\text{coord}})) \quad (\text{C.8})$$

- These components, with Layer Normalization and residual connections, form the block.
3. Decoder (\mathcal{F}): After L blocks, a final decoder (typically an MLP) maps processed query features to the output solution.

Considered Hyperparameters

<i>Architecture</i>	
Trainable parameters	4.87 M
Hidden channels	128
Attention heads	8
Number of Layers	8
MLP ratio	2
<i>Training</i>	
Optimizer	AdamW
Scheduler	same as in B.2
Initial learning rate	$1 \cdot 10^{-3}$
Weight decay	10^{-5}
Number of epochs	500
Batch size	20

D Datasets

In this work, we test GAOT on 24 benchmarks for both time-independent and time-dependent PDEs of various types, ranging from regular grids to random point clouds to highly unstructured adapted grids. The time-dependent and Poisson-Gauss dataset are sourced from [20] and [39], respectively. A static elasticity dataset is from [26]. We have generated five additional challenging datasets: a Poisson-C-Sines dataset exhibiting multiscale properties, and four datasets for compressible fluid dynamics with highly unstructured adapted grids. Detailed information regarding these datasets can be found in the Tab [D.1](#).

We focus on the following PDE Types under various initial/boundary conditions and domain geometries:

Hyper-Elastic Equation (HEE) :

$$\rho^s \frac{\partial^2 \mathbf{u}}{\partial t^2} + \nabla \cdot \boldsymbol{\sigma} = 0, \quad (\text{D.1})$$

where ρ^s is the mass density, \mathbf{u} is the displacement vector, and $\boldsymbol{\sigma}$ is the stress tensor. A constitutive model links the strain tensor ϵ to the stress tensor. The material is the incompressible Rivlin-Saunders type, characterized by $\boldsymbol{\sigma} = \frac{\partial w(\epsilon)}{\partial \epsilon}$ with $w(\epsilon) = C_1(I_1 - 3) + C_2(I_2 - 3)$.

Poisson Equation (PE) :

$$-\Delta u = f, \quad \text{in } (0, 1)^2, \quad (\text{D.2})$$

with homogeneous Dirichlet boundary conditions. The dataset related to poisson equation use either sinusoidal or Gaussian-like source terms on square or circular domains (see Table [D.1](#)).

Table D.1: Overview of the datasets used in this work. Datasets listed above line are time-independent, while those below are time-dependent. Geometry variation (GeoVar) describes whether all data samples share the same geometry. Characteristic briefly describes each dataset’s geometry or PDE setup. The PDE Type column indicates the corresponding class. Visualization (Vis.) provides references to visual examples; for time-dependent datasets, this may include visualizations for both unstructured partially ones and original regular grid ones. Datasets marked with * are newly proposed in this work.

Abbreviation	GeoVar	Characteristic	PDE Type	Vis.
Poisson-C-Sines*	F	Circular domain with sines f	PE	G.1
Poisson-Gauss	F	Gaussian source	PE	G.2
Elasticity	T	Hole boundary distance	HEE	G.3
NACA0012*	T	Flow past NACA0012 airfoil	CE	G.4
NACA2412*	T	Flow past NACA2412 airfoil	CE	G.5
RAE2822*	T	Flow past RAE2822 airfoil	CE	G.6
Bluff-Body*	T	Flow past bluff-bodies	CE	G.7
DrivAerNet++(p)	T	Surface pressure	INS	G.8
DrivAerNet++(wss)	T	Surface wall shear stress	INS	G.9
NS-Gauss	F	Gaussian vorticity IC	INS	G.10 , G.18
NS-PwC	F	Piecewise const. IC	INS	G.11 , G.19
NS-SL	F	Shear layer IC	INS	G.12 , G.20
NS-SVS	F	Sinusoidal vortex sheet IC	INS	G.13 , G.21
CE-Gauss	F	Gaussian vorticity IC	CE	G.14 , G.22
CE-RP	F	4-quadrant RP	CE	G.15 , G.23
Wave-Layer	F	Layered wave medium	WE	G.16 , G.24
Wave-C-Sines	F	Circular domain with sines IC	WE	G.17

1025 **Incompressible Navier–Stokes (INS)** :

$$\begin{aligned}\nabla \cdot \mathbf{v} &= 0, \\ \partial_t \mathbf{v} + (\mathbf{v} \cdot \nabla) \mathbf{v} &= -\nabla p + \nu \nabla^2 \mathbf{v},\end{aligned}$$

1026 where \mathbf{v} is the velocity field, p is the pressure, and viscosity is ν . It assumes periodic boundary
1027 conditions and sample various initial conditions (e.g., Gaussian, piecewise-constant, sinusoidal vortex
1028 sheets).

1029 **Compressible Euler (CE)** :

$$\partial_t \mathbf{u} + \nabla \cdot \mathbf{F} = 0, \quad \mathbf{u} = (\rho, \rho \mathbf{v}, E)^\top, \quad E = \frac{1}{2} \rho \|\mathbf{v}\|^2 + \frac{p}{\gamma-1}, \quad (\text{D.3})$$

1030 with $\gamma = 1.4$. Showing in [20], it imposes periodic boundary conditions and ignore gravity effects.
1031 Data are generated using random initial/boundary conditions such as Gaussian or Riemann problem
1032 (RP) setups.

1033 **Wave Equation (WE)** :

$$\partial_{tt} u - c^2(x, y) \nabla^2 u = 0, \quad (\text{D.4})$$

1034 with a spatially varying propagation speed $c(x, y)$ in an inhomogeneous medium. The dataset employs
1035 absorbing or homogeneous Dirichlet boundaries. Initial conditions (e.g., sinusoidal or layered) are
1036 drawn from parameterized distributions.

1037 All time-dependent problems are numerically integrated up to $T = 1$ (except for the Wave-
1038 C-Sines where $T=0.005$), collected (up to) $N_t = 21$ uniform snapshots per sample at $t \in$
1039 $\{0, 2, 4, 6, 8, 10, 12, 14\}$. For time-dependent PDE, as mentioned before, we use the same all2all
1040 training strategy proposed in Poseidon [20]. This means that each trajectory can generate 28 pairs for
1041 training.

1042 D.1 Poisson-C-Sines

1043 This dataset contains solutions to the two-dimensional Poisson equation with a circular domain.
 1044 The Poisson equation is a fundamental linear elliptic partial differential equation (PDE) given by
 1045 Eq. D.2. The dataset represents the mapping from the source term f to the solution u using the
 1046 solution operator $\mathcal{G}^\dagger : f \mapsto u$. The source term is defined as:

$$f(x, y) = \frac{\pi}{K^2} \sum_{i,j=1}^K a_{ij} \cdot (i^2 + j^2)^{-r} \sin(\pi i x) \sin(\pi j y), \quad \forall (x, y) \in D, \quad (\text{D.5})$$

1047 where $r = -0.5$ and $K = 16$. The coefficients a_{ij} are sampled i.i.d. uniformly from $[-1, 1]$ to
 1048 generate the dataset. The solution u is computed on a circular domain with zero Dirichlet boundary
 1049 conditions. The dataset is generated using a finite element method (FEM) on a triangular mesh in a
 1050 circular domain. The mesh is generated using the Delaunay algorithm with 16431 points and 32441
 1051 elements.

1052 D.2 Compressible Flow Past Airfoils & Bluff Bodies

1053 A classic benchmark for compressible flow physics used for testing the accuracy of neural operators
 1054 and PDE foundation models is the case of flow past airfoils [20, 26]. The datasets used in these
 1055 papers are limited to transonic flow past perturbations of a single airfoil. To capture a broader range
 1056 of rich flow phenomena, it is essential to explore the parameter space spanned by the Mach number
 1057 Ma , angle of attack α and the shape function. To address this issue, this new dataset introduces
 1058 samples comprising a range of flow phenomena from subsonic to supersonic flow for varying angles
 1059 of attack across classical airfoils and various bluff body geometries. The steady-state compressible
 1060 Euler equations govern the flow phenomena in this dataset. The equations have been solved using the
 1061 finite-volume EULER solver of the open-source software SU2 [11] on an unstructured grid generated
 1062 by Delaundo [40]. Convective flux discretization is done using the Jameson-Schmidt-Turkel (JST)
 1063 scheme that is designed especially for achieving quick convergence to steady-state solutions of the
 1064 compressible Euler equations. Figure D.1 represents an O-type unstructured mesh generated using
 1065 Delaundo for the RAE2822 airfoil. Similar O-type unstructured meshes have been generated for all
 1066 airfoils and bluff-bodies considered. The free-stream pressure and temperature conditions for all
 1067 simulations in this dataset are $p_\infty = 1$ atm and $T_\infty = 288.15$ K.

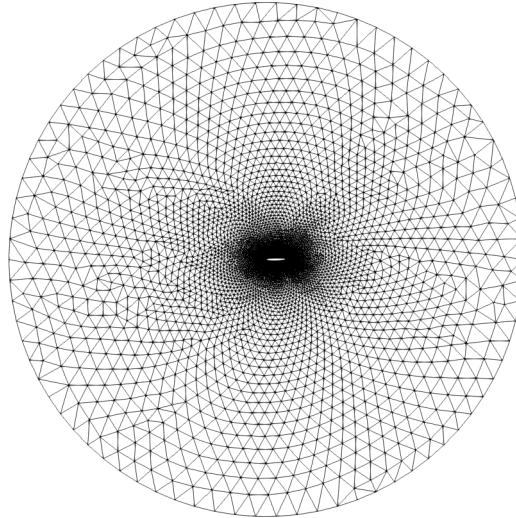


Figure D.1: O-type unstructured mesh - RAE2822 airfoil

1068 D.2.1 Airfoils

1069 Flow past airfoils is considered for $0.5 \leq Ma \leq 1.4$, $0.5^\circ \leq \alpha \leq 5.0^\circ$ and for 500 unique
 1070 perturbations applied to shape functions of the NACA2412, NACA0012, and RAE2822 airfoils.

1071 Anisotropic adaptive mesh refinement for highly accurate shock resolution (oblique and bow shocks)
 1072 is performed using INRIA's pyAMG library coupled with SU2 [32]. The anisotropic mesh refinement
 1073 is done using a Mach sensor that generates refined meshes based on the simulation on a coarse grid
 1074 such as in Figure D.1. The final simulations are then performed by the SU2 EULER solver on the
 1075 new refined mesh. Figure D.2 represents the highly unstructured adapted grids for transonic and
 1076 supersonic flow past the RAE2822 airfoil.

1077 We consider the reference airfoil shapes with the upper and lower surface coordinates located at
 1078 $(x, y_{\text{ref}}^U(\xi))$ and $(x, y_{\text{ref}}^L(\xi))$ where $\xi = \frac{x}{c}$, c is the chord length. We use the Class Function/Shape
 1079 Function Transformation (CST) Method [24] for parameterizing the airfoil surfaces in terms of a
 1080 class function $C(\xi)$ and shape functions $S^U(\xi)$, $S^L(\xi)$ using an in-house MATLAB code. The airfoil
 1081 upper surface function $\eta^U(\xi)$ and lower surface function $\eta^L(\xi)$ are parametrized as follows:

$$\eta^U(\xi) = C(\xi)S^U(\xi), \quad \eta^L(\xi) = C(\xi)S^L(\xi) \quad (\text{D.6})$$

1082 where the class function for airfoils is given as:

$$C(\xi) = \sqrt{\xi(1-\xi)} \quad (\text{D.7})$$

1083 and the upper and lower surface shape functions are respectively

$$S^U(\xi) = \sum_{i=0}^n A_i \frac{n!}{i!(n-i)!} \xi^i (1-\xi)^{n-i}, \quad S^L(\xi) = \sum_{i=0}^n B_i \frac{n!}{i!(n-i)!} \xi^i (1-\xi)^{n-i} \quad (\text{D.8})$$

1084 The polynomials $S_{i,n} = \frac{n!}{i!(n-i)!} \xi^i (1-\xi)^{n-i}$ associated with the coefficients (A_i, B_i) are Bernstein
 1085 polynomials and $n = 7$ is chosen. The parameters (A_i, B_i) directly influence key airfoil design
 1086 variables such as the leading edge radius, trailing edge boattail angle, maximum airfoil thickness and
 1087 maximum thickness location. The parameters (A_0, B_0) are linked to the leading edge radius R_{LE} as
 1088 follows,

$$A_0 = -B_0 = \sqrt{2r}, \quad r = \frac{R_{\text{LE}}}{c} \quad (\text{D.9})$$

1089 and the parameters (A_n, B_n) are linked to the upper boattail angle β_U and lower boattail angle β_L :

$$A_n = \tan(\beta_U), \quad B_n = \tan(\beta_L) \quad (\text{D.10})$$

1090 To generate perturbed variations of the airfoils, minor random perturbations are made to the CST
 1091 parameters (A_i, B_i) keeping in mind the constraints $A_0 = -B_0$, $A_i > B_i$ and $\beta_U > \beta_L$. We
 1092 have randomly sampled 5384 solutions from our dataset for each classical airfoil shape with a
 1093 train/validation/test split of 5000/128/256. For each data, we sub-samples 8000 points for training,
 1094 validation and testing.

1095 D.2.2 Bluff-Body

1096 Flow past bluff-bodies is considered at $0.3 \leq Ma \leq 1.3$, $0.5^\circ \leq \alpha \leq 15.0^\circ$ for a wide variety of
 1097 simple bluff-body geometries. Steady-state solutions for the compressible Euler equation for flow
 1098 past bluff-bodies may not exist or are often unstable making it difficult to attain convergence. This
 1099 bluff-body aerodynamics dataset comprises of samples that are at pseudo-steady state in a large
 1100 finite-time limit. Figure E.6a describes all the bluff body geometries taken into consideration in this
 1101 dataset.

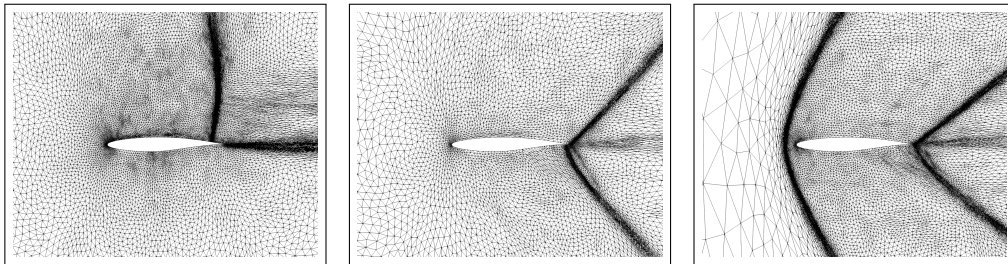


Figure D.2: Adaptively refined meshes for flow past the RAE2822 airfoil at $\alpha = 2.0$ and at different $Ma = 0.8$ (left), 1.0 (center), 1.4 (right).

1102 We sample 4384 solutions from our dataset with a train/validation/test split of 4000/128/256 for all
 1103 bluff-body geometries used for "Training and Testing". For each data, we sub-samples 14000 points
 1104 for training, validation and testing.

1105 E Additional Results

1106 E.1 Accuracy, Robustness and Computational Efficiency Metrics

1107 **Accuracy** For benchmarks in Table 1 and Table E.3, we adopt the relative L^1 error metric, following
 1108 the manner of CNO [45], to measure the discrepancy between the ground-truth operator output $\mathcal{S}(a)$
 1109 and the model's prediction $\mathcal{S}_\theta(a)$ over a discrete set of points. Suppose a given sample is discretized
 1110 into N points (either on a regular grid or an unstructured mesh). For a single-component solution
 1111 field, the discretized relative L^1 error ε is defined as

$$\varepsilon = \frac{1}{N} \sum_{i=1}^N \frac{|(\mathcal{S}(a))_i - (\mathcal{S}_\theta(a))_i|}{|(\mathcal{S}(a))_i|}. \quad (\text{E.1})$$

1112 Because the test set contains multiple input–output pairs $\{(a, \mathcal{S}(a))\}$, we obtain a distribution of
 1113 errors. We report the median of these errors—rather than the mean—to mitigate the influence of
 1114 strong outliers. For multi-component PDE solutions (e.g., velocity and pressure fields), we compute
 1115 the median error per component, then average these medians to obtain a single scalar metric. In
 1116 time-dependent tasks, we specifically report the relative L^1 error at the final time snapshot, as errors
 1117 usually accumulate over time and thus the last snapshot often poses the greatest challenge.

1118 For the pressure and wall shear stress (WSS) in the DrivAerNet++ dataset, we evaluated the model
 1119 on 1154 samples according to the official leaderboard. The errors are calculated based on normalized
 1120 pressure and WSS. For pressure, the mean and standard deviation (std) for normalization were
 1121 obtained from the open-sourced code of [12]. However, for WSS, as the normalization statistics
 1122 were not open-sourced, we calculated the mean and variance for the x, y, and z components over
 1123 8000 samples to be used for normalization. The Mean Squared Error (MSE) and Mean Absolute
 1124 Error (MAE) are first computed for each individual sample. Then, the average of these errors across
 1125 the 1154 test samples is reported as the final result. This entire procedure strictly follows their
 1126 open-sourced code methodology of [12].

1127 In Table E.1, we further provide an aggregate performance comparison of GAOT and three represen-
 1128 tative baseline models (Transolver, GINO, RIGNO-18) on both time-dependent and time-independent
 1129 dataset categories, described in Table 1. Specifically, for each individual dataset, we calculate the
 1130 normalized scores for every model. The best-performing model is assigned a score of 1. The scores
 1131 for other models are calculated as the ratio of the best model's error to their respective errors:

$$S_{\text{norm}} = \frac{\text{error}_{\text{best}}}{\text{error}_{\text{model}}} \quad (\text{E.2})$$

1132 These dataset scores are then summed for each model to derive total scores for the time-dependent and
 1133 time-independent dataset categories, respectively, offering a complete view of model performance.

1134 **Robustness** To evaluate the consistency of model performance across different datasets, we intro-
 1135 duce a Robustness Score. This score is calculated for both the time-dependent and time-independent
 1136 categories of datasets. Leveraging the normalized scores obtained by each model on the individual
 1137 datasets within these categories, the Robustness Score for a model is defined as:

$$\text{Robustness Score} = \bar{S}_{\text{norm}} \times (1 - \text{CV}), \quad (\text{E.3})$$

1138 where \bar{S}_{norm} is the mean of the model's normalized scores across all datasets in a specific category
 1139 (either time-dependent or time-independent). The term CV represents the Coefficient of Variation of
 1140 these normalized scores, calculated as:

$$\text{CV} = \frac{\sigma_{S_{\text{norm}}}}{\bar{S}_{\text{norm}}}, \quad (\text{E.4})$$

1141 where $\sigma_{S_{\text{norm}}}$ is the standard deviation of the model's normalized scores within that same category. A
 1142 higher Robustness Score suggests that a model not only achieves high average performance (high
 1143 mean normalized score) but also exhibits less variability in its performance across the different
 1144 datasets within the category (low CV), indicating greater reliability. The robustness scores for GAOT,
 1145 Transolver, GINO and RIGNO-18 are shown in Table E.1.

Computational Efficiency To provide a comprehensive characterization of model performance and analyze the inherent accuracy-efficiency trade-off, we further evaluate the computational efficiency of the models during both training and inference phases.

Training efficiency is quantified by the *training throughput*, defined as the number of samples the model can process per second during training, encompassing the forward pass, backward pass, and gradient update. A high training throughput is indicative of a model’s ability to learn quickly from data. This is essential for handling large-scale datasets or developing large foundation models where training time can be a significant bottleneck. For measuring throughput, the batch size for each model was determined first by identifying the maximum value that could be run without encountering Out-of-Memory (OOM) errors on the target hardware. The actual batch size used for the throughput measurement was then set to approximately half of this maximum. This heuristic is based on the observation that peak throughput is often not achieved at the absolute maximum batch size, but rather at a point (frequently around half the maximum) where GPU resources, such as shared memory bandwidth, are optimally utilized, leading to the highest processing rates.

Inference efficiency is measured by the *inference latency*, which is the time taken for the model to perform a single forward pass on an individual sample (i.e., batch size of 1). Low inference latency is a critical attribute for the practical deployment of models, particularly in applications requiring real-time or near real-time predictions, such as in engineering simulations, interactive design tools, or control systems.

All computational efficiency metrics were benchmarked on the Bluff-Body dataset with one NVIDIA-4090 hardware. To ensure reliable and stable measurements, the GPU was warmed up prior to data collection, and each reported metric is the average of 100 repeated measurements.

E.2 Results for Radar Chart in Main Text.

Table E.1 presents the raw data used to generate the radar chart in Figure 1 of the main text. The metrics depicted in the radar chart include:

- **Accuracy (Acc. and Acc.(t)):** Overall accuracy on time-independent (Acc.) and time-dependent (Acc.(t)) datasets.
- **Robustness (Robust. and Robust.(t)):** Robustness on time-independent (Robust.) and time-dependent (Robust.(t)) datasets.
- **Training Throughput (Tput.(train)):** The number of samples processed per second during training.
- **Inference Latency (Infer. Latency):** The time (ms) taken for a single forward pass on one sample during inference.

The precise definitions and calculation methodologies for these metrics are detailed in Sec. E.1

Model	acc.(t)	acc.	Tput(train)	Infer Latency	Peak memory	InputScal.	ModelScal	robust(t)	robust
GAOT	7.45	6.30	97.5	6.966	101.7	68.12	48.7	0.80	0.77
Transolver	0	4.12	39.5	15.295	144.0	8.96	6.69	0	0.22
GINO	2.77	2.94	60.4	8.455	556.8	30.53	40.00	0.15	0.19
RIGNO-18	7.37	4.38	50.3	12.749	188.8	12.52	7.51	0.85	0.29

Table E.1: Data for Radar Chart

Table E.1 also includes **Peak Memory (MB)**, which records the peak GPU memory consumption of each model during inference with a batch size of 1. Although not visualized in the radar chart (Figure 1), the data indicates that GAOT exhibits the lowest peak memory usage among the compared models. Furthermore, Figure E.1 (a, c) illustrates the scaling of peak memory with increasing input grid size and model size, respectively. These plots demonstrate GAOT’s superior memory utilization capabilities.

The **Input Scalability** and **Model Scalability** scores presented in the radar chart are derived from the training throughput measured under specific conditions:

- Input Scalability is based on throughput at an input grid size of 50,000 points.
- Model Scalability is based on throughput for a model size of approximately 70 million parameters.

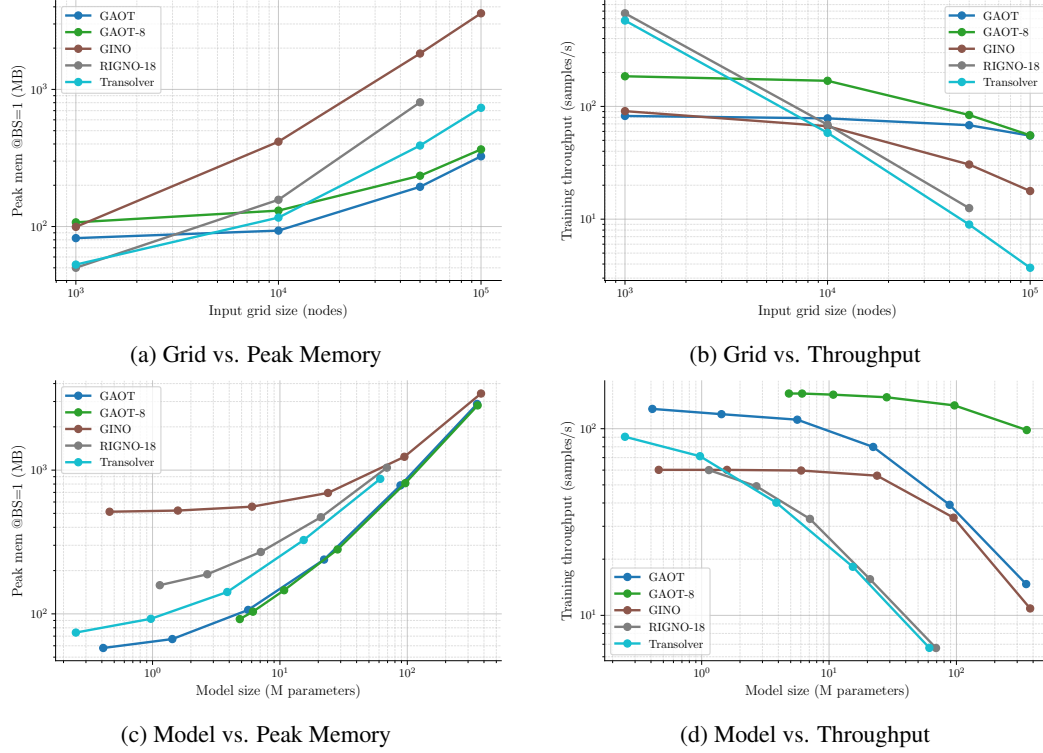


Figure E.1: Performance scaling comparisons across different metrics.

1191 These particular evaluation points were chosen due to the performance limitations encountered with
 1192 models like RIGNO-18 and Transolver on a single NVIDIA 4090 GPU, which prevented us from
 1193 benchmarking them at larger scales. It is important to note that GAOT’s architecture allows it to scale
 1194 significantly beyond these tested limits.

1195 SM Figure E.1 provides detailed scaling curves for both peak memory and training throughput as
 1196 functions of input grid size and model size. To vary the model size for these comparisons, we
 1197 systematically adjusted key architectural width parameters for each model:

- 1198 • For Transolver, we scaled its hidden channel dimension through [64, 128, 256, 512, 1024].
- 1199 • For RIGNO, the hidden channel dimensions of its node and edge functions were varied
 1200 across [64, 128, 256, 512, 1024].
- 1201 • For GINO, the hidden channel dimension of its FNO processor layers was selected from
 1202 [16, 32, 64, 128, 256, 512].
- 1203 • For our GAOT model, we scaled the hidden channel dimension of its attention layers using
 1204 values from [64, 128, 256, 512, 1024, 2048], while the hidden dimension of its FFN layers
 1205 was maintained at four times the attention layer’s hidden dimension.

1206 This figure also introduces results for GAOT-8, a variant of GAOT where the patch size in the
 1207 transformer processor is set to 8 (the default GAOT employs a patch size of 2). As shown, GAOT-8
 1208 can achieve enhanced computational performance. Furthermore, as detailed in our ablation studies
 1209 (Section F.2), this improvement in efficiency with GAOT-8 does not give rise to the substantial
 1210 accuracy degradation.

1211 E.3 Regular Grid Dataset

1212 In addition to datasets with arbitrary point cloud geometries, we also evaluated the performance of our
 1213 GAOT model on time-dependent PDE datasets where the inputs are provided on regular (structured)

1214 grids. The results for GAOT are compared against several baselines, including RIGNO (RIGNO-18
1215 and RIGNO-12), CNO, scOT, and FNO. The performance data for these baseline models are sourced
1216 from the original RIGNO paper [39].

1217 As demonstrated in Table E.2, GAOT also performs well on these structured grid datasets. Our
1218 model consistently ranks within the top two across six of the seven benchmark datasets, achieving
1219 the leading (first place) performance on five of them. This highlights GAOT’s robustness and strong
1220 generalization capabilities across different input discretizations.

Table E.2: Benchmarks with time-dependent datasets with regular grid inputs. Best and 2nd best models are shown in blue and orange fonts for each dataset.

Dataset	Median relative L^1 error [%]					
Structured	GAOT	RIGNO-18	RIGNO-12	CNO	scOT	FNO
NS-Gauss	2.29	2.74	3.78	10.9	2.92	14.41
NS-PwC	1.23	1.12	1.82	5.03	7.12	12.55
NS-SL	0.98	1.13	1.82	2.12	2.49	2.08
NS-SVS	0.46	0.56	0.75	0.70	1.01	7.52
CE-Gauss	5.28	5.47	7.56	22.0	9.44	28.69
CE-RP	4.98	3.49	4.43	18.4	9.74	38.48
Wave-Layer	5.40	6.75	8.97	8.28	13.44	28.13

1221 E.4 Model and Dataset Scaling

1222 **Model Size** To further investigate the scalability of our approach, we conduct an ablation study
1223 on how different model sizes affect performance. We focus on the two compressible Euler datasets,
1224 CE-Gauss and CE-RP, each with 1,024 training trajectories. We measure the final-time relative L^1
1225 error ($t = t_{14}$) and record the total number of parameters and per-epoch training time under various
1226 hyperparameter configurations.

1227 We vary the following components of our GAOT architecture as explained in the Tab B.2:

- 1228 • LC (Lifting Channels): The number of channels used during the encoder stage to project
1229 from the unstructured node features to latent tokens. Intuitively, a larger LC can preserve
1230 more local features when mapping from the input domain to the latent space.
- 1231 • TL (Transformer Layers): The depth of the transformer-based processor. Increasing TL
1232 typically increases modeling capacity for global interactions.
- 1233 • THS (Transformer Hidden Size): The hidden dimension of each self-attention block. A
1234 larger THS can capture richer representations.
- 1235 • FFN (Feed-Forward Network Size): The hidden dimension inside the FFN sub-layer, which
1236 we set to $4 \times$ THS following standard vision transformer practice.

1237 Table E.3 summarizes the performance across a range of these hyperparameters. We also record the
1238 total number of trainable parameters (in millions) and the approximate epoch time (in seconds) on
1239 one NVIDIA 4090 GPU with a batch size of 64. Here, all experiments are done with patch size equal
1240 to 2.

1241 From the top block of Table E.3 (rows 1–4), we observe that as we increase THS from 32 to 256
1242 (keeping TL=5 and LC=32), the final-time errors on both CE-Gauss and CE-RP decrease significantly.
1243 For example, on CE-Gauss, the error drops from 48.4% down to 6.88%. This trend reflects the
1244 transformer’s ability to scale with hidden dimension. The training time per epoch grows from roughly
1245 84 seconds to 143 seconds. While performance improves, larger THS demands more computational
1246 resources.

1247 Next, we fix (TL,THS)=(5,256) and vary LC in the middle block (rows 5–7). Setting LC=32
1248 consistently achieves strong results. Lowering LC to 16 slightly degrades performance, while
1249 pushing LC to 64 or 128 yields only marginal gains. Hence, LC=32 appears sufficient to capture the
1250 encoder-level geometry information.

1251 Finally, the bottom block (rows 8–10) examines the effect of transformer layers TL from 1 up to 10.
1252 With TL=1, errors remain quite high (25.0% on CE-Gauss); adding layers substantially reduces error

Table E.3: Relative L^1 test errors at $t = t_{14}$ with different architectural hyperparameters. Time refers to training time with batch size equals to 64 on 1 NVIDIA-4090 GPU, and the patch size is set to 2. The size of training trajectories is 1024.

Model size		Hyperparameters				Median relative L^1 error [%]	
Parameters [M]	Time [s]	LC	TL	THS	FFN	CE-Gauss	CE-RP
0.14	84	32	5	32	128	48.4	26.5
0.41	89	32	5	64	256	13.2	12.0
1.42	100	32	5	128	512	9.17	7.90
5.6	143	32	5	256	1024	6.88	5.28
5.5	142	16	5	256	1024	7.97	5.94
5.6	154	64	5	256	1024	6.94	5.18
6.1	181	128	5	256	1024	7.33	5.20
1.16	50	32	1	256	1024	25.0	14.5
3.39	98	32	3	256	1024	9.00	6.80
11.2	260	32	10	256	1024	5.28	5.35

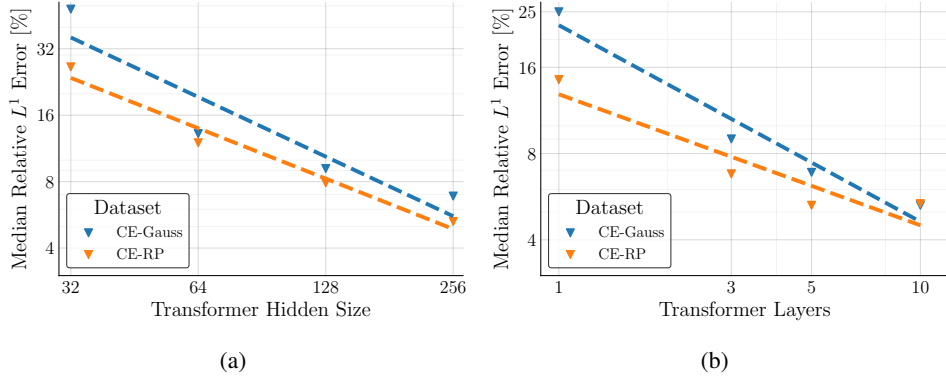


Figure E.2: Relative median L^1 test errors at $t = t_{14}$ with different strategies for scaling model sizes. The x-axis in the left plot corresponds to all the following hyperparameters: THS and TL.

1253 to 9.0% at $TL = 3$, and ultimately down to 5.28% at $TL=10$ on CE-Gauss. Increasing TL to 10 also
1254 expands the parameter count to 11.2M, nearly doubling the training time per epoch (260s).

1255 Figure E.2 illustrates how errors decrease as we scale THS or TL, while Figure E.3 shows the effect
1256 of changing LC or the total parameter count. The largest model tested reaches 11.2M parameters and
1257 attains around 5% error on CE-Gauss, demonstrating the potential to improve accuracy by investing
1258 in more computational resources.

1259 **Data Size** So far, we have discussed how increasing model size affects accuracy. In this subsection,
1260 we turn our attention to data scaling: we examine how the learned operator’s performance changes as
1261 the number of training samples (trajectories or static solutions) grows. Figure E.4 illustrates two sets
1262 of experiments:

1263 **(a) Time-Dependent (Fluid) Datasets.** We plot the final-time ($t = t_{14}$) error on multiple fluid PDE
1264 benchmarks as a function of the training set size $\{128, 256, 512, 1024\}$. All of these datasets use
1265 partial-grid subsampling. The results confirm that as we increase the number of training trajectories,
1266 errors consistently drop across all fluid datasets, often in a near-linear fashion with respect to the
1267 number of training trajectories. This trend highlights the model’s capacity to benefit from additional
1268 time-series diversity.

1269 **(b) Time-Independent (Static) Datasets.** We similarly measure how the final solution error decreases
1270 when expanding the dataset size to $\{128, 256, 512, 1024, 2048\}$ for three static PDE tasks: Poisson-
1271 Gauss, Poisson-C-Sines, and Elasticity. Note that elasticity is limited to at most 1024 samples due to

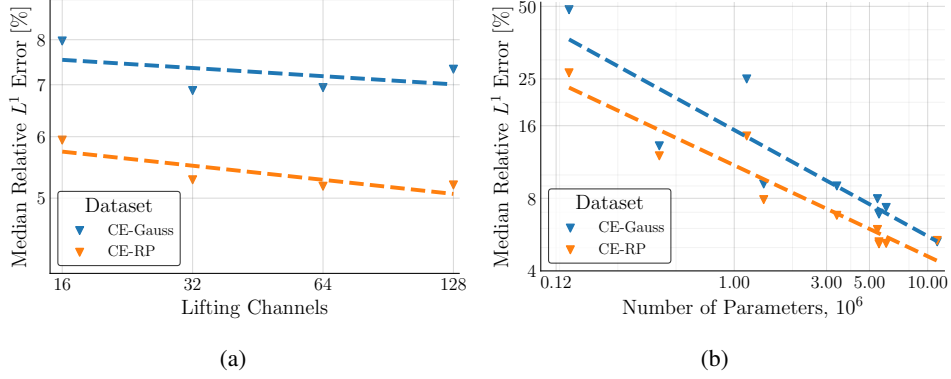


Figure E.3: Relative L^1 test errors at $t = t_{14}$ with different strategies for scaling model sizes. The x-axis in the left plot corresponds to all the following hyperparameters: LC, and the total number of trainable parameters.

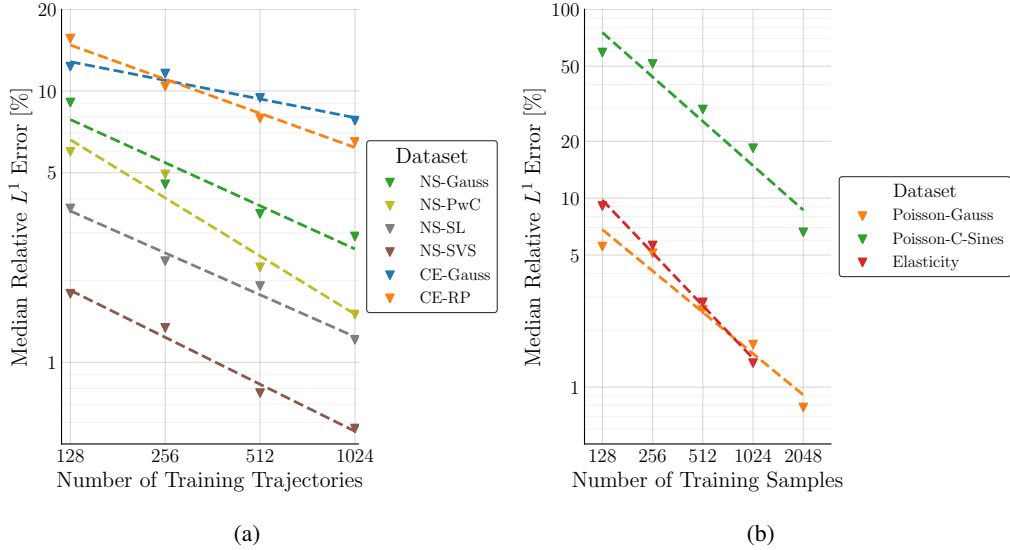


Figure E.4: Relative L^1 test errors against the size of training dataset. The left plot shows these results for the time-dependent fluid datasets, and the right plot for time-independent datasets. The lines show linear regression slopes for each dataset.

1272 data availability. Across all these static problems, we observe a consistent downward slope in error as
 1273 the number of samples increases, again underscoring the advantage of larger training sets.

1274 Overall, in both dynamic (time-dependent) and static (time-independent) scenarios, GAOT exhibits a
 1275 scalable relationship between training set size and error reduction. As the training data grows, the
 1276 learned operator converges more reliably to the underlying PDE solution. This robust data scaling
 1277 property supports our premise that GAOT can serve as a strong foundation model backbone for PDE
 1278 tasks, becoming increasingly accurate with more extensive datasets.

1279 E.5 Resolution Invariance

1280 One of the core properties for operator learning is resolution invariance—the ability to train on a specific
 1281 discretization yet accurately predict solutions at higher/lower resolutions. To validate this property in
 1282 our GAOT framework, we conduct experiments on a time-independent PDE, Poisson-Gauss.

1283 Figure E.5 illustrates the resolution invariance capabilities of GAOT. In this experiment, GAOT was
 1284 trained using data discretized by 2048 points. Its performance was then evaluated across a spectrum

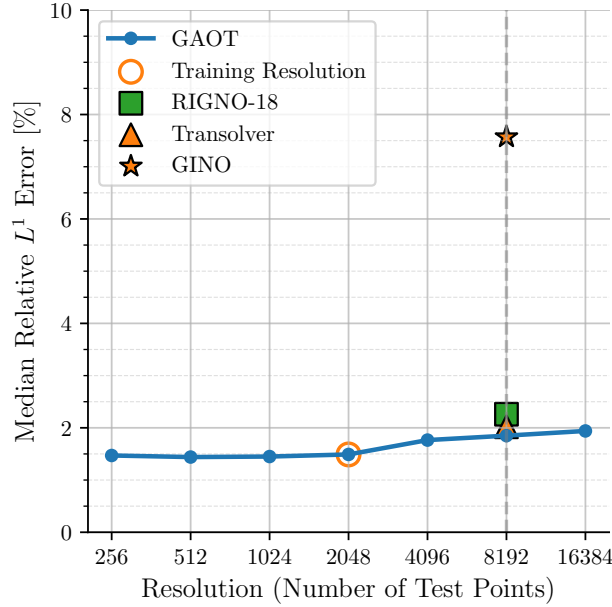


Figure E.5: The GAOT model is trained at a resolution of 2048 and evaluate at various test resolutions. The results for RIGNO-18, Transolver and GINO correspond to models trained and tested at a resolution of 8192.

of seven distinct resolutions: three sub-resolution settings (256, 512, and 1024 points), the training resolution itself (2048 points), and three super-resolution settings (4096, 8192, and 16384 points). For comparative purposes, Figure E.5 also displays the performance of the top three baseline models from Table 1 (excluding GAOT itself), namely RIGNO-18, Transolver, and GINO. These baseline results were obtained from models that were both trained and tested at a resolution of 8192 points.

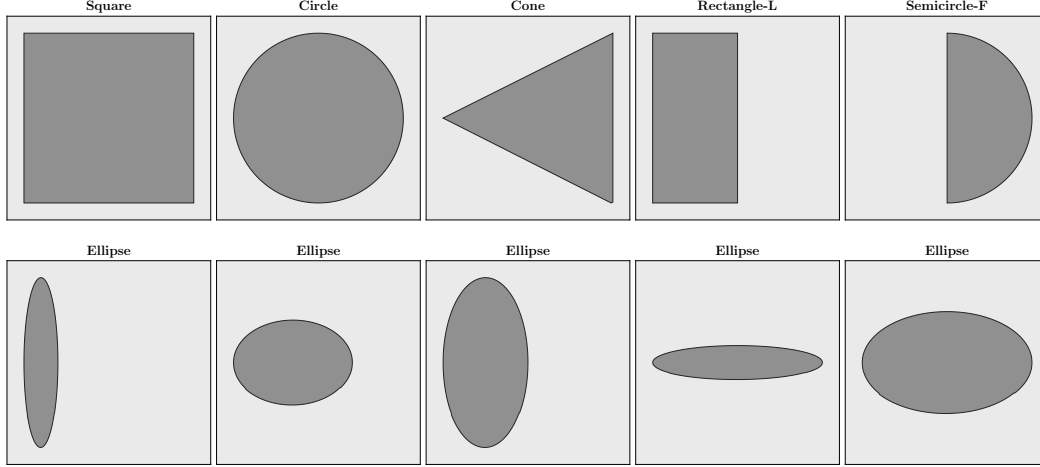
The results demonstrate that GAOT possesses excellent resolution invariance. Notably, even when trained at a resolution of 2048 points, GAOT not only generalizes well to higher resolutions but also achieves the best performance when tested at 8192 points. It outperforms the baseline models which were specifically trained for and tested at this higher resolution (8192 points), underscoring GAOT’s efficiency and robustness in learning resolution-independent solution operators.

E.6 Transfer Learning

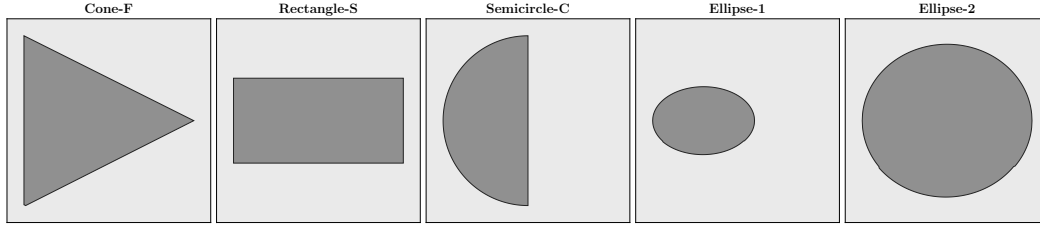
The set of geometries illustrated in Figure E.6a, represent the varying bluff-body geometries in the Bluff-Body dataset, which is one of the benchmarks presented in Tab. 1 of the main text. This dataset is constructed by simulating compressible flow across diverse bluff-body geometries at varying Ma and α , as described in Sec. D.2. The distinct shapes depicted in Figure E.6b were specifically employed for the fine-tuning stage of our transfer learning experiments. The corresponding transfer learning performance, demonstrating the model’s ability to adapt from the shapes used for pretraining to the novel ones indicated in Figure E.6b, is presented in Figure 3(c) in the main text.

E.7 Training Randomness

In order to quantify the dependence of the final model performance on the inherent randomness in the training process, such as in weight initialization, we trained the GAOT model six independent times. Each training run utilized a different seed for the pseudo-random number generator. These experiments were conducted on the Bluff-Body dataset. The statistics of the resulting relative L^1 test errors across these six runs are summarized in Table E.4. The standard deviation of these errors is 0.12. This relatively small standard deviation suggests that the GAOT model exhibits good stability with respect to the random aspects of the training procedure.



(a) Shapes utilized for pretraining in the transfer learning experiments.



(b) Bluff body shapes employed for the fine-tuning (FT) phase of the transfer learning task.

Figure E.6: The geometries in (a) are included in the Bluff-Body dataset in Tab. 1. Shape-* (*: C, F, S, L; Shape: Semicircle, Cone, Rectangle) indicates shapes and their contact surfaces (*) with respect to the flow. Here, F - flat surface, C - curved surface, L - larger side, S - smaller side.

Table E.4: Statistics of relative L^1 test errors with different random seeds. We train GAOT on Bluff-Body dataset, which is repeated 6 times.

Dataset	Error [%]
	Mean \pm Standard deviation
Bluff-Body	2.39 ± 0.12

F Ablation Studies

F.1 Encode-Process-Decode

In this subsection, we investigate the performance of four different *encode-process-decode* architectures on both time-dependent and time-independent PDE benchmarks. The four models considered are GAOT (ours), Regional Attentional Neural Operator (RANO), Regional Fourier Neural Operator (RFNO) and GINO [29], with components are *Message-Passing (MP)* graph neural network [16], *Transformer* [49], *Fourier Neural Operator (FNO)* [27], *Graph Neural Operator (GNO)* [28] and proposed *Multi-scal Attentional GNO (MAGNO)*. Table F.1 summarizes the components of each model. All variants follow an *encode-process-decode* pipeline but differ in how graph, Fourier, or transformer-based mechanisms are deployed.

Figure F.1 shows the *median relative L^1 error* for each model on six PDE datasets (4 time-dependent PDEs, 2 time-independent PDEs). All models are trained for 500 epochs under the same data splits and hyperparameter conditions. We can see that GAOT consistently achieves strong performance and robustness across all six datasets. Its errors remain low, highlighting the effectiveness of combining MAGNO for local geometric encoding with transformer-based global attention. GINO ranks second

Model	Encode	Process	Decode
GAOT	MAGNO	Transformer	MAGNO
RANO	MP	Transformer	MP
RFNO	MP	FNO	MP
GINO	GNO	FNO	GNO

Table F.1: Components for different encode–process–decode designs.

in overall accuracy, yet exhibits noticeable difficulties on NS-Gauss and Poisson-C-Sines. RANO and RFNO perform moderately well on simpler datasets (e.g. Elasticity), but show instability on more challenging tasks (e.g. NS-SVS or NS-Gauss). This indicates that reliance on message-passing or FNO-based processors alone may not be sufficient to handle diverse PDE and geometry conditions with the same level of robustness.

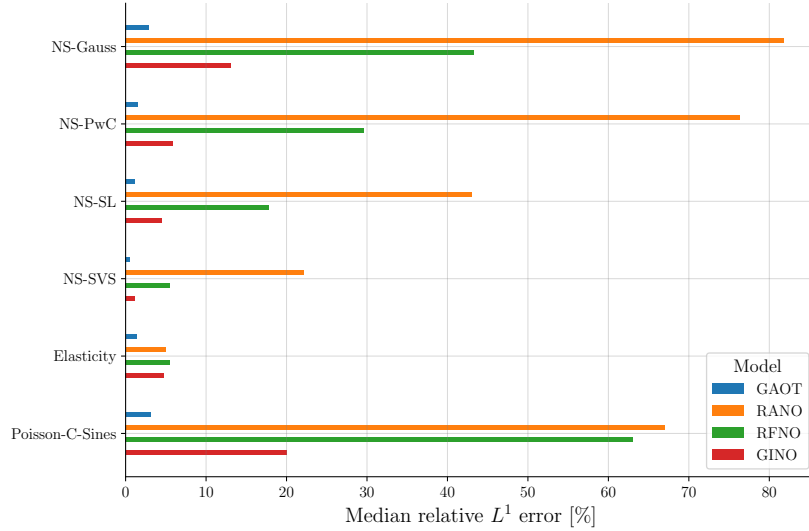


Figure F.1: Median relative L^1 errors (%) of GAOT, RANO, RFNO, and GINO on six PDE benchmarks.

Overall, these results reinforce GAOT’s stability across multiple PDE settings. Even with a fixed training protocol (500 epochs for each dataset), GAOT consistently converges faster and more reliably, underscoring the advantage of geometry-aware tokens, multiscale attention, and the flexible transformer backbone.

F.2 Tokenization Strategies

In Section B.1, we have introduced three tokenization methods. Here, we compare these strategies on two datasets, Elasticity and Poisson-C-Sines. Figure F.2 shows the final median relative L^1 errors for each approach. The Strategy I consistently achieves the best performance on both unstructured datasets. Strategy II & III perform similarly to Strategy I on simpler datasets (elasticity), but can fail to converge on the more challenging one, Poisson-C-Sines. Similar situations also happen on models like UPT and GNOT in Tab. 1 of main text. Overall, Strategy I emerges as the most robust approach in our current experiments. While Strategies II and III show promise, they require more careful optimization to match Strategy I’s reliability.

Next, we focus on Strategy I and study how varying the *number of latent tokens (LT)*, *patch size (PS)*, and *radius (GR)* affect performance. Note that here we do not use multiscale radii; each token has a single radius. Table F.2 summarizes experiments on the elasticity and Poisson-Gauss datasets. Results show that fewer tokens (e.g., [32,32]) can degrade performance in some cases (elasticity), presumably because the domain coverage becomes coarser, making it harder to capture local variations. More tokens ([64,64] or [128,128]) typically improve accuracy and stabilize convergence. Nevertheless, computational costs rise when the number of tokens grows, as transformer

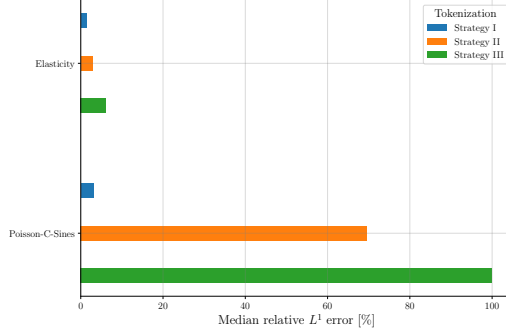


Figure F.2: Median relative L^1 errors (%) comparing three tokenization strategies on Elasticity, and Poisson-C-Sines. The Strategy I, II, III corresponds to the methods discussed in Section B.1.

Table F.2: Median relative L^1 errors (%), parameter counts, and training time with different numbers of latent tokens (LT), patch sizes (PS), and radii (GR).

Model Size		Hyperparameters			Median Relative L^1 Error [%]	
Params [M]	Time [s/it]	LT	PS	GR	Elasticity	Poisson-Gauss
5.60	10.1	[64, 64]	2	0.033	1.80	1.05
6.00	3.06	[64, 64]	4	0.033	1.71	1.57
10.7	2.20	[64, 64]	8	0.033	1.60	1.65
5.56	10.1	[32, 32]	1	0.066	3.41	1.22
5.60	3.00	[32, 32]	2	0.066	2.25	1.22
6.00	11.8	[128, 128]	4	0.033	1.67	1.72
10.7	5.02	[128, 128]	8	0.033	1.62	1.22

attention scales quadratically with token count. Increasing the patch size (PS) reduces the number of tokens entering the transformer, lowering the training time. Encouragingly, performance does not degrade sharply with larger patches. For instance, going from $PS = 2$ to 8 is fairly stable across datasets. Note that the overall parameter count can increase if each token aggregates larger local features, but in practice, training runs faster due to fewer tokens in self-attention. Radius (GR) grows if we reduce the number of latent tokens because we need to ensure coverage of the entire physical domain by enlarging the receptive field. This is critical for unstructured or irregular samples, especially if tokens must capture a bigger subregion.

F.3 Time-Stepping Method

We now investigate how different *time-stepping* formulations (see Section B.5) affect performance on time-dependent PDEs. Specifically, we compare the output, residual, and derivative stepping strategies. Table F.3 reports the median relative L^1 errors for six representative fluid dynamics benchmarks on regular grids.

Table F.3: Median relative L^1 errors (%) at final time t_{14} for GAOT with three different time-stepping methods.

Dataset	Median relative L^1 error [%]		
	Output	Residual	Derivative
NS-Gauss	3.57	3.60	2.52
NS-PwC	1.95	1.70	1.23
NS-SL	1.78	1.49	1.29
NS-SVS	0.60	0.60	0.56
CE-Gauss	8.80	8.93	7.97
CE-RP	5.17	6.12	5.94

As shown, modeling the operator as a time derivative (derivative column) often yields the lowest final-time errors on all but one dataset (CE-RP, where the *Output* strategy slightly outperforms the others). We hypothesize that treating the operator as $\partial_t u$ naturally enforces a continuous dependence on time, analogous to neural ODEs or residual networks [19, 9], which can improve stability and accuracy over multiple steps. In experiments involving time-dependent PDEs, we therefore use derivative time stepping as the default unless stated otherwise. This approach not only achieves strong final-time accuracy, but also aligns with our design goal of a differentiable, time-continuous operator.

F.4 Geometric Embedding

As discussed in Section B.3, our framework incorporates a *geometric embedding network* to encode shape and domain information separately from the physical (PDE) state. Table F.4 compares these geometric embedding approaches against a baseline "original" (i.e., no additional geometry embedding) on two original unstructured datasets (Wave-C-Sines, Poisson-C-Sines).

Table F.4: Median relative L^1 errors (%) for various geometry embedding approaches. Original omits geometric embedding, while Statistical and PointNet follow Section B.3.

Dataset	Median relative L^1 error [%]		
	original	statistical	pointnet
Wave-C-Sines	6.50	5.69	6.07
Poisson-C-Sines	6.60	4.66	23.7

In the unstructured datasets, including Wave-C-Sines, and Poisson-C-Sines, explicitly encoding domain geometry yields a more pronounced benefit. In particular, the statistical strategy consistently outperforms PointNet on these irregular meshes, and in Poisson-C-Sines, training with the PointNet approach appears unstable (23.7% error). Based on these observations, we use statistical embedding by default for unstructured dataset given its stable and superior performance in most cases.

F.5 multiscale Features

As introduced in Section B.2, our encoder can capture multiscale local information by aggregating neighborhood features across multiple radii. Specifically, we compare:

- Single-scale: using a single fixed radius of 0.033 for each point.
- multiscale: using three radii [0.022, 0.033, 0.044] for each point.

Table F.5: Median relative L^1 errors (%) comparing single-scale vs. multiscale features.

Dataset	Median relative L^1 error [%]	
	Single-scale	multiscale
Wave-C-Sines	5.69	4.6
Poisson-C-Sines	4.66	3.04

Table F.5 reports the mean relative L^1 errors on unstructured datasets including Wave-C-Sines and Poisson-C-Sines. Results show that multiscale neighbors yield a clear reduction in error. For instance, in Poisson-C-Sines, the error decreases from 4.66% to 3.04%. This contrast reflects the fact that a single, fixed receptive field on a regularly spaced grid is often sufficient. However, on unstructured domains where the mesh density can vary, using multiple radii helps the network capture both fine and coarse local structures.

G Visualizations of Datasets

Estimates produced by trained models are visualized in this section for different datasets.

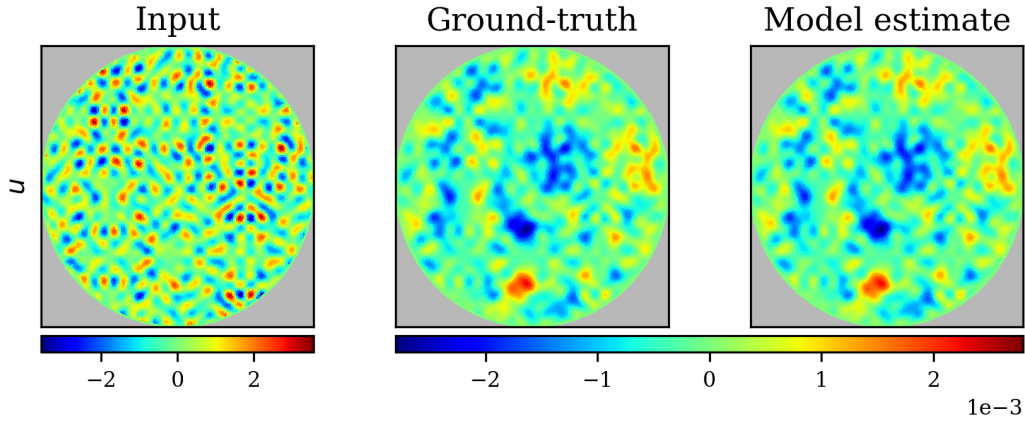


Figure G.1: Model input, ground-truth solution, and model estimate of a test sample of the Poisson-C-Sines dataset.

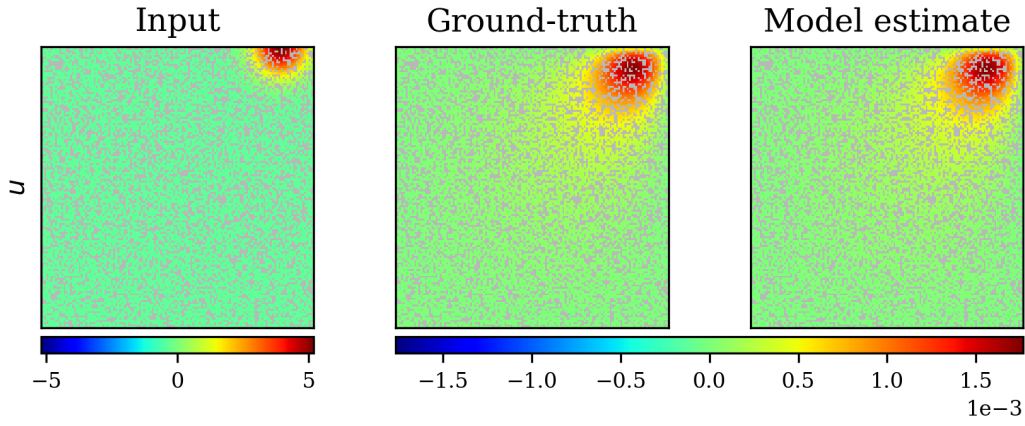


Figure G.2: Model input, ground-truth solution, and model estimate of a test sample of the Poisson-Gauss dataset.

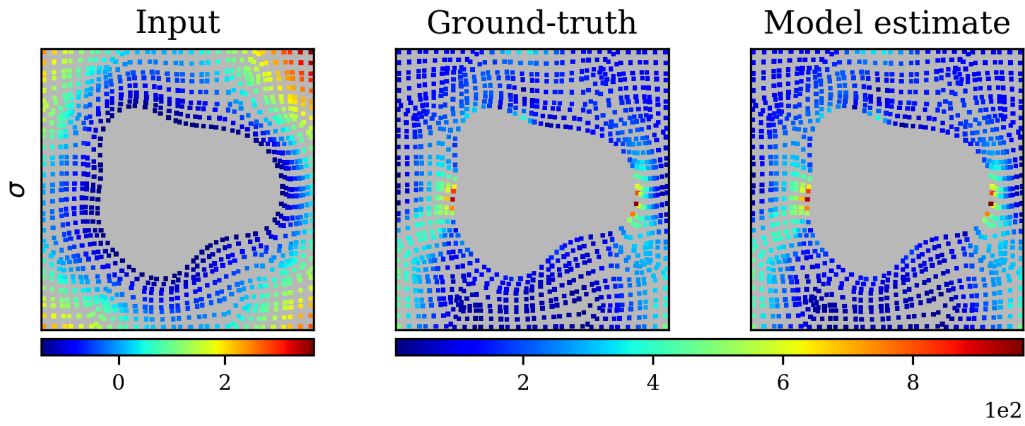


Figure G.3: Model input, ground-truth solution, and model estimate of a test sample of the Elasticity dataset.

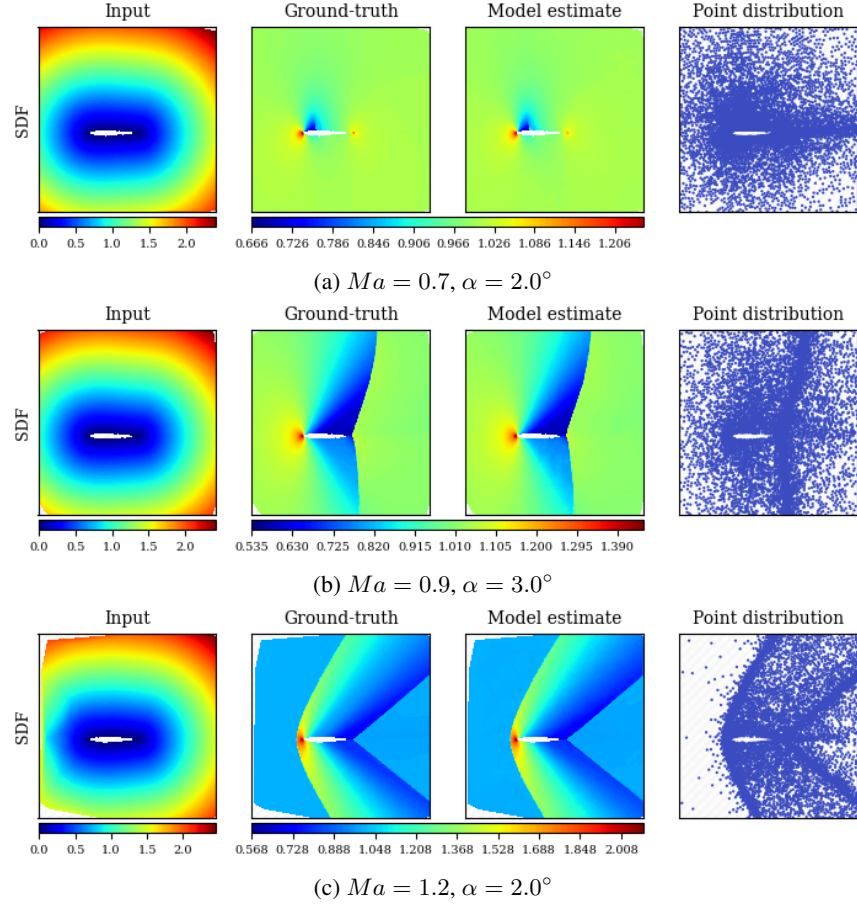


Figure G.4: Model input, ground-truth solution, model estimate and point distribution of test samples of the NACA0012 dataset.

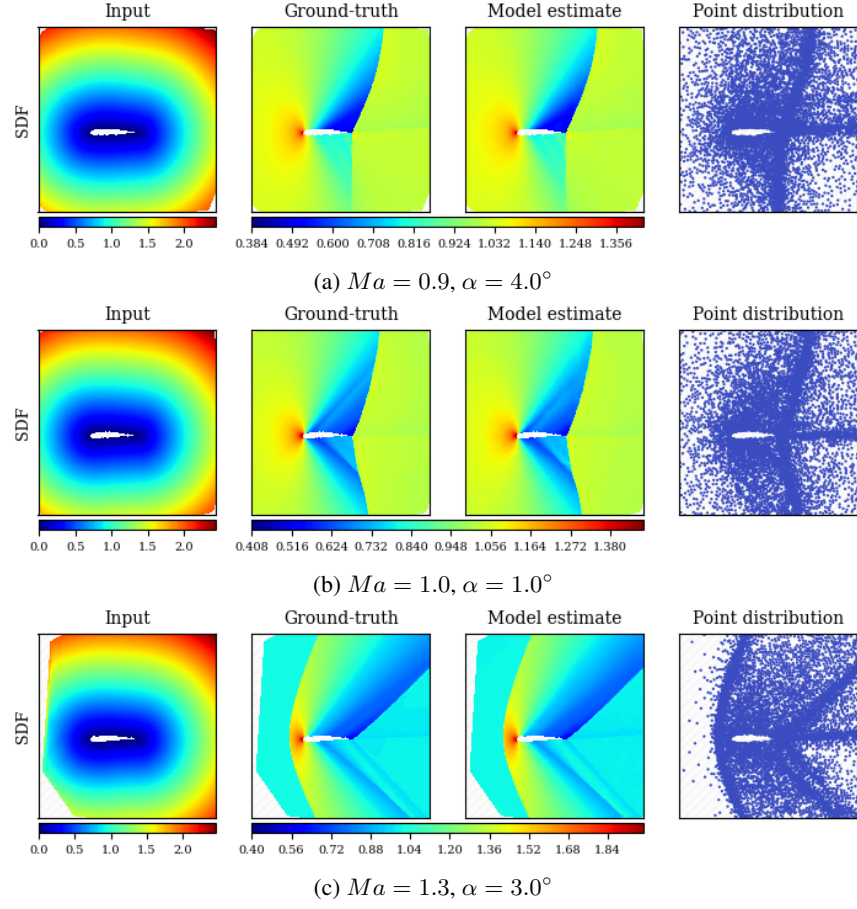


Figure G.5: Model input, ground-truth solution, model estimate and point distribution of test samples of the NACA2412 dataset.

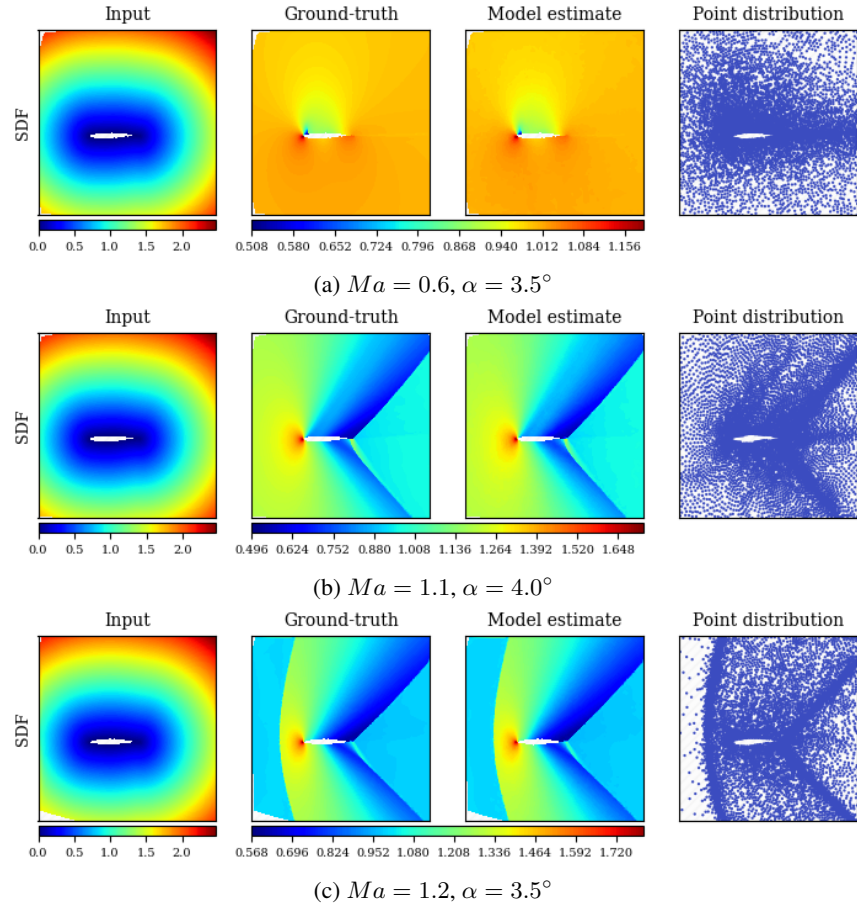


Figure G.6: Model input, ground-truth solution, model estimate and point distribution of test samples of the RAE2822 dataset.

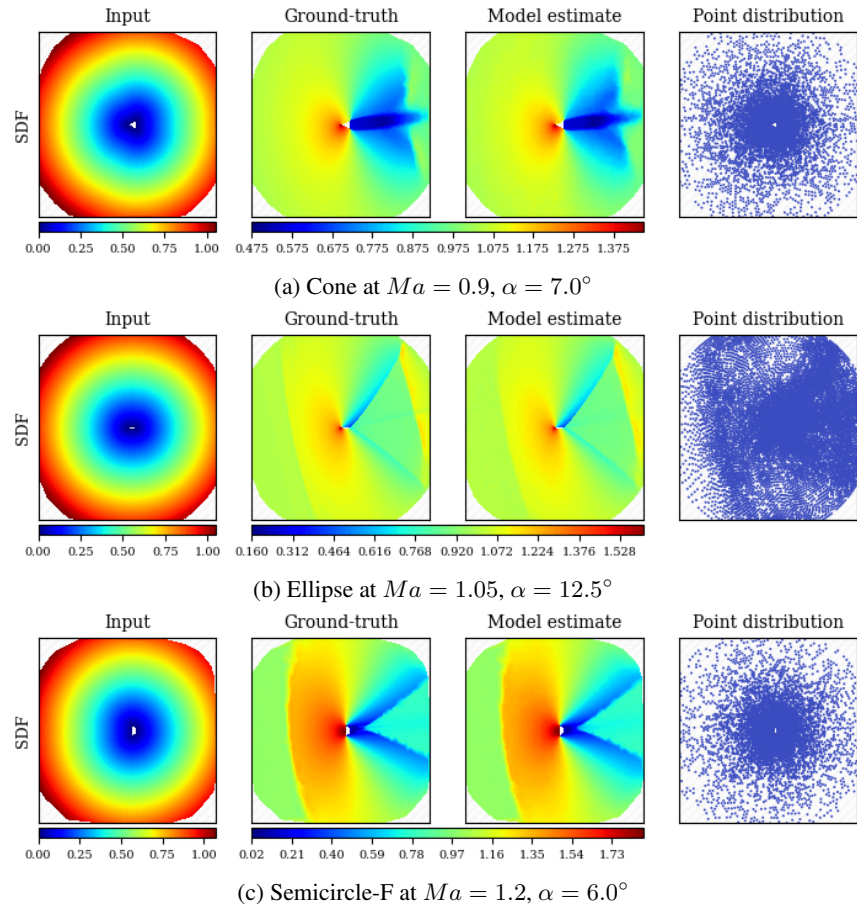


Figure G.7: Model input, ground-truth solution, model estimate and point distribution of test samples of the Bluff-Body dataset.

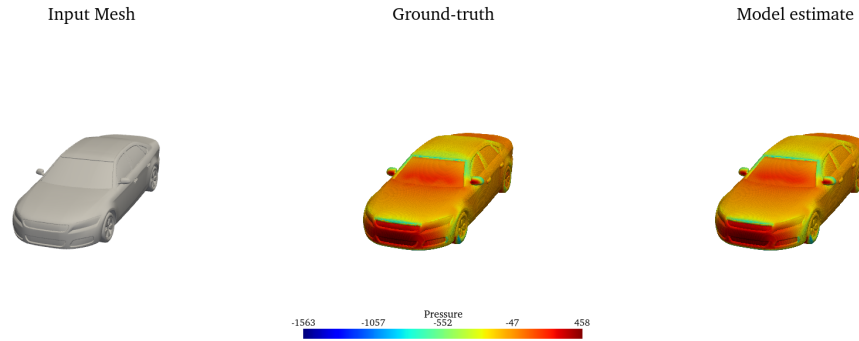


Figure G.8: Model input, ground-truth solution, model estimate of a test sample N_S_WWS_WM_172 of the surface pressure on the DrivAerNet++.

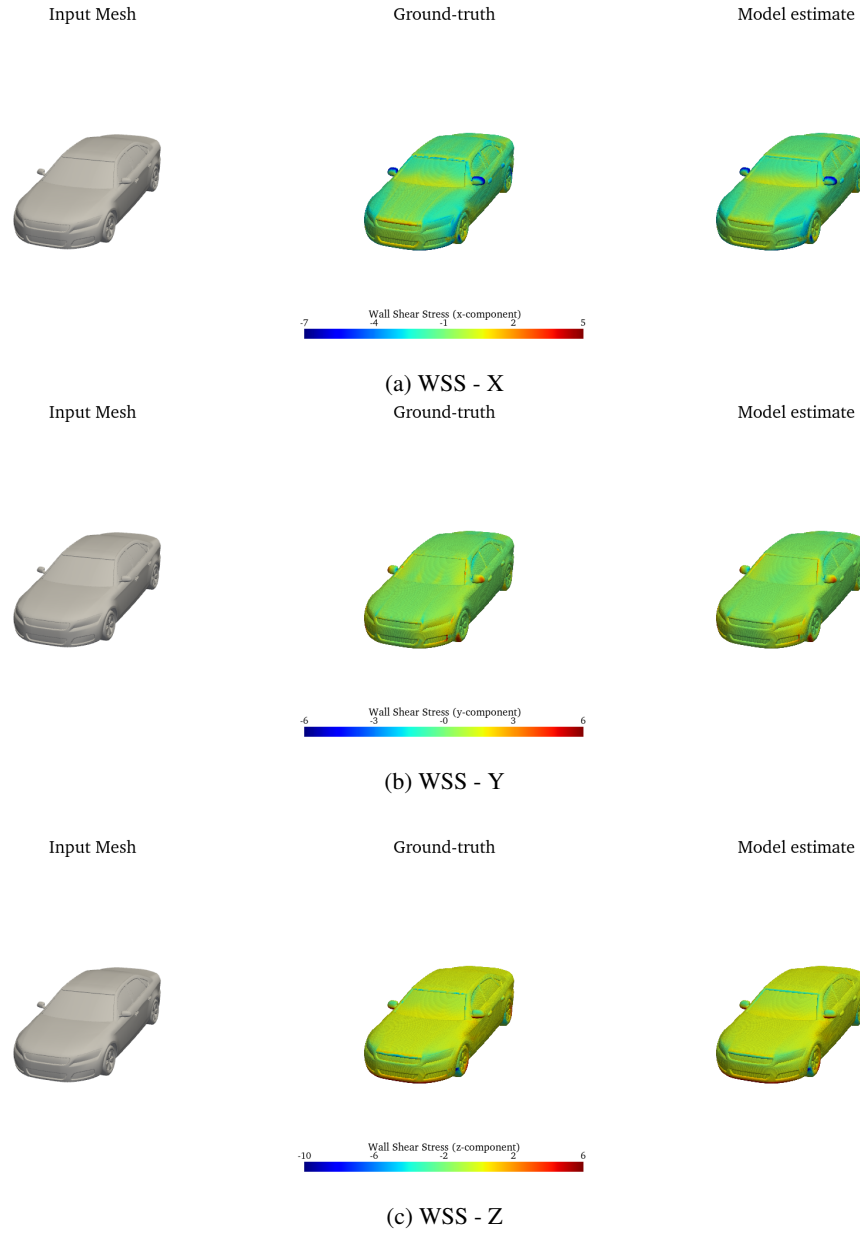


Figure G.9: Model input, ground-truth solution, model estimate of a test sample N_S_WWS_WM_172 of the surface wall shear stress on the DrivAerNet++.

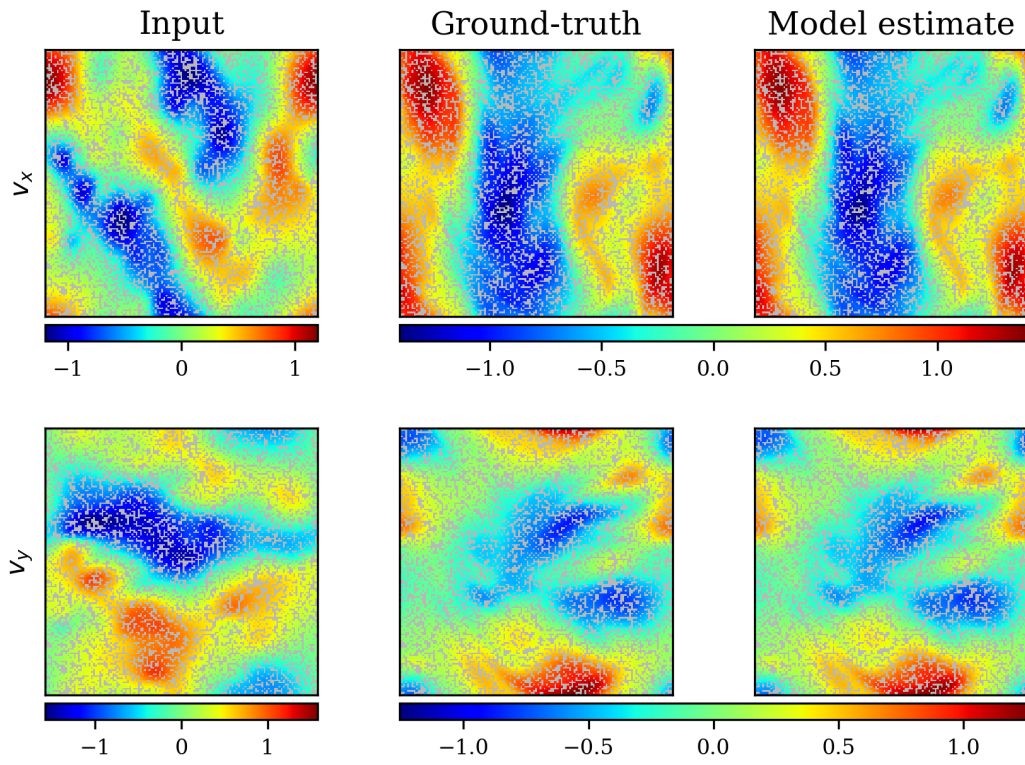


Figure G.10: Model input at $t = t_0$, ground-truth solution and model estimate at $t = t_{14}$ of a test sample unstructured NS-Gauss dataset.

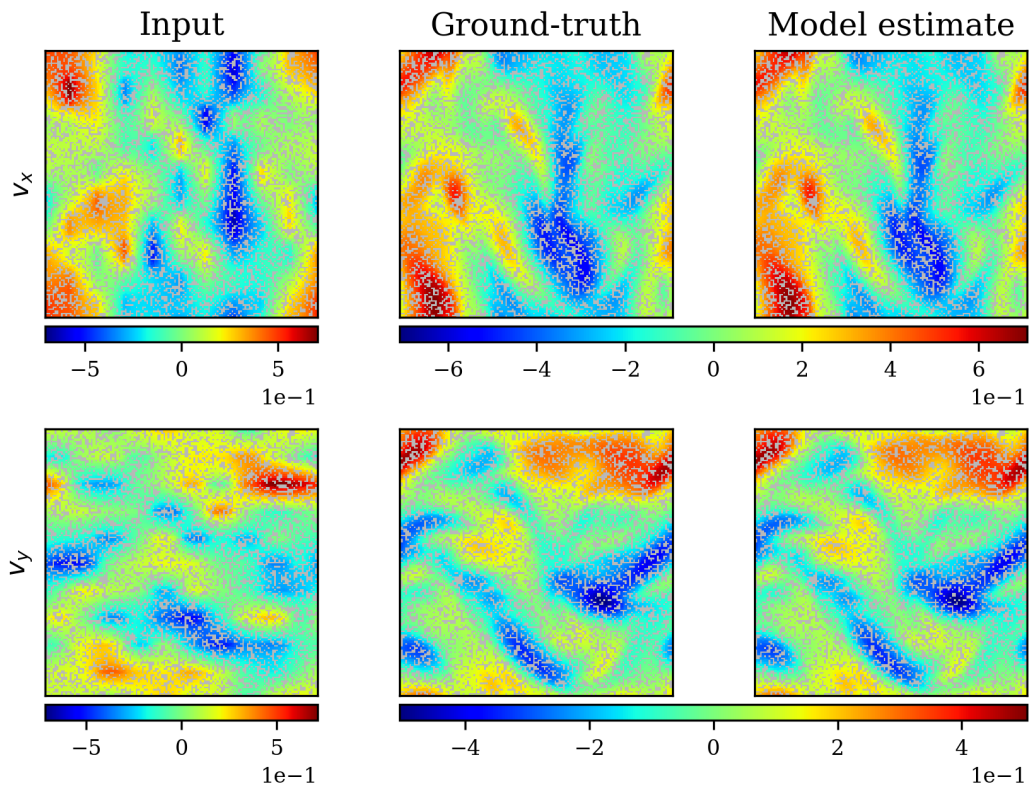


Figure G.11: Model input at $t = t_0$, ground-truth solution and model estimate at $t = t_{14}$ of a test sample unstructured NS-PwC dataset.

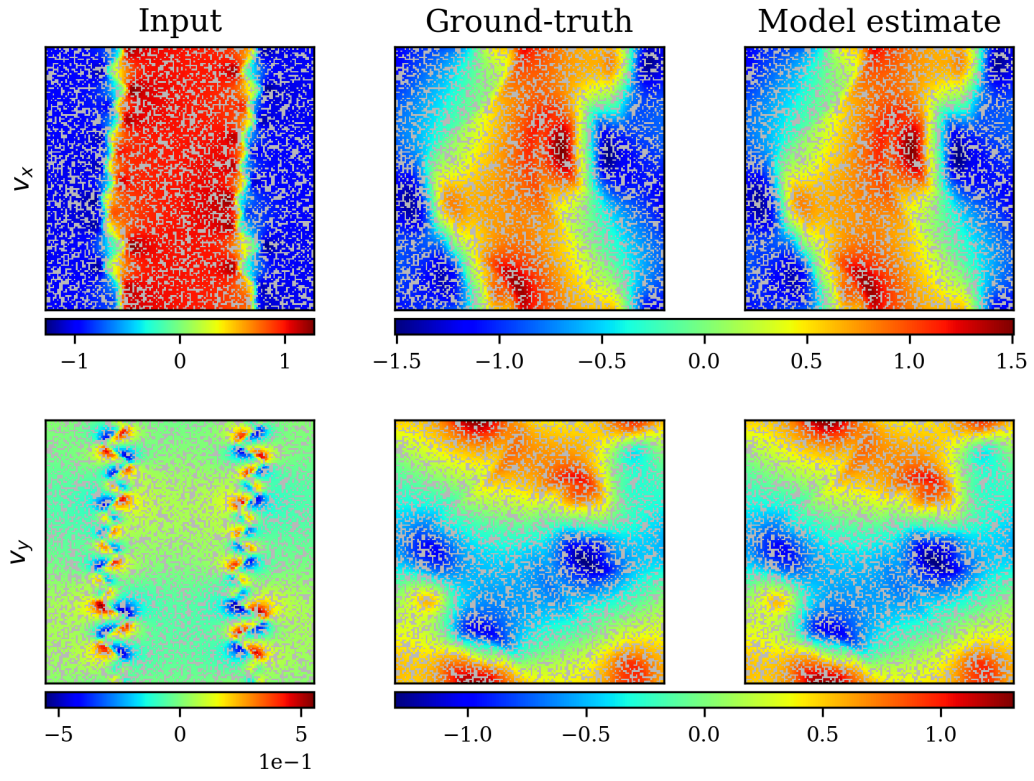


Figure G.12: Model input at $t = t_0$, ground-truth solution and model estimate at $t = t_{14}$ of a test sample unstructured NS-SL dataset.

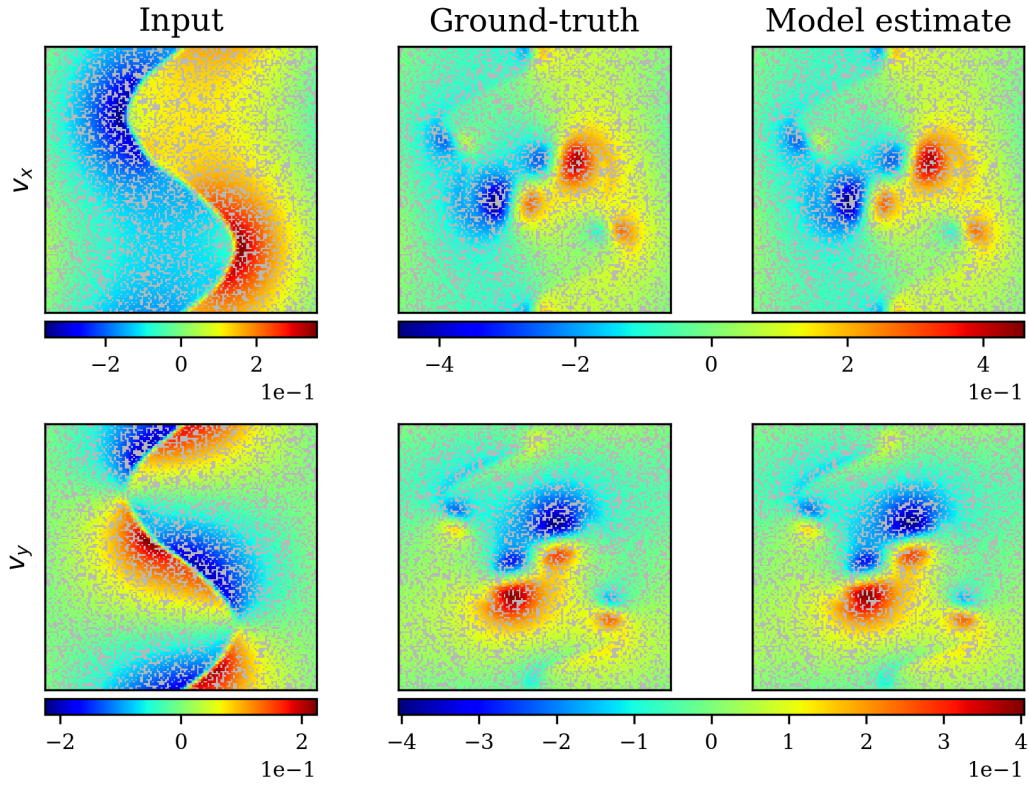


Figure G.13: Model input at $t = t_0$, ground-truth solution and model estimate at $t = t_{14}$ of a test sample unstructured NS-SVS dataset.

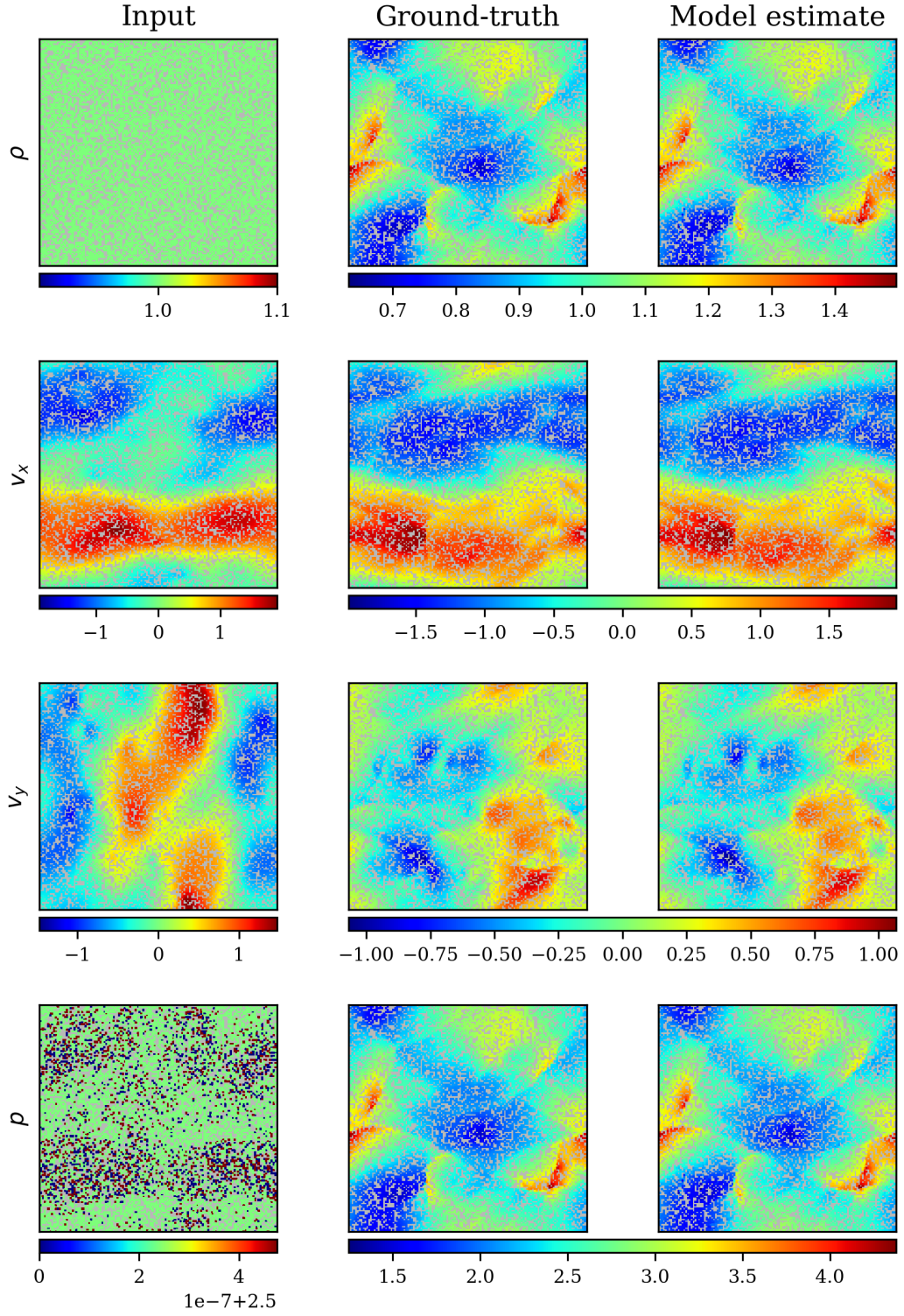


Figure G.14: Model input at $t = t_0$, ground-truth solution and model estimate at $t = t_{14}$ of a test sample unstructured CE-Gauss dataset.

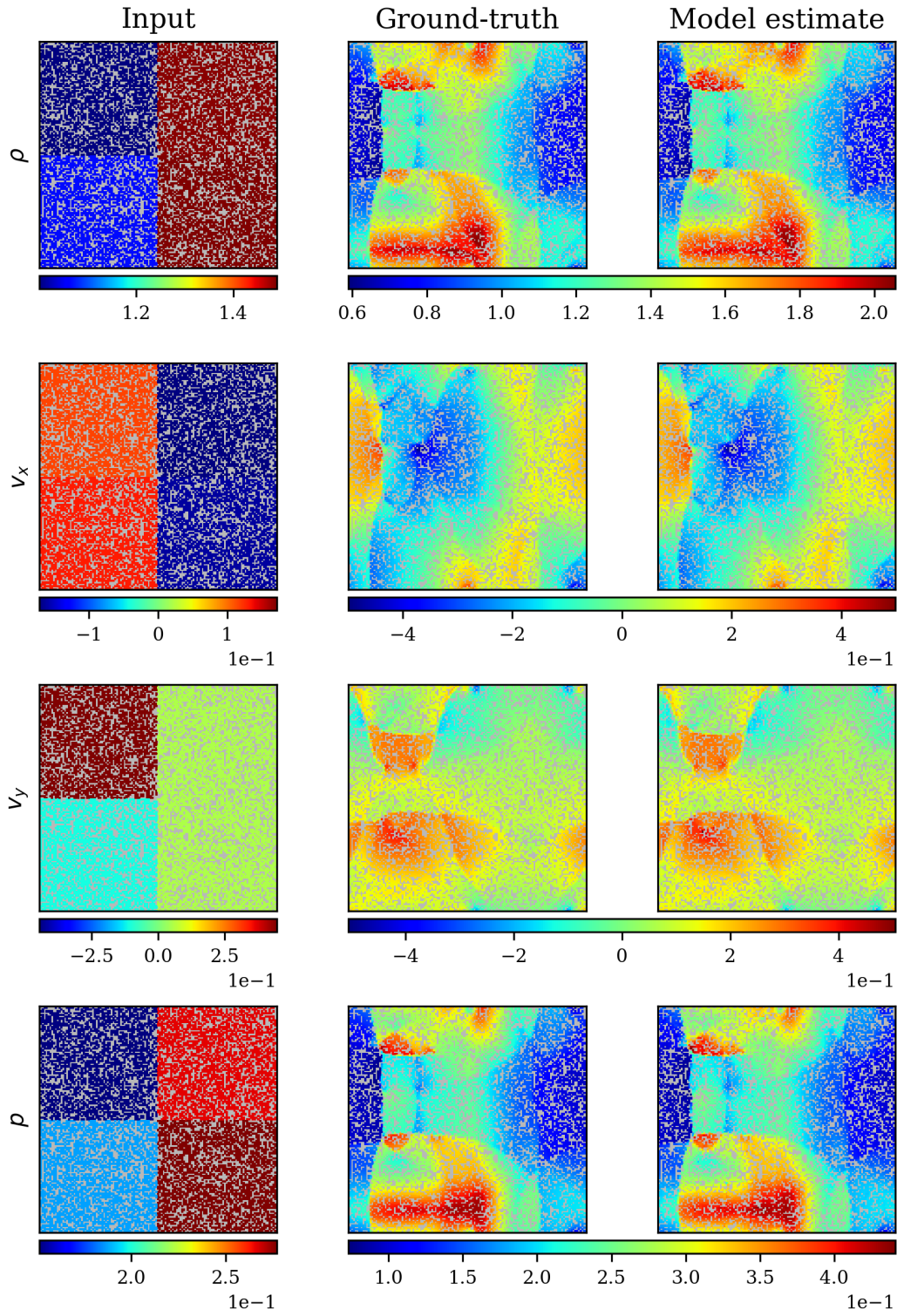


Figure G.15: Model input at $t = t_0$, ground-truth solution and model estimate at $t = t_{14}$ of a test sample unstructured CE-RP dataset.

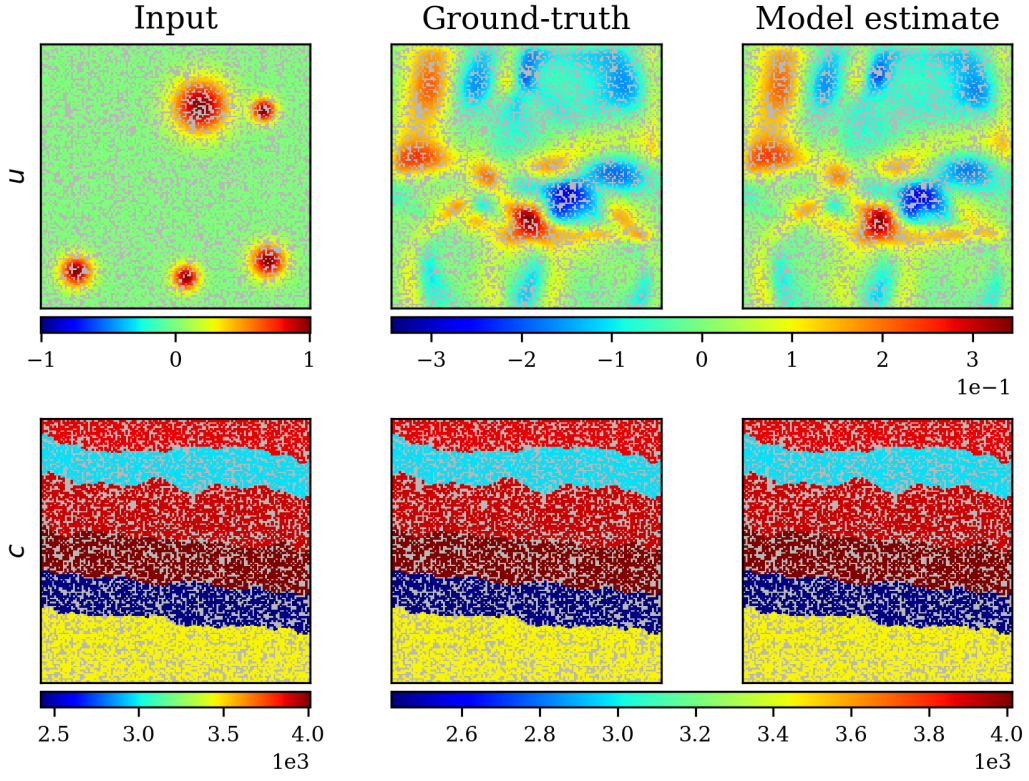


Figure G.16: Model input at $t = t_0$, ground-truth solution and model estimate at $t = t_{14}$ of a test sample unstructured Wave-Layer dataset.

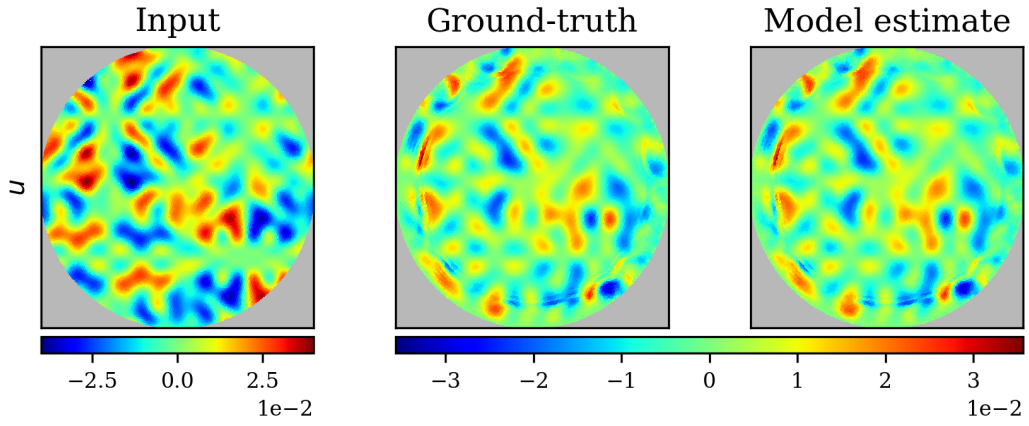


Figure G.17: Model input at $t = t_0$, ground-truth solution and model estimate at $t = t_{14}$ of a test sample Wave-C-Sines dataset.

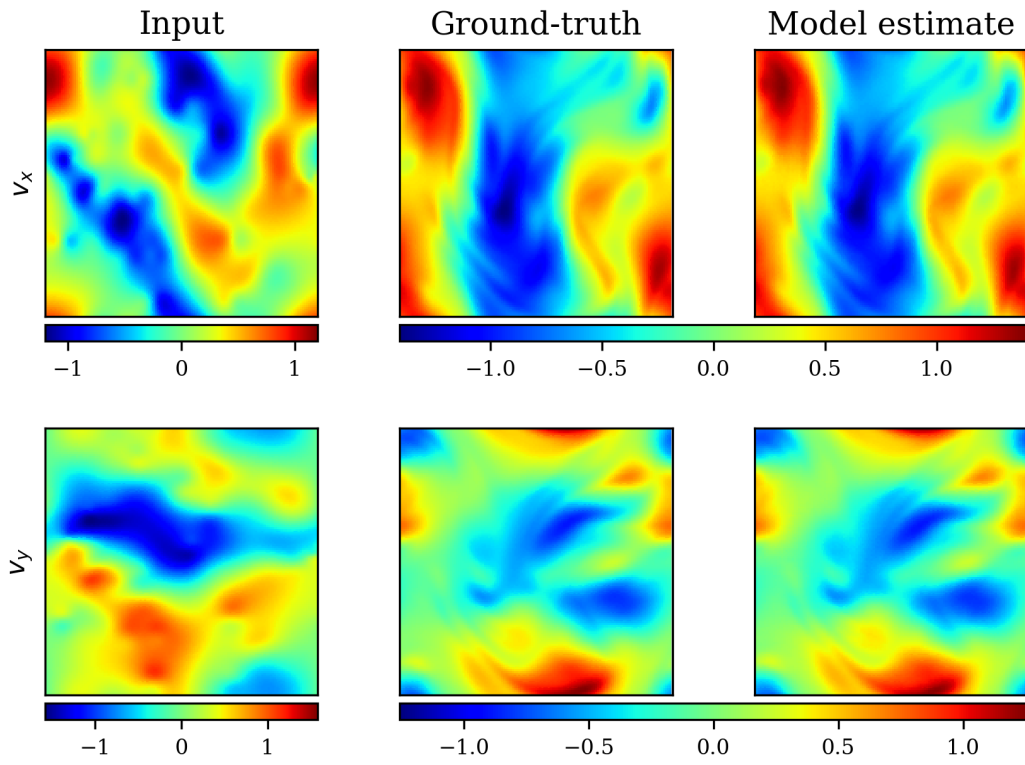


Figure G.18: Model input at $t = t_0$, ground-truth solution and model estimate at $t = t_{14}$ of a test sample NS-Gauss dataset.

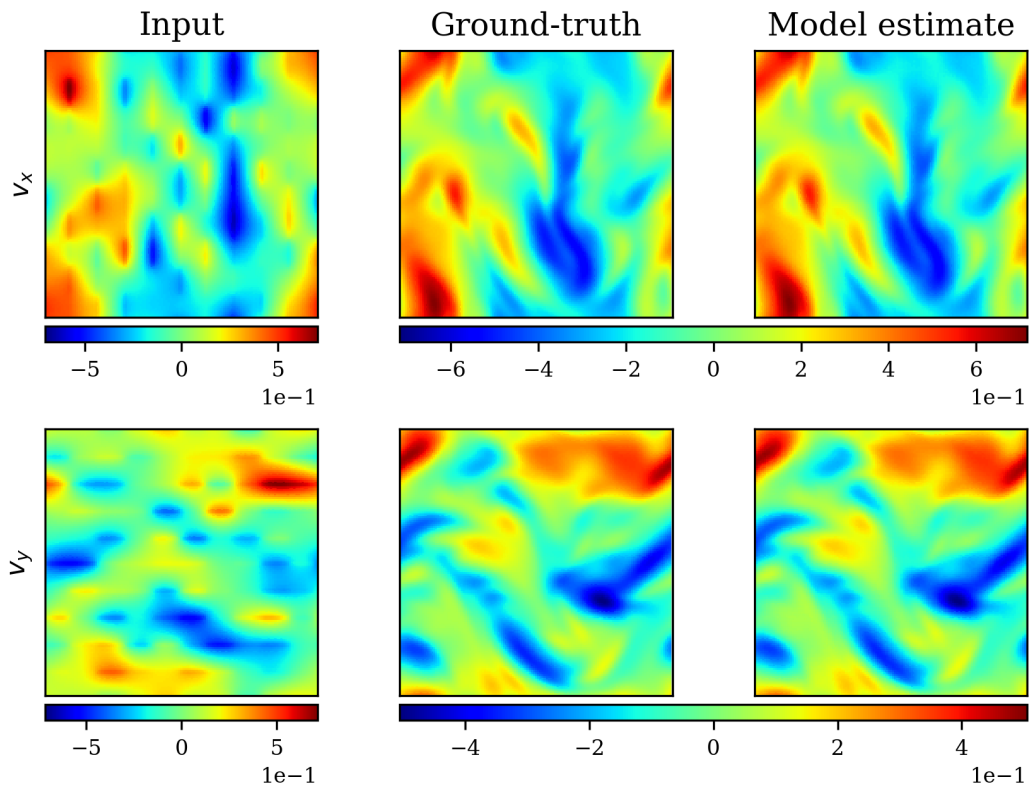


Figure G.19: Model input at $t = t_0$, ground-truth solution and model estimate at $t = t_{14}$ of a test sample NS-PwC dataset.

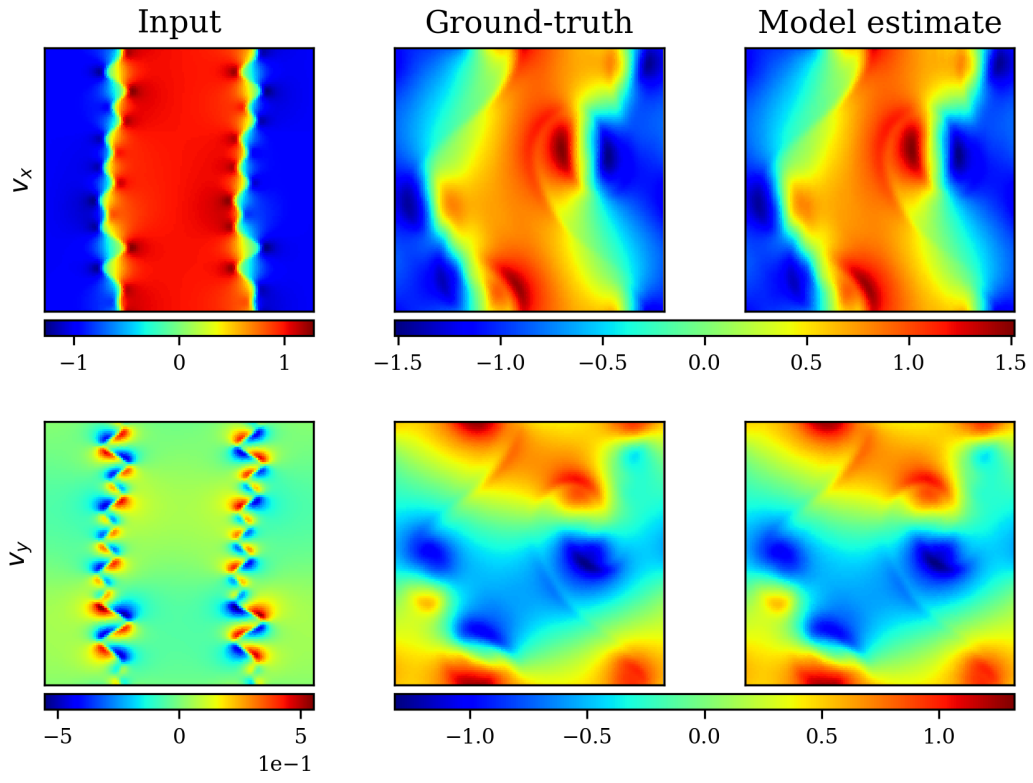


Figure G.20: Model input at $t = t_0$, ground-truth solution and model estimate at $t = t_{14}$ of a test sample NS-SL dataset.

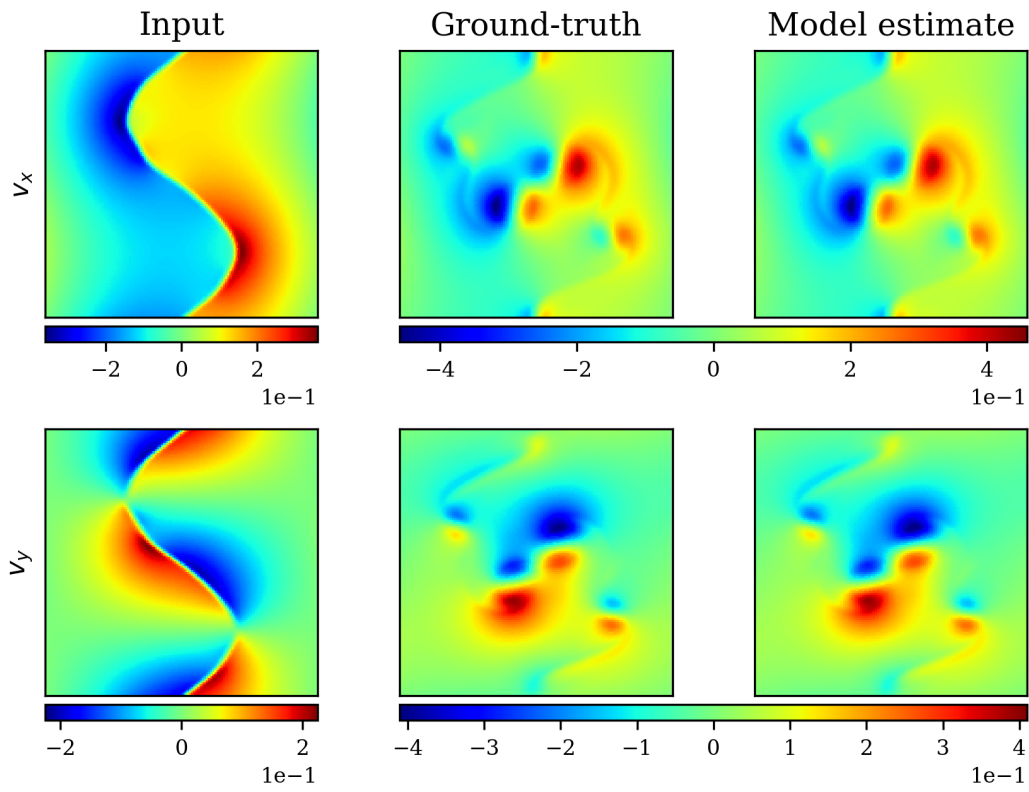


Figure G.21: Model input at $t = t_0$, ground-truth solution and model estimate at $t = t_{14}$ of a test sample NS-SVS dataset.

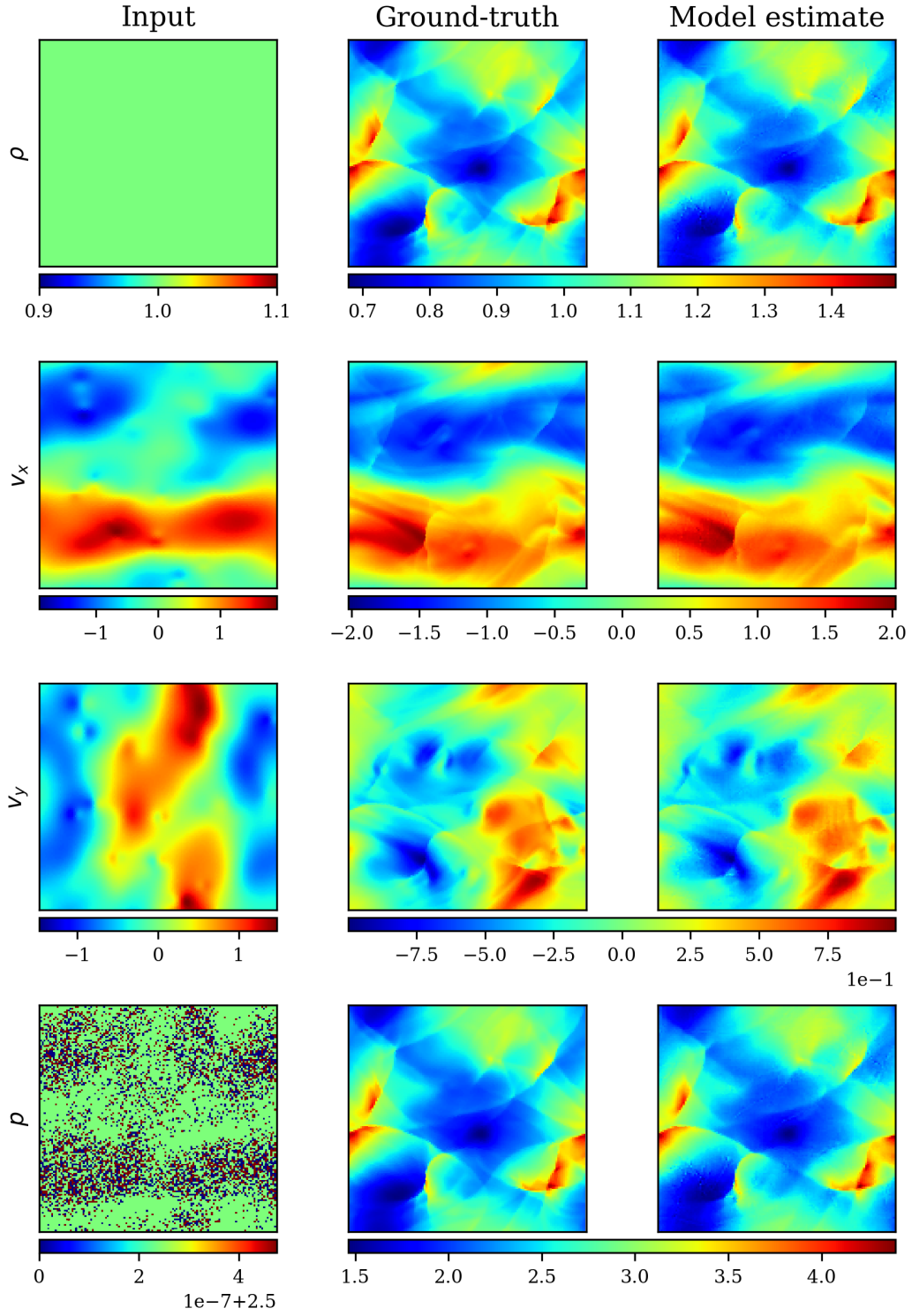


Figure G.22: Model input at $t = t_0$, ground-truth solution and model estimate at $t = t_{14}$ of a test sample CE-Gauss dataset.

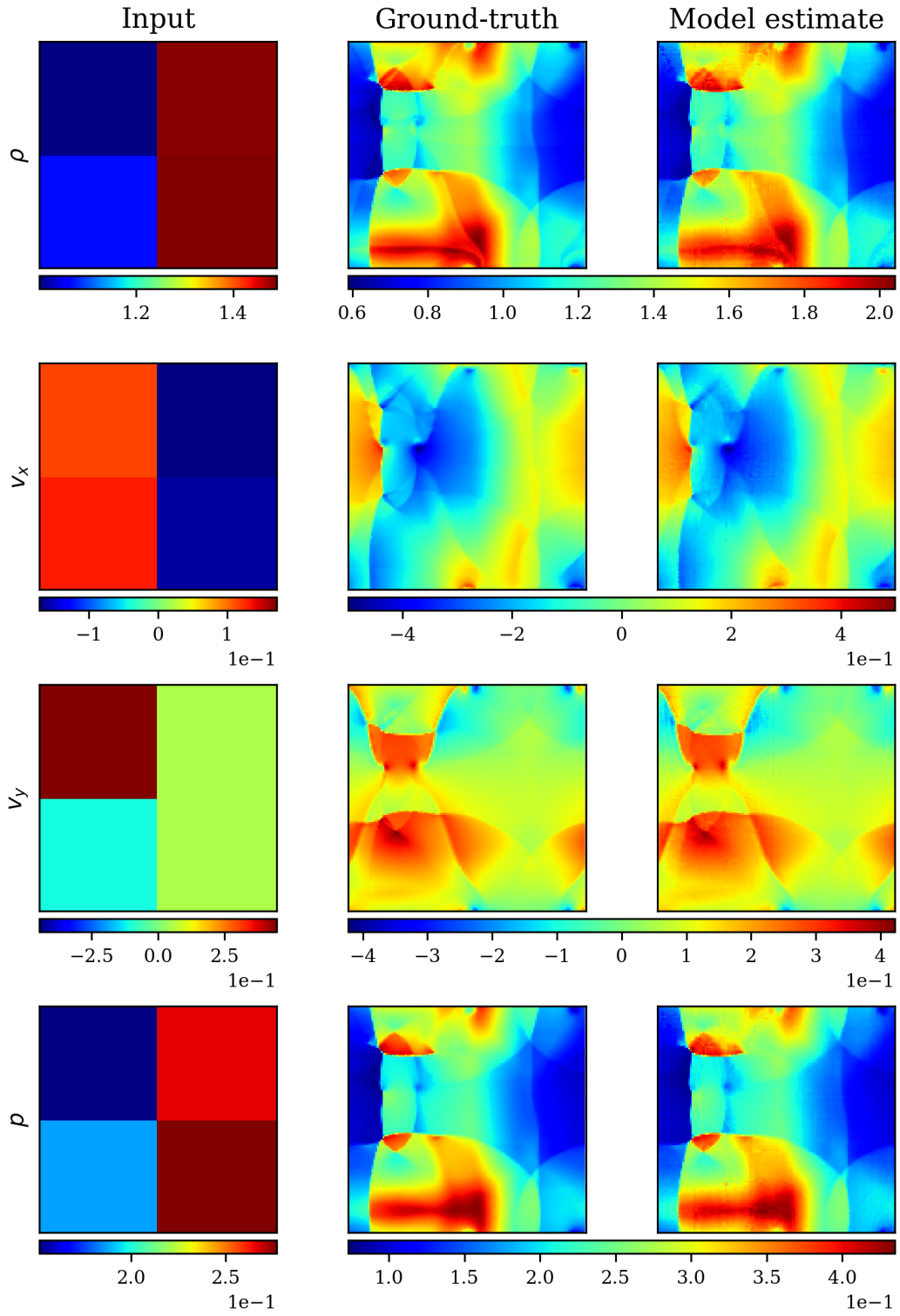


Figure G.23: Model input at $t = t_0$, ground-truth solution and model estimate at $t = t_{14}$ of a test sample CE-RP dataset.

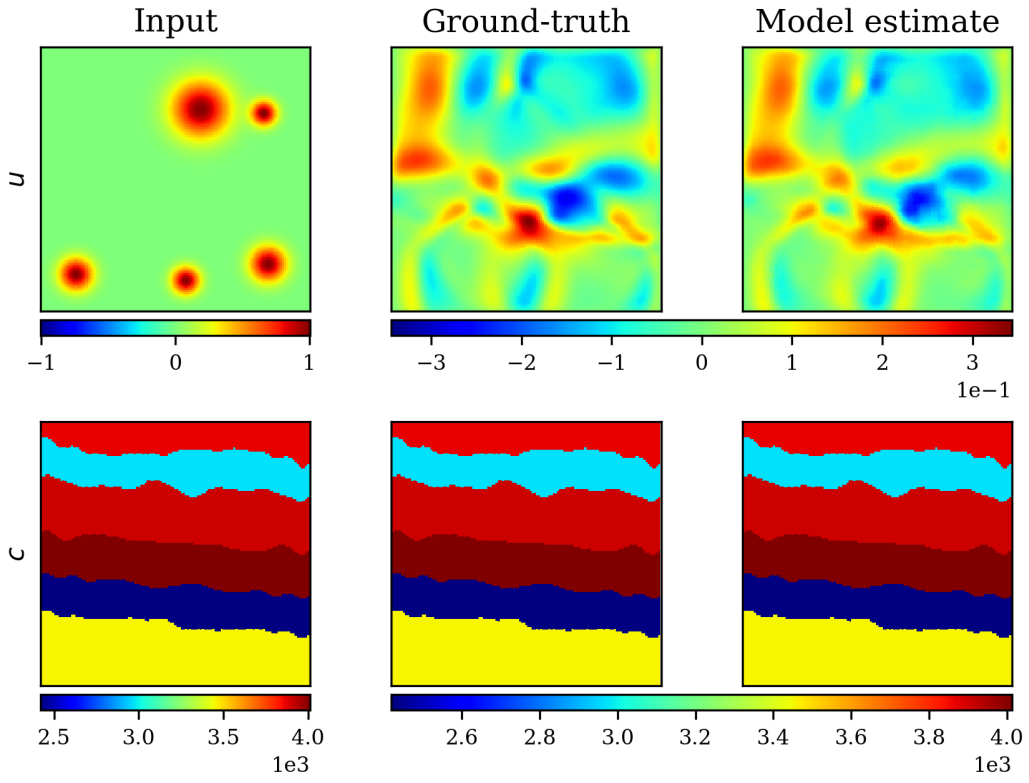


Figure G.24: Model input at $t = t_0$, ground-truth solution and model estimate at $t = t_{14}$ of a test sample Wave-Layer dataset.

1394 **NeurIPS Paper Checklist**

1395 **1. Claims**

1396 Question: Do the main claims made in the abstract and introduction accurately reflect the
1397 paper’s contributions and scope?

1398 Answer: [\[Yes\]](#)

1399 Justification: The abstract and introduction (lines 55-81) clearly state the paper’s contribu-
1400 tions regarding the GAOT model, and demonstrate its performance in terms of accuracy and
1401 efficiency across various PDE learning tasks.

1402 **2. Limitations**

1403 Question: Does the paper discuss the limitations of the work performed by the authors?

1404 Answer: [\[Yes\]](#)

1405 Justification: The Limitations and Extensions section (line 355-364) outlines several poten-
1406 tial limitations: this paper doesn’t address the rigorous theoretical analysis of GAOT. The
1407 method has not yet been evaluated on real 3D datasets, and it has not been tested on down-
1408 stream tasks such as uncertainty quantification (UQ), inverse problems, or PDE-constrained
1409 optimization.

1410 **3. Theory assumptions and proofs**

1411 Question: For each theoretical result, does the paper provide the full set of assumptions and
1412 a complete (and correct) proof?

1413 Answer: [\[NA\]](#)

1414 Justification: We do not present theoretical results in our paper.

1415 **4. Experimental result reproducibility**

1416 Question: Does the paper fully disclose all the information needed to reproduce the main ex-
1417 perimental results of the paper to the extent that it affects the main claims and/or conclusions
1418 of the paper (regardless of whether the code and data are provided or not)?

1419 Answer: [\[Yes\]](#)

1420 Justification: The paper states the detailed setup for generating experimental results and is
1421 provided in Supplemental Material sections [B](#) and [C](#).

1422 **5. Open access to data and code**

1423 Question: Does the paper provide open access to the data and code, with sufficient instruc-
1424 tions to faithfully reproduce the main experimental results, as described in supplemental
1425 material?

1426 Answer: [\[Yes\]](#)

1427 Justification: We have submitted our anonymized version of our code with the full paper
1428 submission. This includes the necessary details to set up the environment and run the
1429 experiments which will recreate the results from our proposed algorithm.

1430 **6. Experimental setting/details**

1431 Question: Does the paper specify all the training and test details (e.g., data splits, hyper-
1432 parameters, how they were chosen, type of optimizer, etc.) necessary to understand the
1433 results?

1434 Answer: [\[Yes\]](#)

1435 Justification: We have illustrated the detailed training and testing setup in the SM sections
1436 [B.5](#) and [C](#).

1437 **7. Experiment statistical significance**

1438 Question: Does the paper report error bars suitably and correctly defined or other appropriate
1439 information about the statistical significance of the experiments?

1440 Answer: [\[Yes\]](#)

1441 Justification: We provide sensitivity to training randomness in **SM Sec. E.7**.

1442 **8. Experiments compute resources**

1443 Question: For each experiment, does the paper provide sufficient information on the com-
 1444 puter resources (type of compute workers, memory, time of execution) needed to reproduce
 1445 the experiments?

1446 Answer: [Yes]

1447 Justification: The paper provides the detailed computer resources needed to reproduce these
 1448 experiments in the SM B.5.

1449 **9. Code of ethics**

1450 Question: Does the research conducted in the paper conform, in every respect, with the
 1451 NeurIPS Code of Ethics <https://neurips.cc/public/EthicsGuidelines>?

1452 Answer: [Yes]

1453 Justification: The paper follows the NeurIPS Code of Ethics in every respect. Our research
 1454 does not include the use of human subjects and focuses on models with minimal risk for
 1455 safety and security concerns or misuse.

1456 **10. Broader impacts**

1457 Question: Does the paper discuss both potential positive societal impacts and negative
 1458 societal impacts of the work performed?

1459 Answer: [Yes]

1460 Justification: The paper mentions wide-spread applications in science and engineering as a
 1461 positive impact. Moreover, our work is focused solely on scientific applications, with little
 1462 to no ability to be used for potentially harmful or nefarious tasks such as the generation of
 1463 false or misleading information or social engineering.

1464 **11. Safeguards**

1465 Question: Does the paper describe safeguards that have been put in place for responsible
 1466 release of data or models that have a high risk for misuse (e.g., pretrained language models,
 1467 image generators, or scraped datasets)?

1468 Answer: [NA]

1469 Justification: This work does not present any resources or artifacts with risks of misuse.

1470 **12. Licenses for existing assets**

1471 Question: Are the creators or original owners of assets (e.g., code, data, models), used in
 1472 the paper, properly credited and are the license and terms of use explicitly mentioned and
 1473 properly respected?

1474 Answer: [Yes]

1475 Justification: All the original owners of assets (e.g., code, data, models) are explicitly
 1476 mentioned in the paper. Any resources presented for the first time, i.e. the aforementioned
 1477 time-independent datasets, are owned by the authors and made publicly available under the
 1478 appropriate license.

1479 **13. New assets**

1480 Question: Are new assets introduced in the paper well documented and is the documentation
 1481 provided alongside the assets?

1482 Answer: [Yes]

1483 Justification: We provide documentation detailing the parameters within the dataset, as well
 1484 as how the data may be loaded to be used for use in other works.

1485 **14. Crowdsourcing and research with human subjects**

1486 Question: For crowdsourcing experiments and research with human subjects, does the paper
 1487 include the full text of instructions given to participants and screenshots, if applicable, as
 1488 well as details about compensation (if any)?

1489 Answer: [NA]

1490 Justification: The paper does not involve crowdsourcing nor research with human subjects.

1491 15. **Institutional review board (IRB) approvals or equivalent for research with human**
1492 **subjects**

1493 Question: Does the paper describe potential risks incurred by study participants, whether
1494 such risks were disclosed to the subjects, and whether Institutional Review Board (IRB)
1495 approvals (or an equivalent approval/review based on the requirements of your country or
1496 institution) were obtained?

1497 Answer: [NA]

1498 Justification: The paper does not involve research with human subjects.

1499 16. **Declaration of LLM usage**

1500 Question: Does the paper describe the usage of LLMs if it is an important, original, or
1501 non-standard component of the core methods in this research? Note that if the LLM is used
1502 only for writing, editing, or formatting purposes and does not impact the core methodology,
1503 scientific rigorousness, or originality of the research, declaration is not required.

1504 Answer: [NA]

1505 Justification: The core method development in this research does not involve LLMs as any
1506 important, original, or non-standard components.